An optical dipole trap for Erbium with tunable geometry

Simon Baier

M A S T E R T H E S I S

submitted to the

Faculty of

Mathematics, Computer Science and Physics

of the University of Innsbruck

Supervisor:

Univ. Prof. Dr. Francesca Ferlaino

October 2012

Abstract

In this thesis, we describe the realization of a novel optical dipole trap for erbium atoms. The trap is based on time-averaged potentials and is thus tunable in geometry. We investigate both theoretically and experimentally the dynamic polarizability of ground-state erbium atoms. The polarizability is a very important quantity for the understanding of the atomic properties of erbium and, prior to this thesis, its value was unknown. We measure a dynamic polarizability of $\mathrm{Re}(\alpha) = (84 \pm 2 \pm 18)$ a.u. for erbium atoms in a 1064-nm laser field, which is 47 % lower than the one we calculated based on the best knowledge of the erbium atomic spectrum. This discrepancy might points to a too rough knowledge of the atomic level structure or to novel unexpected effects arising in sub-merged shell atoms. Further investigations both in theory and experiments are highly needed.

For our novel optical dipole trap setup we use a scanning system consisting of an acousto-optical modulator, electronics and a customized optical setup. The dipole trap beam is shifted perpendicular to its horizontal axis, creating time-averaged potentials when the scan over a range of positions is fast enough compared to the trap frequency. The aspect ratio of the dipole trap can be tuned from 1.5 to 15. With the new dipole trap system we can load up to 35 % of MOT atoms to the dipole trap, which is related to mode-matching arguments. Further the density at each evaporation step can be optimized, leading to a large overall evaporation efficiency of 3.5. This improvements result in up to three times larger numbers in the pure BEC compared to our previous experiments.

With the new tunable dipole trap we are confident that in future we can investigate geometry-dependent anisotropic quantum effects, unique to dipolar gases.

Contents

Chapter 1

Introduction

Experiments on ultracold gases deal with atomic systems at temperatures near the absolute zero, where the atoms start to reveal their quantum behavior. Ultracold atomic gases provide an unprecedented level of control over many external and internal degrees of freedom. Remarkably, the interparticle interaction and the confining geometry can be changed almost "on demand", giving access to the investigation of various exciting phenomena belonging to a wide range of physical researches. Quantum simulations [Fey82], high-temperature superconductivity [Chi06], condensed matter [Gre08], few body physics [Fer10] and quantum chemistry [Osp10] just name a few of these phenomena.

The first experimental realization of a Bose-Einstein condensate (BEC) in 1995 [And95, Bra95, Dav95] marked the starting point of a new field in physics. The attainment of quantum degenerate Fermi gases further pushed the interest on this still rapidly growing field [DeM99, Sch01b, Tru01]. The level of control was increased by the ability to modify the interparticle interaction via Feshbach resonances [Chi10]. This controllability leaded to the observation of various fascinating phenomena, such as the superfluid to Mott insulator transition [Gre02] or the creation of weakly bound dimer states [Win06, Joc03, Fer09]. Even though the list of exciting results could be almost arbitrarily extended, all of these physical pioneering works were performed with elements from the alkali series, where the interaction is ruled by the surprisingly simple isotropic and short-range contact interaction.

To make the story even more exciting, efforts were taken to explore novel systems, in which the particles additionally interact via an anisotropic and long range interaction, called dipole-dipole interaction (DDI). Polar molecules and polar atoms carry an electric and a magnetic dipole moment, respectively, and, therefore, give access to the DDI. Because of the DDI new fascinating quantum phases are expected, which in particular depend on the trapping

geometry [Lah09, Bar08].

The first species used to study dipolar effects in experiments was chromium [Gri05, Bea08]. Among many fascinating phenomena the observation of the d-wave collapse of a Bose gas stands out [Lah08]. In order to deepen the experimental possibilities on dipolar physics novel species with even higher magnetic moments have become promising candidates in ultracold experiments. The recent realization of a BEC and a quantum degenerate Fermi gas of dysprosium by the group of B. Lev at Stanford [Lu11, Lu12] and the BEC of erbium by our group in Innsbruck [Aik12] promise to open a new chapter in the field of dipolar gases.

Erbium is part of the lanthanide series and has a rich energy spectrum. Due to its multivalence-electrons character complex scattering properties are expected. The investigation of optical transitions in erbium opened the possibility to control this species by means of laser cooling techniques [Ban05, McC06b].

The first goal of our experiment was to reach a BEC. In march, 2012 we could set an end to this over two years lasting journey. Worldwide we have been the first to cool down erbium to quantum degeneracy [Aik12]. In our experiment we load erbium atoms from the MOT to an optical dipole trap and evaporatively cool them down.

The purpose of my master thesis was to design an optical dipole trap with tunable geometry. This was realized by means of a scanning system, which can create time-averaged potentials. This improvement gave us the possibility to dynamically optimize the efficiencies in the loading and the evaporation phase of our experiment. Furthermore, the flexible geometry opens access to the investigation of various fascinating geometry-dependent quantum effects, unique to dipolar gases [Lim11, San03, Bla12]. To gain a deeper understanding of the dipole trap for erbium I also focused on the development of a mathematical model on dipole traps. This model calculates the dynamic polarizability of erbium taking all dipole allowed transitions into account. The difficulty of this calculation is connected to the complex and rather unknown energy spectrum of erbium [Ral11, Ban05]. Furthermore, with this model the trapping geometry of the dipole trap configuration in our experiment can be fully simulated.

This thesis is structured as follows. In Chap. 2 we present the properties of erbium and focus on the energy spectrum of erbium. Furthermore, the up-to-date known scattering properties of erbium are discussed. Chapter 3 reviews the theory of optical dipole traps and outlines the influence of the dipole effect on erbium atoms. The mathematical model used to calculate dipole trap parameters for erbium at our experiment is explained. Chapter 4 focuses deeply on the investigation of the atomic polarizability of erbium. In Chap. 5 the optical and electronic setup of the scanning system is discussed, as well as the

performance of the scanning system is characterized. Chapter 6 investigates the trapping geometry of the new dipole trap for erbium atoms and shows the measurement of the dynamic polarizability of erbium. The production of the new, improved Er-BEC is discussed. Finally, Chap. 7 concludes and outlines future experiments being accessible with the new dipole trap system.

Chapter 2

Erbium

Ultracold gases are ideal systems to observe exciting many- and few-body quantum effects. In recent years there is an increasing interest on the investigation of non-alkali atoms. Such species have rich atomic spectra, opening possibilities for novel laser cooling approaches and leading to fascinating interaction properties. Particularly interesting are multi-valence-electron atoms with a non-S electronic ground state, such as lanthanides. The interaction of alkali atoms can be described by a short-range and isotropic contact potential. Lanthanide atoms, such as erbium, provide a large magnetic dipole moment, leading to a long-range and anisotropic dipole-dipole interactions [Lah09]. This interaction is expected to give access to unexplored physical scenarios [Gor00].

In this Chapter, we briefly discuss the main properties of erbium and will then focus on the energy spectrum and the interaction of erbium atoms. For a closer insight into the properties of erbium see e.g. Ref. [Sch11].

2.1 A glance at erbium

General properties

Erbium (Er) is part of the lanthanide series and has an atomic number of 68. It is a soft, silver-colored metal, which has a comparatively high melting point of about 1530 °C [Jam92]. Erbium has six stable isotopes with masses ranging from 162 to 170 amu. Table 2.1 shows the natural abundance and nuclear spin of each isotope. There are three bosonic isotopes with a natural abundance exceeding 14 %. Remarkably, the natural abundance of the fermionic isotope is extremely high compared to the typically used fermionic species ^{40}K [DeM99] and ^{6}Li [Sch01a] belonging to the alkali class. This is a very favorable feature for experiments on degenerate Fermi gases.

Table 2.1: Natural abundance and nuclear spin quantum number I of all staple erbium isotopes.

mass m (amu)	abundance (%)	nuclear spin I	statistic
162	0.1	0	boson
164	1.6	0	boson
166	33.5	0	boson
167	22.9	7/2	fermion
168	27.0	0	boson
170	14.9	0	boson

$4f$-block atoms

Several species from the lanthanides, among which erbium, are also known as atoms of the $4f$-block. They are named in this way because of an unfilled $4f$ inner shell, shielded by a closed outer shell. This peculiarity plays a crucial role in the atom behavior. In the case of erbium, the electronic configuration of the ground state reads as [Xe]$4f^{12}6s^2$. The [Xe]-like core indicates that all shells are filled up to the $5p$ shell. From the 14 valence electrons only 12 are located in the $4f$ shell, leading to a two-electron vacancy. The two remaining electrons fill up the $6s$ shell. This leads to the so-called submerged shell structure. The f-shell is characterized by a strong anisotropy in the electron density distribution. One of the most relevant consequences is the large magnetic moment endowed by such atoms.

Another important feature is that the ground state of erbium has large quantum numbers. The bosonic erbium isotopes have a nuclear spin quantum number I of zero. Therefore the used quantum number to describe transitions in erbium is the total angular momentum quantum number J. For the ground state this quantum number yields $J = 6$. The fermionic isotope ^{167}Er has a nuclear spin quantum number I of 7/2, which leads to a hyperfine structure. The ground state splits up to eight hyperfine states from $F = 19/2$ to $F = 5/2$. The magnetic quantum numbers m_J are the projection of the total angular momentum quantum number and range between -6 and 6.

In erbium the valence electrons couple in a LS-scheme to the $^3H_6$ term of the ground state; see Fig. 2.1, leading to a large orbital angular momentum of $L = 5$. Due to the non-S ground state an anisotropy in the interaction of atoms is expected [Kre04].

2.2 Energy spectrum of erbium atoms

The rich and complex energy spectrum of erbium is shown in Fig. 2.1. From the NIST Atomic Spectra Database [Ral11] there are 672 excited states known with J values ranging from 1 to 12. The energy of the excited states in relation to the ground state ranges from 5035 to 46971 cm^{-1} and the ionization limit is 49262 cm^{-1}. Black and red lines indicate even and odd parity states, respectively. Only levels with J values ranging from 5 to 7 and even parity can couple to the ground state via optical dipole transitions. These transitions are shown in Fig. 2.2. The natural linewidths $\Delta\nu$ of these states are located in a wide range from the MHz to the subHz regime.

To describe the quantum states of erbium two different angular momenta coupling schemes are needed. In the spin-orbit (LS-) coupling the individual electronic orbital angular momenta $\vec{l}$ and spins $\vec{s}$ add to the total orbital angular momentum $\vec{L}$ and to the total spin $\vec{S}$, respectively. Finally they couple to the total angular momentum $\vec{J} = \vec{L} + \vec{S}$ [Dem05]. In erbium the $4f^{12}6s^2$ electrons of the outer shells follow these coupling scheme forming the $^3H_6$ term of the ground state[1]. Other levels of erbium have to be described by $J_1 J_2$ coupling. In this case the $4f$ and the $6s$ electrons couple independently in a LS-coupling scheme. The formed states $\vec{J}_1$ and $\vec{J}_2$ add then up to a total angular momentum.

For laser cooling of erbium atoms at our experiment we use the strong 401-nm transition and the narrow 583-nm transition. These transitions were proposed in Ref. [Ban05]. The 401-nm line is used for the Zeeman slower (ZS) and has a linewidth of 29.7 MHz; see Fig. 4.2. For the operation of the magneto-optical trap (MOT) we use the 583-nm line, which has a linewidth of $\Delta\nu = 190$ kHz. At this transition one of the valence electrons is excited to the $6p$ shell, thereby changing its spin. This kind of transitions are forbidden in LS-coupling and are called intercombination lines. This leads to the observed narrower linewidth. For evaporative cooling we use an optical dipole trap (ODT) operating at a wavelength of 1064 nm. The contribution of every dipole allowed transition to the trapping potential is discussed in Sec. 4.1.

[1] The term symbol for this quantum state is $^{(2s+1)}L_J$ where $L = 5$ is correlated to the letter H.

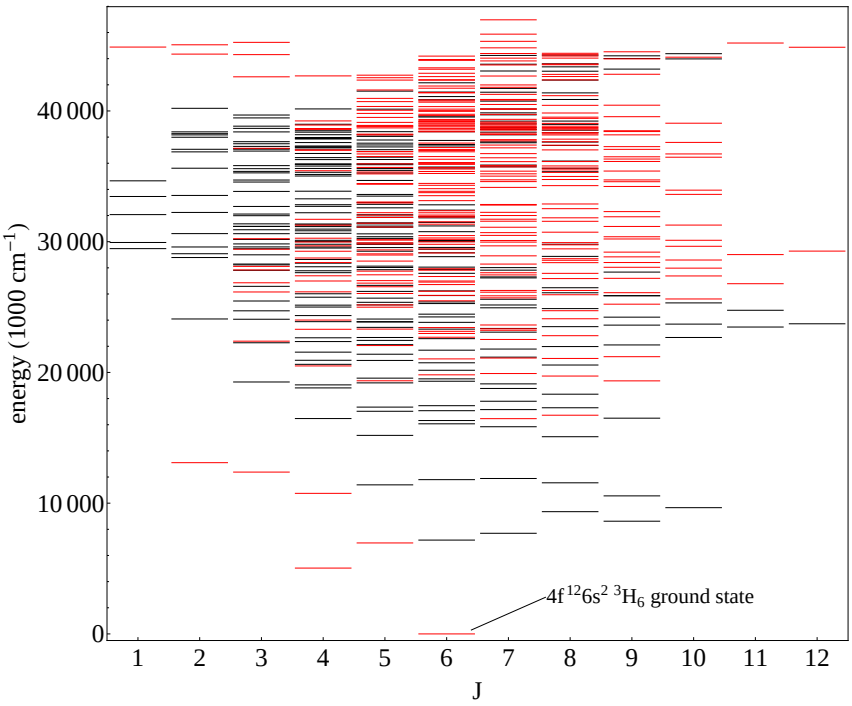

Figure 2.1: Full energy spectrum of erbium with total angular momentum quantum numbers J ranging from 1 to 12. The energy is given with respect to the ground state [Xe]$4f^{12}6s^2(^3H_6)$. Red lines have even parity where black lines have odd parity. The data were taken from [Ral11].

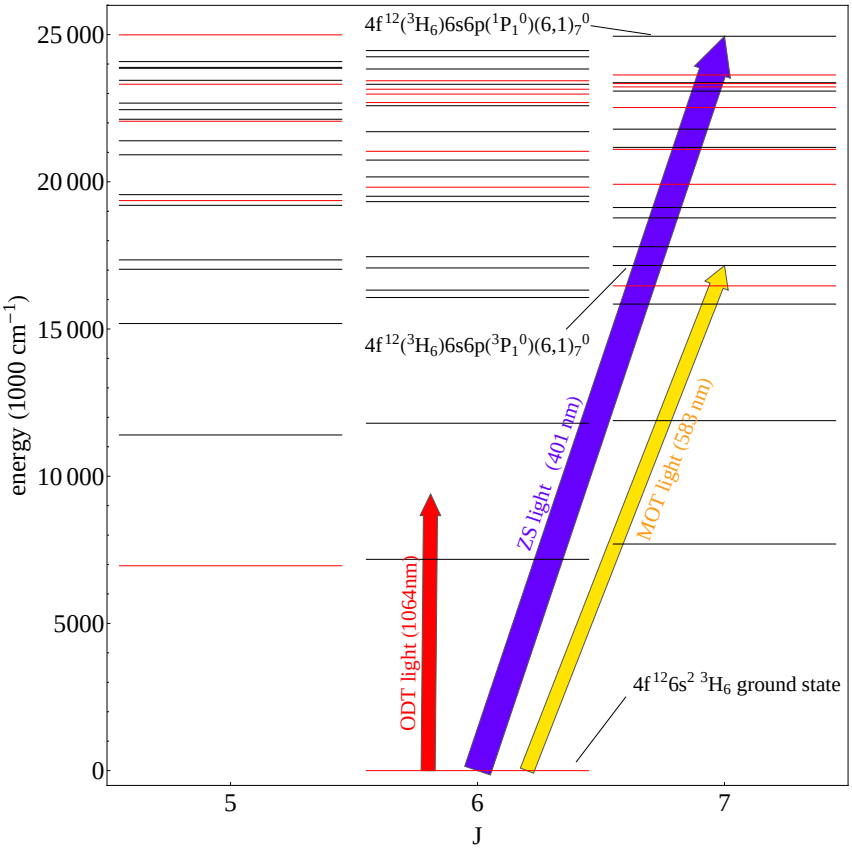

Figure 2.2: Zoom of the energy levels relevant for laser cooling. The excited level with odd parity (black line) can couple to the ground state $4f^{12}6s^2(^3H_6)$ via optical dipole transition. The blue and the yellow arrow indicate the levels, which are used for the deceleration of atoms in the ZS and the capturing of atoms in the MOT, respectively. The red arrow shows the energy of the used ODT laser. The data were taken from [Ral11].

2.3 Interaction between erbium atoms

For the achievement of quantum degeneracy the scattering properties play a crucial role. An important quantity is the background scattering length a, which is an intrinsic property of a specific isotope and describes the strength of the contact interaction between the atoms. For erbium, a is so far not known. During this thesis work we could Bose condense the ^{168}Er isotope by means of evaporative cooling. This already indicates a favorable background scattering length a for experimental work[2]. In theory the interaction is described by the isotropic van der Waals C_6 value and scales with the interatomic distance R as $1/R^6$. For non-S state atoms, such as erbium, additionally to the isotropic contact interaction anisotropic interactions are expected [Kre04].

Anisotropy in the interaction

In the case of dysprosium the anisotropy in the interaction was discussed by Kotochigova et al. [Kot11]. For erbium a similar behavior is expected. It is shown that the van der Waals potential also has a long-range part, which strongly depends on m_J. This is a consequence of an anisotropic coupling of the open f-shell electrons of the two atoms. Different projection quantum numbers of the total angular momentum lead to a spread of the C_6 value. This spread is defined by the anisotropic dispersion potential $\Delta C_6/R^6$. Additionally there can be found a magnetic dipole-dipole interaction (DDI) and an electrostatic quadropole-quadropole interaction. The DDI scales as C_3/R^3 where C_3 has an angle dependence and will be discussed later.

Due to these interactions higher partial waves can couple with each other, which can lead to inelastic losses. Figure 2.3 shows that, depending on the interatomic distance, different interactions are dominant. At small separation the anisotropic interactions lead to mixing of rotational levels, where at large R the Zeeman splitting dominates.

The presence of anisotropy also changes the nature of Feshbach resonances. Due to the anisotropy couplings to bound states with non-zero l can occur. Therefore, for submerged-shell atoms multiple Feshbach resonances are predicted [Pet12]. In our experiment we already could confirm this theoretical prediction by finding not less than six resonances in a narrow magnetic-field range up to 3 G; see Appendix C.

[2]Preliminary cross-dimensional thermalization measurements give $a_{^{168}\mathrm{Er}} = 180 \pm 50\, a_0$.

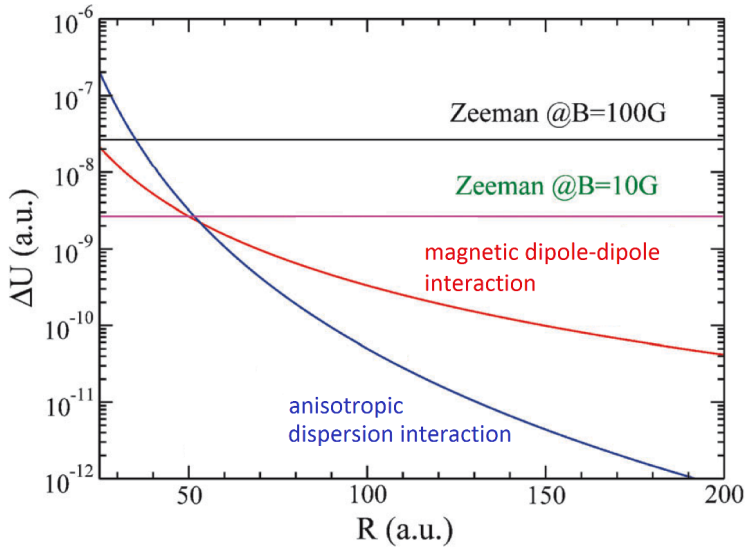

Figure 2.3: Level splitting due to interactions between two Dy atoms as a function of their interatomic seperation. For short distances R of the atoms the energy shifts of the anisotropic interactions are dominant over the Zeeman shifts, leading to m_J-changing collisions. The graph is taken from [Kot11].

Magnetic properties

One of the anisotropic interactions giving rise to novel scattering behavior is the magnetic dipole-dipole interaction, which is related to the magnetic dipole moment. The ground state of erbium has a total angular momentum quantum number J of 6 and a magnetic quantum number m_J of 6. This leads to a Landé g-factor g_J of 1.16. The magnetic moment μ is calculated by

$$\mu = g_J m_J \mu_B. \tag{2.1}$$

For the ground state of erbium atoms this gives $\mu = 6.98\,\mu_B$, which is about seven times larger than the magnetic moment of alkali atoms. For two polarized magnetic dipoles the DDI is defined as

$$U_{dd} = \frac{C_3}{|\vec{r}|^3} = \frac{\mu_0 \mu^2}{4\pi} \frac{1 - 3cos^2(\theta)}{|\vec{r}|^3}, \tag{2.2}$$

where $\vec{r}$ is the relative coordinate between the dipoles, θ is the angle between the quantization axis and the interatomic axis, defined by $\vec{r}$ [Lah09] and μ_0 is the magnetic constant. In contrast to the short range contact interaction, which scales with $1/|\vec{r}|^6$, the DDI scales with $1/|\vec{r}|^3$, and is thus a long-range

interaction. The anisotropy of the DDI is indicated by the dependence on the angle θ. When the dipoles are placed side-to-side they repel each other, while a head-to-tail configuration leads to attraction. The characteristic length scale for the DDI of erbium is

$$a_{dd} = \frac{m\mu_0\mu}{4\pi\hbar} = 201\, a_0, \tag{2.3}$$

where m is the mass of erbium and a_0 is the Bohr radius [Bar08]. The large mass of erbium enhances the dipolar character.

As discussed earlier due to the anisotropic DDI novel collisional behavior is expected, since also higher partial waves can couple with each other. This coupling could, for example, induce collisions between ultracold identical fermions, which are usually forbidden by the Pauli exclusion principle [Bar08]. This opens up new possibilities for experiments on degenerate Fermi gases.

To visualize the DDI one can "turn off" the contact interaction by tuning the scattering length via Feshbach resonances, leading to a d-wave collaps of the atomic cloud. For the collapse the relative strength of the dipolar and the contact interaction has to be compared. The collapse occurs when [Lah08]

$$\epsilon_{dd} = \frac{a_{dd}}{3a} \geq 1. \tag{2.4}$$

As a proof-of-principle experiment this collapse was also shown at our experiment; see Appendix C.

Scattering experiments

Scattering experiments on submerged-shell atoms are a new and challenging field. In the case of erbium the scattering behavior is only weakly known. In 2004 it was shown that erbium can successfully be trapped in a He buffer gas cooled magnetic trap at temperatures below 1 K [Han04]. This indicated, that in Er-He collisions the interaction anisotropy can be suppressed by the spherically symmetric $6s$-shell, allowing magnetic trapping and evaporative cooling. However, this conclusion could not hold for Er-Er collisions. In 2010 large spin relaxation rates of erbium in a magnetic trap at temperatures near 500 mK were measured, implying that evaporative cooling in magnetic traps will be highly inefficient [Con10]. In our experiment an optical dipole trap is used to evaporative cool erbium atoms. Chap. 3 gives a theoretical discussion on dipole traps for erbium.

The goal of our experiment is to further investigate the scattering properties of erbium. The observations of the dipolar collapse and the first Feshbach resonances lead in the right direction.

Chapter 3

Optical dipole trap

In recent years new atomic species have been used in ultracold experiments to study novel physical phenomena. It has been discovered that for some species magnetic traps are not appropriate for loading and evaporative cooling of atoms because of large collisional relaxation rates [Söd98, Con10]. This has led to the investigation of optical dipole traps, which are nowadays a crucial tool in many ultracold experiments. In this Chapter we will give an overview on the basic mechanism at the foundation of the interaction between light field and atoms, which is at the origin of a trapping potential. Furthermore, we will discuss this interaction in the case of erbium, which is correlated to the atomic polarizability[1] of erbium. Finally, we will introduce the theoretical model that we use to simulate the trapping potential at our Er-experiment.

3.1 Theoretical background

An intuitive picture of the dipole force acting on the atoms can be obtained by considering the case of a classical oscillator [Phi92]. By placing a neutral atom in an oscillating electric field, e.g. laser field, the centers of mass of both the positive and negative charge are separated by the field. This separation leads to an induced electric dipole moment in the atom. The atom can then be treated as a dipole that interacts with the driving field. When the dipole is driven below resonance it oscillates in phase with the field and when it is driven above resonance it oscillates out of phase. Below (above) resonance the interaction energy is negative (positive) and therefore the atom is roped into (out of) the region with the highest intensity of the electric field. For atoms the

[1]The atomic polarizability describes the coupling strength of an atom to an electromagnetic field and can, therefore, be used to calculate the potential depth of an optical dipole trap.

resonance frequency is defined by the energy of the excited state with respect to the ground state. We call the driving field red-detuned when its frequency is below resonance and blue-detuned when it is above resonance. Laser beams can be described by Gaussian beams, where the intensity profile has a Gaussian shape. This means that the intensity is the highest in the center of the beam and decreases with radial and axial distance. Due to these facts one can create a trap by sending red detuned laser light on atoms. All atoms will be pushed to the center of the beam and thus can minimize their energy.

Of course the dipole force can also be seen as an scattering process of an atom and a photon. Usually the photon is absorbed by the atom and then spontaneously re-emitted, each time leading to a momentum transfer. In contrast to normal scattering for far-detuned light absorption and emission cannot be seen as independent events anymore. This is the correlation, which leads to the non dissipative nature of the dipole force.

The mathematical discussion in the next section follows the review article of Grimm et. al [Gri00].

3.1.1 The oscillator model

An electric field $\vec{E}(\vec{r})$ with frequency ω induces an electric dipole moment in an atom given by

$$\vec{p}(\vec{r}) = \alpha \vec{E}(\vec{r}). \tag{3.1}$$

α is the complex polarizability of the atom and depends on the atomic species, the light frequency ω and the polarization of the electric field. From this relation one can calculate the potential rising from the interaction of $\vec{p}$ and $\vec{E}$:

$$U_{dip}(\vec{r}) = -\frac{1}{2}\langle \vec{p}(\vec{r})\vec{E}(\vec{r})\rangle = -\frac{1}{2\epsilon_0 c}\mathrm{Re}(\alpha) I(\vec{r}). \tag{3.2}$$

Here the relation for the field intensity $I(\vec{r}) = 2\epsilon_0 c|\vec{E}(\vec{r})|^2$ is used, ϵ_0 being the dielectric constant and c the speed of light in vacuum. The real part of the polarizability accounts for the in-phase oscillation.

In addition to the generated potential the driven oscillator absorbs energy, which is then re-emitted as dipolar radiation. One can describe this absorption by the out of phase component, thus the imaginary part of the polarizability:

$$P_{abs} = \langle \dot{\vec{p}}\vec{E}\rangle = \frac{\omega}{\epsilon_0 c}\mathrm{Im}(\alpha) I(\vec{r}). \tag{3.3}$$

This absorption can be seen as a photon scattering process and, therefore, the scattering rate can be written as

$$\Gamma_{sc}(\vec{r}) = \frac{P_{abs}}{\hbar\omega} = \frac{1}{\hbar\epsilon_0 c}\mathrm{Im}(\alpha) I(\vec{r}), \tag{3.4}$$

$\hbar$ being the Planck constant divided by 2π.

In general it is very difficult to calculate the atomic polarizability α, but there exist theoretical models, which make this calculation more easy. For the calculation one can either use the classical Lorentz-oscillator model or a semiclassical approach. In the classical model an electron is bound elastically to the atom core and oscillates with the eigenfrequency ω_0, which is the optical transition frequency of a two-level atom. This oscillation is damped due to radiative energy loss. The damping rate is proportional to the spontaneous decay rate Γ of the excited level. The spontaneous decay rate Γ is correlated to the natural linewidth $\Delta\nu$ with $\Gamma = 2\pi\Delta\nu$. The semiclassical approach considers an atom as a two-level quantum system in a classical radiation field. The case of a far-detuned electric field is of particular interest for us, because the scattering rate becomes very low and, therefore, heating processes can be neglected. In this case both models give the same result and thus the atomic polarizability can be extracted. For large detunings the following expressions for the dipole potential and the scattering rate can be derived [Gri00]:

$$U_{dip}(\vec{r}) = -\frac{3\pi c^2}{2\omega_0^3}\left(\frac{\Gamma}{\omega_0-\omega}+\frac{\Gamma}{\omega_0+\omega}\right) I(\vec{r}), \tag{3.5}$$

$$\Gamma_{sc}(\vec{r}) = \frac{3\pi c^2}{2\hbar\omega_0^3}\left(\frac{\omega}{\omega_0}\right)^3\left(\frac{\Gamma}{\omega_0-\omega}+\frac{\Gamma}{\omega_0+\omega}\right)^2 I(\vec{r}). \tag{3.6}$$

These two equations are probably the most important relations to understand the physics of dipole traps using far-detuned laser fields. Equation (3.5) indicates, that the sign of the dipole potential depends on the sign of the detuning $\Delta = \omega - \omega_0$ ($\Delta < 0$: red detuning; $\Delta > 0$: blue detuning). This is the mathematical explanation of the above-discussed "intuitive picture". If the laser frequency is smaller (larger) than the atomic resonance frequency, the dipole potential is negative (positive) and, therefore, atoms are located at the region with maximum (minimum) intensity of the laser beam. The comparison of Eq. (3.5) and Eq. (3.6) also shows why usually far-detuned laser light is used for optical dipole traps. As U_{dip} scales with $\frac{I}{\Delta}$ and Γ_{sc} scales with $\frac{I}{\Delta^2}$ it is clear that the scattering rate can be suppressed for large detunings.

3.1.2 Multilevel atoms

The following model provides a picture on the interaction between a light field and an atom, which can be used for atoms with more than two internal energy states. To extend the above discussed model to a multilevel quantum system we have to introduce the influence of a far-detuned electric field on all

the atomic levels. Mathematically this influence is treated as a second-order time-independent perturbation with interaction Hamiltonian $\mathcal{H}_1 = \mu E$, where $\mu = -e\vec{r}$ represents the electric dipole operator.

Two-level system

For a two-level atom the coupling to the electric field leads to an energy shift of the ground state:

$$\Delta E = \frac{|\langle e|\mu|g\rangle|^2}{\Delta}|E|^2, \tag{3.7}$$

which is nothing else than the ac-Stark shift. For the excited state the shift is the same but with opposite sign. $|\langle e|\mu|g\rangle|$ is the dipole matrix element between the ground state $|g\rangle$ and the excited state $|e\rangle$ and corresponds to the spontaneous decay rate Γ of the excited state:

$$\Gamma = \frac{\omega_0^3}{3\pi\epsilon_0\hbar c^3}|\langle e|\mu|g\rangle|^2. \tag{3.8}$$

Because of these relations the energy shift by the light, corresponding also to the dipole potential seen by the atoms, only depends on the spontaneous decay rate Γ, the detuning Δ, and the intensity I of the laser light. Figure 3.1(b) shows the ac-Stark shift for a two-level atom due to an electric field. Applying a Gaussian laser beam generates a trapping potential for atoms in their ground state as depicted in 3.1(c).

Multi-level system

For a multilevel atom all allowed transitions from a ground state $|g_i\rangle$ to an excited state $|e_j\rangle$ are involved. Dipole transitions are only allowed when the total angular momentum quantum number J changes by $0, \pm 1$ with respect to the ground state and the parity of the excited state is different[2][Dra96]. For the contribution of each excited state to the ac-Stark shift, furthermore, the real transition coefficients c_{ij} have to be taken into account. These transition-dependent factors determine the specific dipole matrix elements

$$\mu_{ij} = c_{ij}||\mu||, \tag{3.9}$$

where $||\mu||$ is the fully reduced matrix element, which is related to the spontaneous decay rate Γ according to Eq. (3.8). The transition coefficients c_{ij}, which

[2]The parity gives information about how the electronic wave function $\psi(\vec{r})$ is inverted through the origin. For $\psi(-\vec{r}) = \psi(\vec{r})$ the parity is even, where for $\psi(-\vec{r}) = -\psi(\vec{r})$ the parity is odd.

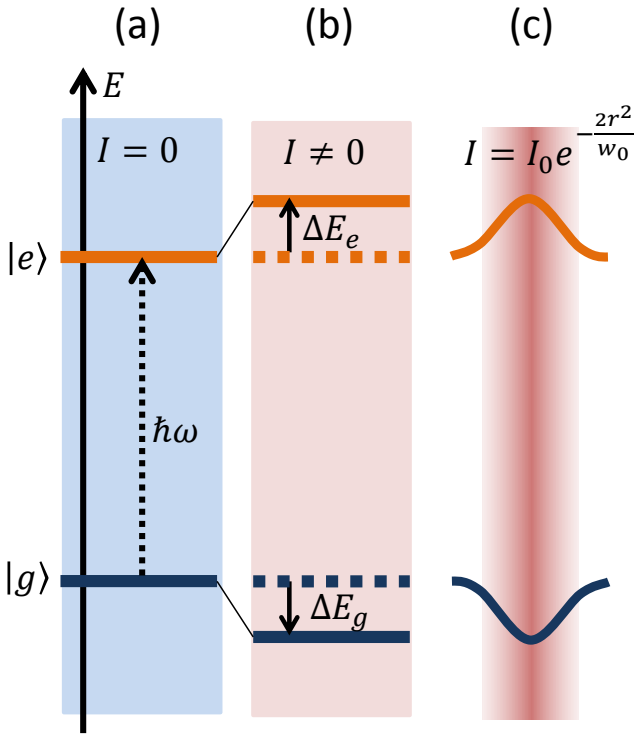

Figure 3.1: Schematic of the ac-Stark shift of a two-level atom for red-detuned light with intensity I (b). ΔE_g and ΔE_e are the energy shifts of the ground state $|g\rangle$ and the excited state $|e\rangle$, respectively. In (c) the potential seen by an atom in a Gaussian beam with peak intensity I_0 and beam waist w_0 is shown.

consider the coupling strength between specific sub-levels $|g_i\rangle$ and $|e_j\rangle$, depend on the laser polarization and the electric angular momenta involved. They can be calculated with the use of the $3J$-symbol to

$$c_{ij}^2 = (2J_j + 1) \begin{pmatrix} J_i & 1 & J_j \\ m_i & p & -m_j \end{pmatrix}^2, \tag{3.10}$$

where J_i and J_j are the total angular momenta of the states $|g_i\rangle$ and $|e_j\rangle$, respectively. The parameters m_i and m_j are the corresponding magnetic quantum numbers and p denotes the laser polarization. Equation (3.10) is adapted from Ref. [Gra07]. The $3J$-symbol is only non zero when the relation

$$m_i + p = m_j \tag{3.11}$$

is fulfilled. For linear π and circular $\sigma^{\pm}$ polarized light p is equal to 0 and ± 1, respectively. The relation indicates that for linear polarized light, e. g. , a

ground state in the stretched state $m_i = -J_i$ will not couple to an excited state with $J_j = J_i - 1$, since in this case the magnetic quantum numbers m_i and m_j cannot be equal. For different laser polarization different excited states contribute to the ac-Stark shift. The line strength factors are included by defining a new variable $\tilde{\Gamma}_j$

$$\tilde{\Gamma}_j = c_{ij}^2 \Gamma_j = (2J_j + 1) \begin{pmatrix} J_i & 1 & J_j \\ m_i & p & -m_j \end{pmatrix}^2 \Gamma_j, \tag{3.12}$$

where Γ_j is the spontaneous decay rate of the corresponding excited state $|e_j\rangle$.

The overall energy shift of a state $|g_i\rangle$ is given by the sum over the contributions of each coupled excited state $|e_j\rangle$ according to the detuning $(\omega - \omega_{ij})$, the spontaneous decay rate Γ_j and the line strength factors c_{ij}^2. This leads to the following generalization of Eqs. (3.5) and (3.6):

$$U_{dip}(\vec{r}) = -\sum_j \frac{3\pi c^2}{2\omega_{ij}^3} \left(\frac{\tilde{\Gamma}_j}{\omega_{ij} - \omega} + \frac{\tilde{\Gamma}_j}{\omega_{ij} + \omega} \right) I(\vec{r}), \tag{3.13}$$

$$\Gamma_{sc}(\vec{r}) = \sum_j \frac{3\pi c^2}{2\hbar\omega_{ij}^3} \left(\frac{\omega}{\omega_{ij}} \right)^3 \left(\frac{\tilde{\Gamma}_j}{\omega_{ij} - \omega} + \frac{\tilde{\Gamma}_j}{\omega_{ij} + \omega} \right)^2 I(\vec{r}). \tag{3.14}$$

To calculate the trapping potential and the scattering rate the intensity distribution of the electric field has to be known. The simplest realization of an optical dipole trap is to focus a single red-detuned laser beam onto the atoms. In Gaussian optics [Sal91], the intensity of a laser beam propagating along the z-axis with radial symmetry r is described by

$$I(r, z) = \frac{2P}{\pi w^2(z)} \exp\left(-2\frac{r^2}{w^2(z)} \right) \tag{3.15}$$

with P being the total power[3]. $w(z)$ is the $1/e^2$ beam radius[4] and it is defined by the minimal beam waist w_0, the axial coordinate z, and the Rayleigh range z_R:

$$w(z) = w_0 \sqrt{1 + \frac{z^2}{z_R^2}}. \tag{3.16}$$

[3] P can be calculated by integrating the intensity $I(r)$ over the whole area in polar coordinates.

[4] This means that within a circle of radius $r = w(z)$ approximately 86% of the power is contained.

The Rayleigh range $z_R = \pi w_0^2/\lambda$ describes the distance over which the waist of the beam has increased to $\sqrt{2}w_0$. Equation (3.15) indicates that the intensity is the highest in the focal point at the center of the beam.

$$I_0 = I(0,0) = \frac{2P}{\pi w_0^2} \tag{3.17}$$

This peak intensity I_0 and the polarizability $\tilde{U}$ define the total trap depth

$$\hat{U} = -\sum_j \frac{3\pi c^2}{2\omega_{ij}^3}\left(\frac{\tilde{\Gamma}_j}{\omega_{ij}-\omega} + \frac{\tilde{\Gamma}_j}{\omega_{ij}+\omega}\right) I(0,0) = \tilde{U} I_0. \tag{3.18}$$

For convenience we express the polarizability in units of $2\epsilon_0 c^5$. In literature it is often distinguished between the scalar and the tensorial part of the polarizability. The formula given in this thesis includes already both, the scalar and the tensorial part.

3.2 The case of erbium

As discussed previously, the total trapping potential is determined by the contribution of every dipole allowed transition according to the detunings Δ_{ij}, the spontaneous decay rates Γ_j and the line strength factors c_{ij}^2. In the case of erbium the calculation of the polarizability is difficult, since this rare-earth element has such a complicated level structure; see Sec. 2.2. To provide a complete set of excited states and their corresponding linewidths precise spectroscopy and complex calculations are necessary. Up-to-date still many lines in erbium are not known.

Due to new data from J.-F. Wyart and the group of O. Dulieu [Law10, Wya12], we can calculate the polarizability for the ground state of erbium atoms, as well as for the 583-nm and 401-nm state. For these calculations we use linear polarized light at 1064 nm and assume that the atomic sample is prepared in the stretched state $m_i = -J_i$:

$$\tilde{U}_{|g\rangle} = -4.9384 \cdot 10^{-37}\,\mathrm{Jm^2/W},$$

$$\tilde{U}_{583} = -9.0164 \cdot 10^{-39}\,\mathrm{Jm^2/W},$$

$$\tilde{U}_{401} = -1.3633 \cdot 10^{-38}\,\mathrm{Jm^2/W}.$$

[5] According to Eq. (3.2) $\tilde{U}$ is correlated to the complex polarizability α with $\tilde{U} = \frac{1}{2\epsilon_0 c}\mathrm{Re}(\alpha)$.

In atomic units the atomic polarizabilities are $\mathrm{Re}(\alpha_{|g\rangle}) = 159.01$ a.u., $\mathrm{Re}(\alpha_{583}) = 2.90$ a.u. and $\mathrm{Re}(\alpha_{401}) = 4.39$ a.u. The resulting potential depths for a Gaussian laser beam with a 30 μm waist and a power of 10 W are:

$$\hat{U}_{|g\rangle} = -253.01\,\mu\mathrm{K},$$

$$\hat{U}_{583} = -4.62\,\mu\mathrm{K},$$

$$\hat{U}_{401} = -6.98\,\mu\mathrm{K}.$$

In Chap. 4 we will focus deeply on the calculation of the polarizability and will also discuss the influence of trapping laser light with a different wavelength.

3.3 Modeling of the trapping potential

On the route to quantum degeneracy, the design of an optimal dipole trap plays a crucial role. The most important parameters of an optical trap are the trap depths and the trap frequencies, which give insight on the confinement in each spatial direction. The confinement can be manipulated by changing the power, the waist or the propagation direction of the laser beams. For a single, circular beam the calculation of the relevant parameters is straightforward. But a single beam cannot create a strong confinement in the axial direction. In our experiment we cross two elliptic beams within a specific angle to create the dipole trap. The angle is not avoidable, because the optical access to the chamber is limited. The ellipticity of the horizontal laser beam is tunable as will be shown in Sec. 5.1.

A major part of my thesis work was about setting up a calculation[6] to design the optimal trapping potential for our experiment. This model can also be adapted to any other atomic element and calculates trapping parameters for arbitrary crossed elliptic beams.

In this Section, we will follow a step-by-step mathematical approach to model optical dipole traps and derive relevant parameters. We will start by considering a single circular laser beam. We will then allow the beam to be elliptic. Further we will consider the case of two beams crossing at an angle of 90°. Then we will describe the trapping geometry for a crossed beam dipole trap intersecting at an arbitrary angle. Finally we will take gravity into account, which plays an important role for shallow trapping potentials.

In a last step, we will use this model to simulate the trapping potential of the used dipole trap in our experiment.

[6]The source code of this file can be found in Appendix B (Program version: Wolfram Mathematica 8.0)

Single circular beam

The trapping potential of a dipole trap was already discussed in Sec. 3.1.2. It is defined as:

$$U_{dip} = \tilde{U} I(\vec{r}),$$

where $\tilde{U}$ is the atomic polarizability and $I(\vec{r})$ is the laser intensity. For a circular Gaussian beam it has the following form:

$$I(r,z) = \frac{2P}{\pi w^2(z)} \exp\left(-2\frac{r^2}{w^2(z)}\right). \tag{3.19}$$

For small atomic clouds compared to the size of the laser beam it is possible to use a harmonic approximation to extract the trap frequencies. This is a reasonable assumption, since atoms populate only the center of the trap. The harmonic approximation gives for the potential of a single circular beam:

$$U_{circular} \approx \frac{1}{2}\frac{\partial^2 U_{dip}}{\partial r^2}(0) r^2 + \frac{1}{2}\frac{\partial^2 U_{dip}}{\partial z^2}(0) z^2 = \hat{U}\left(1 - 2\frac{r^2}{w_0^2} - \frac{z^2}{z_R^2}\right). \tag{3.20}$$

Here w_0 represents the minimal beam waist at the focal point, z_R is the Rayleigh range and $\hat{U} = \tilde{U} I(0)$ is the total trap depth. By comparing Eq. (3.20) to the classical harmonic potential $\frac{1}{2}m(\omega_r^2 r^2 + \omega_z^2 z^2)$ one finds for the trap frequencies in radial and axial direction:

$$\omega_r \equiv \sqrt{\frac{4\hat{U}}{m w_0^2}}, \quad \omega_z \equiv \sqrt{\frac{2\hat{U}}{m z_R^2}}. \tag{3.21}$$

The axial confinement is much weaker than the radial confinement, because z_R is much larger than w_0 and the axial trap frequency is smaller by a factor of $\sqrt{2}$. Because $\hat{U}$ is proportional to P/w_0^2 and $z_R \propto w_0^2$, the dependence of the trap frequencies can also be written as

$$\omega_r \propto \sqrt{P}/w_0^2, \quad \omega_a \propto \sqrt{P}/w_0^2. \tag{3.22}$$

Single elliptic beam

For the description of an elliptic beam one has to switch to Cartesian coordinates. The axes definition are the same as for the horizontal beam in Fig. 3.2. As already seen in Eq. (3.19) the peak intensity is in principle nothing else than the total power divided by the area of the beam. For an elliptic beam the waists in the radial directions x and y are different and defined as horizontal

waist $w_x(z)$ and vertical waist $w_y(z)$. Therefore, the total cross section of the laser beam changes, and leads to the following intensity profile:

$$I(x,y,z) = \frac{2P}{\pi w_x(z) w_y(z)} \exp\left[-2\left(\frac{x^2}{w_x^2(z)} + \frac{y^2}{w_y^2(z)}\right)\right]. \tag{3.23}$$

The harmonic approximation of the trapping potential gives

$$U_{elliptic} \approx \hat{U}\left[1 - \frac{2x^2}{w_x^2} - \frac{2y^2}{w_y^2} - \frac{1}{2}z^2\left(\frac{1}{z_{R_x}^2} + \frac{1}{z_{R_y}^2}\right)\right], \tag{3.24}$$

where w_x and w_y are the minimal beam waists along the radial directions x and y. z_{R_x} and z_{R_y} are the corresponding Rayleigh ranges along the axial z direction and

$$\hat{U} = \tilde{U}\frac{2P}{\pi w_x w_y}$$

is the total trap depth. For convenience we define a new Rayleigh range $z_{R_{ell}}$:

$$z_{R_{ell}} = \frac{z_{R_x} z_{R_y}}{\sqrt{\frac{1}{2}(z_{R_x}^2 + z_{R_y}^2)}}. \tag{3.25}$$

Finally, the trap frequencies for a single elliptic beam read as

$$\omega_x \equiv \sqrt{\frac{4\hat{U}}{m w_x^2}}, \quad \omega_y \equiv \sqrt{\frac{4\hat{U}}{m w_y^2}}, \quad \omega_z \equiv \sqrt{\frac{2\hat{U}}{m z_{R_{ell}}^2}}. \tag{3.26}$$

Crossed beams at 90°

The crossing of two beams in principle only adds another dipole trap potential to the system. Here we define the propagation direction of the second beam along the y-axis (axis of gravity), which is shown schematically in Fig. 3.2. The first beam is defined as horizontal beam and the second beam as vertical beam. The new trapping potential of the vertical beam is added to the trapping potential of the horizontal beam and leads to the following total potential:

$$\begin{aligned} U_{crossed} \approx\ & \hat{U}_1\left[1 - \frac{2x^2}{w_{1x}^2} - \frac{2y^2}{w_{1y}^2} - \frac{1}{2}\frac{z^2}{z_{R_{1,ell}}})\right] - \\ & - \hat{U}_2\left[1 - \frac{2x^2}{w_{2x}^2} - \frac{2z^2}{w_{2z}^2} - \frac{1}{2}\frac{y^2}{z_{R_{2,ell}}})\right]. \end{aligned} \tag{3.27}$$

The definition w_{1i} (w_{2i}) indicates the quantity for the minimal beam waist along the axis $i = x$, y, z of the horizontal (vertical) beam. $z_{R_{1,ell}}$ and $z_{R_{2,ell}}$

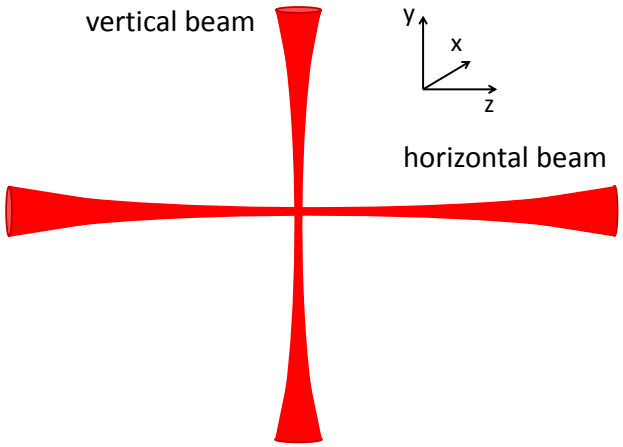

Figure 3.2: Schematic of two dipole trap beams crossed at an angle of 90°. The horizontal beam propagates along the z-axis and the vertical beam along the y-axis.

are the corresponding Rayleigh ranges of the horizontal and the vertical beam, respectively. $\hat{U}_1$ and $\hat{U}_2$ are the total trap depths for these beams. The harmonic approximation gives the following trap frequencies:

$$\begin{aligned}
\omega_{x,crossed} &\equiv \sqrt{\frac{4}{m}\left(\frac{\hat{U}_1}{w_{1x}^2}+\frac{\hat{U}_2}{w_{2x}^2}\right)}, \\
\omega_{y,crossed} &\equiv \sqrt{\frac{1}{m}\left(\frac{4\hat{U}_1}{w_{1y}^2}+\frac{2\hat{U}_2}{z_{R_{2,ell}}^2}\right)}, \\
\omega_{z,crossed} &\equiv \sqrt{\frac{1}{m}\left(\frac{4\hat{U}_2}{w_{2z}^2}+\frac{2\hat{U}_1}{z_{R_{1,ell}}^2}\right)}.
\end{aligned} \tag{3.28}$$

These equations point out two things:

- In the case of similar beam waists and powers of the two laser beams the confinement in the x-direction is the highest, because the radial confinement of each beam is added up.
- The confinement in the axial direction of one beam is mainly given by the second beam.

In the experiment the weakest confining axis plays the most significant role, because atoms can be lost in this direction. Therefore, the effective potential

depth is always determined by the axis with the smallest trap frequency.

Crossed beams at an angle

When the vertical beam is rotated, the confinement is also changed. The rotation can be described by two angles α and β. Their definition is given in Fig. 3.3. When both angles are 0° this model matches the discussion for crossed beams at 90°.

Tilting one beam does not change the total trap depth, but the influence of the beam waists and the Rayleigh range on each axis on the trap frequencies is different. To investigate this change we describe the trap geometry created by the beam propagating along the y-axis as an ellipse $\frac{x^2}{a^2}+\frac{y^2}{b^2}=1$ with boundaries $a = w_{2z}$ and $b = z_{R_{2,ell}}$. When this ellipse is rotated to the used coordinate system at an angle α, the new boundaries $\tilde{w}_0$ and $\tilde{z}_R$ on the x-, and y-axis have the following form:

$$\begin{aligned} \tilde{w}_{2z}(\alpha) &= \sqrt{\frac{1}{\frac{\cos^2(\alpha)}{w_{2z}^2}+\frac{\sin^2(\alpha)}{2z_{R_{2,ell}}^2}}}, \\ \tilde{z}_{R_{2,ell}}(\alpha) &= \sqrt{\frac{1}{\frac{\sin^2(\alpha)}{w_{2z}^2}+\frac{\cos^2(\alpha)}{2z_{R_{2,ell}}^2}}}. \end{aligned} \tag{3.29}$$

The factor 2 at $z_{R_{2,ell}}$ includes that the confinement in the axial direction is weaker than the radial confinement, which was already mentioned in Eq. (3.21). Figure 3.3(a) shows the tilt of the vertical beam to the axis of gravity, i.e. y-z-plane, and Fig. 3.3(b) indicates the rotation of the vertical beam in the plane perpendicular to the axis of gravity, i.e. x-z-plane. The calculation of the adapted boundaries for the angle β is done analogously. The only difference is that for this angle w_{2x} and w_{2z} have to be adapted. Note that for the calculation for angle β the new boundary from the calculation with angle α, hence $\tilde{w}_{2z}(\alpha)$, has to be taken into account. As a consequence the trap

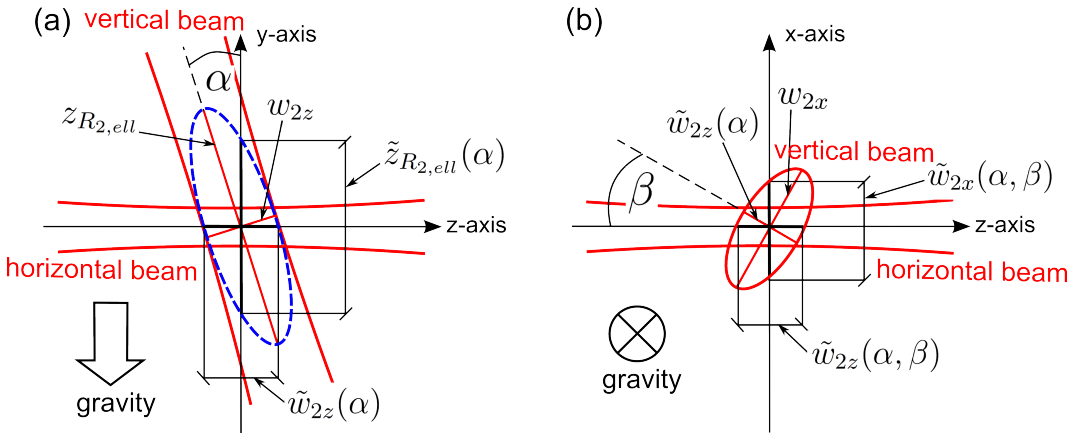

Figure 3.3: Definition of the angles embedded between the two beams. The horizontal beam (beam 1) propagates along the z-axis. The vertical beam (beam 2) in principle propagates along the y-axis. α defines the angle of the vertical beam to the axis of gravity in the plane spanned by the propagation direction of the horizontal beam and the direction of gravity. If α would be 90° the vertical beam would overlap with the horizontal beam. β defines the rotation of the vertical to the horizontal beam in the plane perpendicular to the axis of gravity. The change of the effective waists and the Rayleigh range of the vertical beam in the x-, y- and z-axis due to these two angles cannot be calculated independently.

frequencies transform to:

$$\begin{aligned}
\omega_{x_{\alpha\beta}} &\equiv \sqrt{\frac{4}{m}\left(\frac{\hat{U}_1}{w_{1x}^2}+\frac{\hat{U}_2}{\tilde{w}_{2x}^2(\alpha,\beta)}\right)},\\
\omega_{y_{\alpha\beta}} &\equiv \sqrt{\frac{4}{m}\left(\frac{\hat{U}_1}{w_{1y}^2}+\frac{\hat{U}_2}{\tilde{z}_{R_{2,ell}}^2(\alpha)}\right)},\\
\omega_{z_{\alpha\beta}} &\equiv \sqrt{\frac{1}{m}\left(\frac{4\hat{U}_2}{\tilde{w}_{2z}^2(\alpha,\beta)}+\frac{2\hat{U}_1}{z_{R_{1,ell}}^2}\right)}.
\end{aligned} \tag{3.30}$$

How the beam waists and the Rayleigh range of the tilted vertical beam are actually calculated can be found in Appendix B.

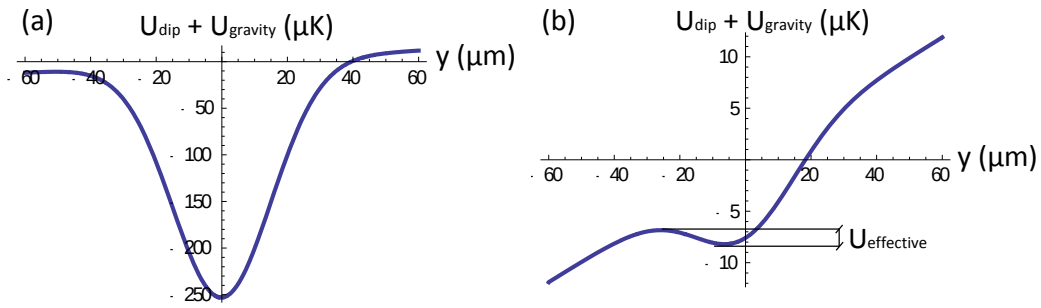

Figure 3.4: Influence of gravity on the trapping potential for different powers of the trapping laser beam along the plane $x = z = 0$. For this simulation we use a single circular beam with a waist w_0 of 30 μm and a power P of (a) 10 W and (b) 0.3 W. The trap depths correspond to the polarizability of bosonic erbium atoms. This simulation shows that the effect of gravity only becomes crucial for shallow trapping potentials.

Gravity

For low trap depths the gravitational force ($F_{grav} = mg$) can push the atoms out of the trap. m is the mass of the atom and g is the gravitational acceleration. It is important to know at which confinement this effect becomes relevant. Only the trap frequency ω_y has to be adapted.

Adding the gravitational potential ($U_{grav} = mgy$) to the dipole potential (U_{dip}) makes the effect visible. In Fig. 3.4 the tilt of the potential is shown for two different trapping configuration of a single beam. Figure (a) is for a 10 W circular laser beam with a waist w_0 of 30 μm and Fig. (b) shows the same beam for a power of 0.3 W. The shown trap depths are calculated for erbium atoms. The change of the trap frequency along the axis of gravity is described by the following equation:

$$\omega_{y_{\alpha\beta,\,gravity}} \equiv \sqrt{\frac{4}{m}\left(\frac{\hat{U}_{1,\,gravity}}{w_{1y}^2} + \frac{\hat{U}_{2,\,gravity}}{\tilde{z}_{R_{2,ell}}^2(\alpha)}\right)}, \tag{3.31}$$

where $\hat{U}_{1,\,gravity}$ ($\hat{U}_{2,\,gravity}$) describes the reduced effective trap depth of the horizontal (vertical) dipole trap beam due to the gravitational potential. The reduced trap depths are found numerically. Therefore, we compare the total trap depth with the maximum value of the combined potential in the direction of gravity. If the trapping potential is less steep than the potential of gravity, all atoms are lost out of the trap.

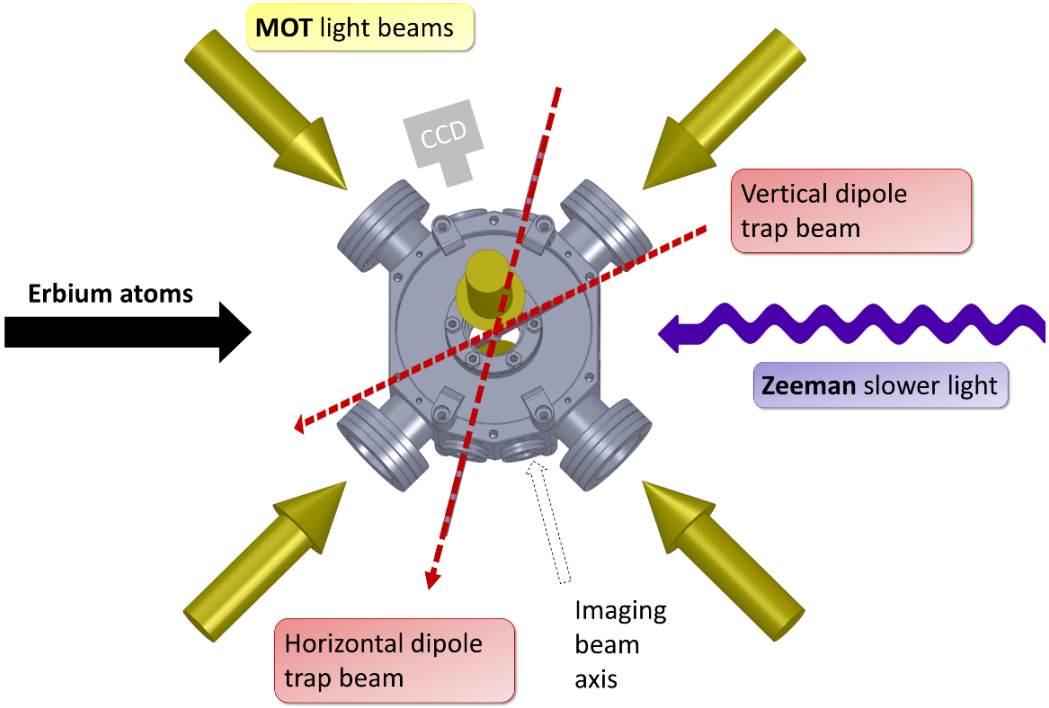

Figure 3.5: Scheme of the cooling and trapping setup in our experiment. For the Zeeman slower we use the strong 401-nm transition. The MOT operates on the narrow 583-nm transition. For the dipole trap we use 1064-nm laser light in a crossed configuration.

Real trap

In our experiment we use two crossed laser beams to create an optical dipole trap. The vertical beam has an angle of $\alpha = 15°$ as defined in Fig. 3.3. This angle is because of the limited space around the viewport, which is used for the vertical beam due to the MOT operation. Additionally the vertical beam is rotated by the angle $\beta = 14°$ in the plane perpendicular to the axis of gravity. This angle is because of the angle of the viewport, which is used for the horizontal dipole trap beam. The scheme of our cooling and trapping setup can be found in Fig. 3.5. The experimental implementation of the dipole trap beams will be discussed in detail in Sec. 5.1.3.

Figure 3.6 shows a simulation of the real trapping potential in our experiment. For this simulation we use a power of 1 W for the horizontal beam, and a power of 10 W for the vertical beam. The waists of the beams are specified in the caption of Fig. 3.6.

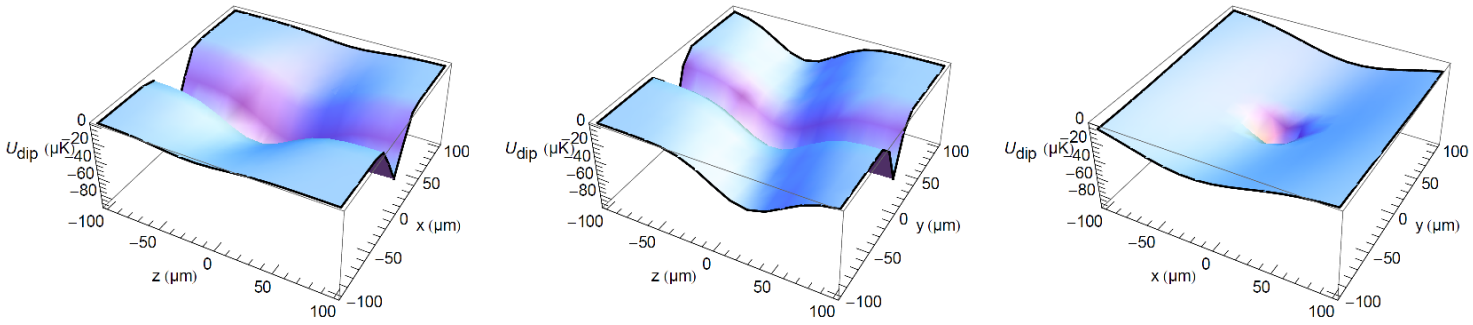

Figure 3.6: Trap potential of the crossed dipole trap in our experiment in all three coordinates. In this simulation the horizontal beam has a power of 1 W, a horizontal waist (x-axis) of 27 μm, and a vertical waist (y-axis) of 16 μm. The vertical beam crosses the horizontal beam under an angle $\alpha = 15°$ and $\beta = 14°$ because of the limited optical access in our experiment. The vertical beam has a power of 10 W, a horizontal waist (close to x-axis) of 110 μm, and a vertical waist (close to z-axis) of 55 μm. The direction of gravity coincides with the y-axis.

Chapter 4

Atomic polarizability of erbium

In this Chapter, we focus on the atomic polarizability of bosonic erbium atoms. For the bosonic isotopes the nuclear quantum number is zero and, therefore, no hyperfine splitting is observed. We briefly introduce the up-to-date knowledge of the energy level structure of erbium. Further, we give an estimate for the depth of the dipole trap potential for the ground state of erbium atoms. Additionally, we discuss the polarizability of the narrow-line transition at 583 nm and the strong 401-nm transition, which we use for the operation of the MOT and the Zeeman slower, respectively. We show the dependence of the trapping potential on the laser frequency ω and how the scattering rate depends on ω. Finally, we calculate the relevant parameters of an optical dipole trap for erbium atoms for a selection of technically feasible laser wavelengths.

4.1 Contribution of different energy levels

Erbium has a very rich energy spectrum; see Sec. 2.2. The electronic ground state of erbium is in a $[\mathrm{Xe}]4f^{12}6s^2(^3H_6)$ configuration. This state has a total angular momentum quantum number J of 6 and an even parity. From the NIST Atomic Spectra Database [Ral11] there are 672 excited states known with J values ranging from 1 to 12. The energy of the excited states in relation to the ground state ranges from 5035 to 46971 cm^{-1}. From these levels only 144 can couple to the ground state via optical dipole transition; see Sec. 3.1.2. In the case of erbium electrons can only be excited to levels with odd parity and J values ranging from 5 to 7. These dipole allowed transitions are shown in Fig. 4.1.

We have an intense collaboration with J.-F. Wyart and the group of O. Dulieu at the Laboratoire Aimé Cotton in Orsay, France, which have derived transi-

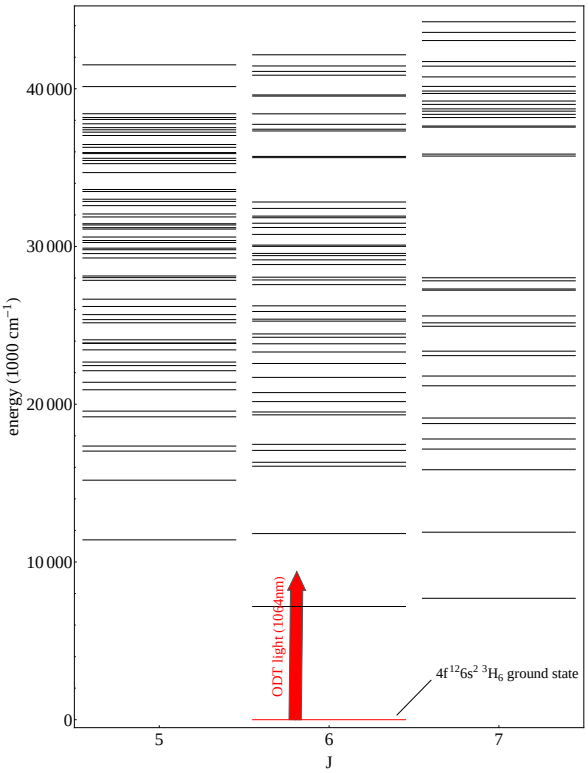

Figure 4.1: Energy of all levels which can couple to the ground state $4f^{12}6s^2(^3H_6)$ due to the selection rules for electric dipole interaction. The shown energy spectrum is incomplete, since to date not all energy levels in erbium are known. The red arrow shows the energy of the used dipole trap laser. For a low scattering rate of dipole trap photons it is important, that the detuning to the excited states is large. In particular, the detuning to the strongest transition should be as large as possible. In our experiment a 1064-nm laser source was chosen for the creation of the dipole trap. The data were taken from [Ral11].

tion probabilities for many levels of erbium [Law10]. The data are the result of combined spectroscopic measurements and calculations. Experimental data are derived by combining branching fractions measured with a Fourier transform spectrometer with radiative lifetimes from time-resolved-laser-induced-fluorescence measurements. The calculations use parametric fits based on the Cowan code [Cow81] and can also predict unobserved levels. The calculations are than rescaled by using the observed levels as a reference value. The theoretical energies can be extracted from fitted parameters. Those values minimize the root mean square of the difference between the experimentally observed

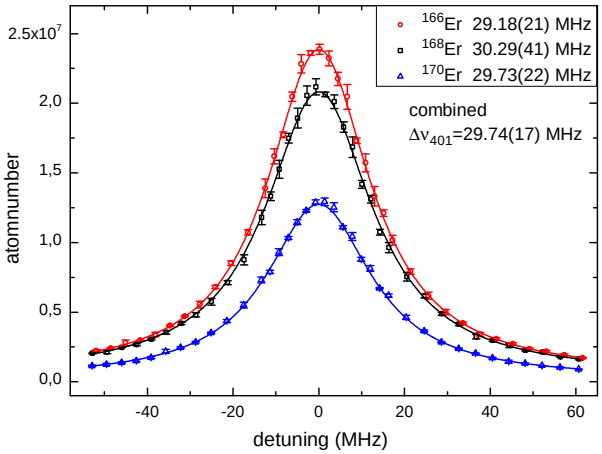

Figure 4.2: Natural linewidth $\Delta\nu_{401}$ of the strong 401-nm level. The quantity $\Delta\nu_{401} = 29.74(2)$ MHz was measured in our experiment by using an absorption imaging technique. The atom number was measure versus the detuning of the imaging light for three different isotopes (^{166}Er, ^{168}Er, ^{170}Er). The data were fitted by a Lorentzian function and the arithmetic mean of the linewidths is taken to extract the actual linewidth. The temperature for the measurements was in the range between 11 and 15 μK.

and the theoretically calculated energies of the excited states. This is done for all considered experimental energies.

Newest calculations predict 1176 excited levels that can couple to the ground state [Wya12]. This new data set provides indeed more transitions, however, compared to [Ral11] there are also levels missing[1]. The new set of data also includes the experimental values for the linewidths $\Delta\nu = \Gamma/2\pi$ of the 401-, and the 583-nm state. Because of the complexity of the atomic spectrum, the knowledge of the transition linewidths is not very precise. For instance, even one of the strongest erbium transitions, located at 401 nm, was overestimated by 20 %. The group of McClelland et al. [McC06a] has measured a linewidth of $\Gamma_{401}/2\pi = 35.6$ MHz. This measurement was done via fluorescence spectroscopy on atomic beams. Lawler et al. [Law10] found a value of $\Gamma_{401}/2\pi = 29.5$ MHz from lifetime measurements. We measure a linewidth of 29.74(2) MHz by using an absorption imaging technique on magneto-optically trapped atoms; see Fig. 4.2. This little historical excursus shows exemplary how difficult it is to determine all the levels in erbium and their corresponding linewidths precisely. The linewidth of the 583-nm state is $\Gamma_{583}/2\pi = 190$ kHz.

[1] In the new set of data transitions with linewidths below 100 Hz are excluded, which explains the missing levels.

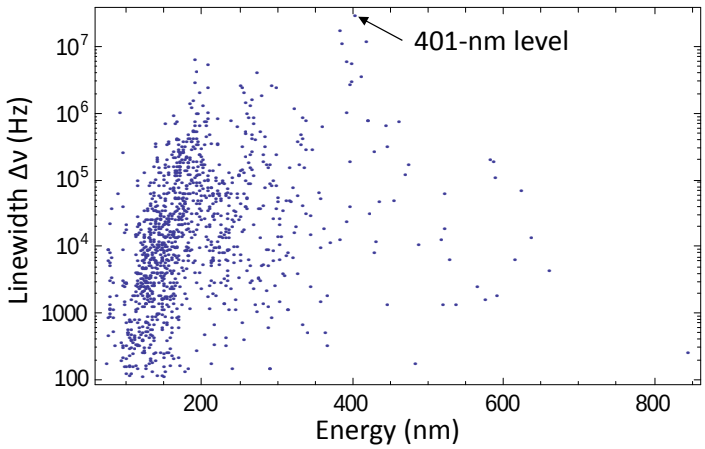

Figure 4.3: Natural linewidth $\Delta\nu$ of all relevant excited states versus the corresponding energy difference between the ground state $|g\rangle$ and each excited state $|e\rangle$ [Wya12].

Figure 4.3 shows the energies of the 1176 states plotted to their corresponding natural linewidths $\Delta\nu$. The strong 401-nm transition has the broadest linewidth. The detuning of the laser trapping light is always given with respect to this level because it is the strongest transition in erbium. Dipole traps with lower (higher) laser energies relative to this level are called red-detuned (blue-detuned) traps. Most of the excited levels in erbium are located in the high energy[2] region below 300 nm. From these data one can already realize that a laser emitting at a wavelength above 900 nm will give a low scattering rate, because the detuning to most of the levels is large. A more detailed discussion on the dependence of the dipole force on the used laser wavelength is given in Sec. 4.2.

As previously discussed, all the dipole allowed transitions contribute to the overall trapping potential according to their line strength factors. However, the polarizability strongly depends on the linewidth $\Delta\nu$, making the weight of narrow transitions less an less important; see discussion below. Based on the new data set, we derive the atomic polarizability following Eq. (3.18). For linear polarized laser light at 1064 nm, we find

$$\tilde{U}_{|g\rangle} = -4.9384 \cdot 10^{-37}\,\mathrm{Jm}^2/\mathrm{W}.$$

[2]The energy E is correlated to the wavelength λ with $E = \frac{\hbar c}{\lambda}$.

In atomic units[3] this value converts to:

$$\mathrm{Re}(\alpha_{|g\rangle}) = 159.01\,\mathrm{a.u.}$$

The derived value already takes the scalar and tensorial part of the polarizability into account. For the ground state of erbium atoms the tensorial part does not have a big influence on the polarizability. We can now calculate the resulting dipole potential and potential depth. For a Gaussian laser beam of $30\,\mu$m waist and a power of 10 W, we find a potential depth for atoms in the ground state of

$$\hat{U}_{|g\rangle} = -253.01\,\mu\mathrm{K}^4.$$

Figure 4.4 shows the contribution of all dipole allowed transitions to the overall trapping potential of the ground state. In Sec.6.1.2 we use trap frequency measurements to extract the dynamic polarizability of erbium experimentally and compare it to the derived theoretical value.

There are 4 (34) excited states with a natural linewidth $\Delta\nu > 10$ (1) MHz. The coupling to these states already gives a contribution to the trap depth of 62.7 (84.1) %. The contribution of the strongest line (401-nm) is 11.1 %. This shows that mainly the strong lines contribute to the dipole trap potential.

For a deeper understanding of the trapping behavior of erbium atoms, it is necessary to know the polarizability of specific excited states. From particular interest are the 583-nm and the 401-nm state. These are the transitions at which the MOT and the Zeeman slower are operated and hence atoms can populate these levels. For these calculations the excited state is treated as a ground state, where all allowed transitions of this state can contribute to the energy shift. Energy levels located below this excited state will increase the energy, while energy levels located above this state will decrease the energy.

Fig. 4.5 shows the resulting shift of the 583-nm state due to the laser light. The shift of the 401-nm state is shown in Fig. 4.6. The dynamic polarizabilities for a linear polarized 1064-nm laser light are found to be:

$$\tilde{U}_{583} = -9.0164 \cdot 10^{-39}\,\mathrm{Jm}^2/\mathrm{W},$$

$$\tilde{U}_{401} = -1.3633 \cdot 10^{-38}\,\mathrm{Jm}^2/\mathrm{W}.$$

In atomic units this corresponds to

$$\mathrm{Re}(\alpha_{583}) = 2.90\,\mathrm{a.u.},$$

[3]The conversion factor to atomic units is $\mathrm{Re}(\alpha) = -\tilde{U}2\epsilon_0 c\cdot/(1.6488\cdot 10^{-41})$; see Eq. (3.2) and [Sch06].

[4]To convert the dipole potential to the temperature scale, one has to divide the effective potential depth by the Boltzmann constant k_B.

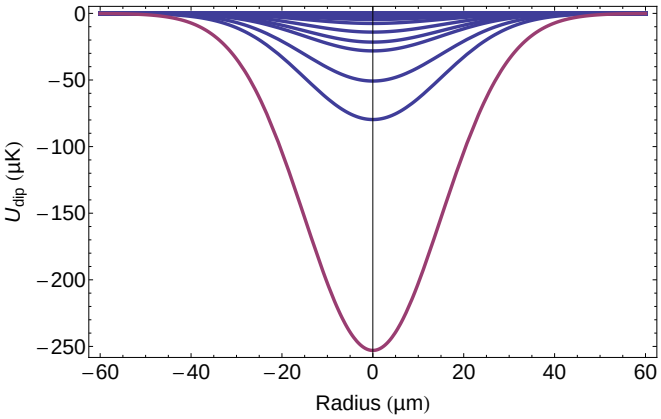

Figure 4.4: Dipole trap depth for a spherical 1064 nm laser beam with waist $w = 30\,\mu$m and power $P = 10\,$W for the ground state of erbium atoms. The blue curves are the contribution to the trap depth of each dipole allowed transition, which is related to their linewidths and line strength factors. The purple curve is the total trapping potential.

$$\mathrm{Re}(\alpha_{401}) = 4.39\,\text{a.u.}.$$

For the modeled laser beam the polarizabilities correspond to total trap depths of

$$\hat{U}_{583} = -4.62\,\mu\text{K},$$
$$\hat{U}_{401} = -6.98\,\mu\text{K}.$$

Unfortunately for these states only eight and three transitions are known, respectively [Law10]. Therefore, the calculated polarizabilities might not be correct. For the excited states it is expected that the tensorial part of the polarizabilities plays a more significant role. The scalar part only depends on the intensity of the electric field, whereas the tensorial part also depends on the direction of the electric field compared to the direction of the quantization axis of the atoms [Ang68]. The influence of the tensorial part on the total polarizability can be huge, as shown recently for ^{40}K^{87}Rb molecules [Ney12]. To determine a complete set of dipole allowed transitions of the discussed excited states will be part of future theoretical investigations.

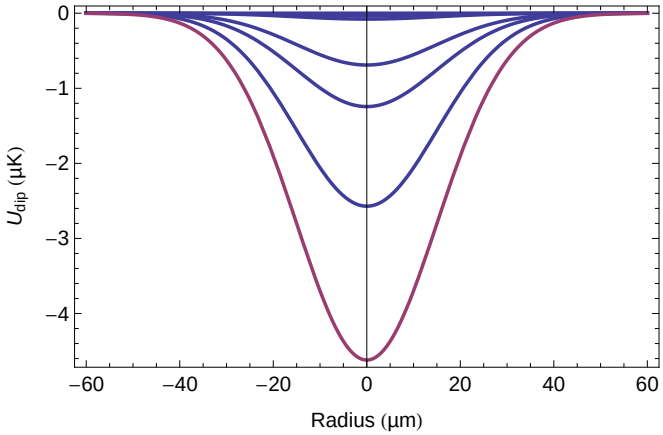

Figure 4.5: Dipole trap depth for a spherical 1064 nm laser with waist $w = 30\,\mu$m and power $P = 10\,$W for the 583-nm state of erbium atoms. The blue curves are the contribution to the trap depth of each dipole allowed transition to the 583-nm state. The purple curve is the total trapping potential.

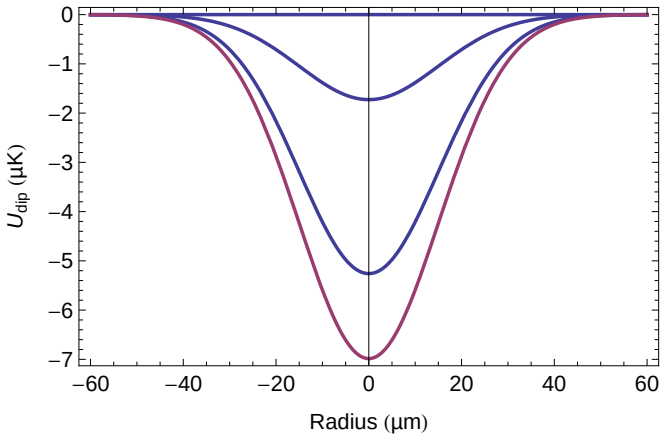

Figure 4.6: Dipole trap depth for a spherical 1064 nm laser with waist $w = 30\,\mu$m and power $P = 10\,$W for the 401-nm state of erbium atoms. The blue curves are the contribution to the trap depth of each dipole allowed transition to the 401-nm state. The purple curve is the total trapping potential.

4.2 Dependence on the laser wavelength

To calculate the dependence of the total trap depth $\hat{U}_{dip}$ on the used laser wavelength λ_{laser} we use Eq. (3.13) and change $\lambda_{laser} = \frac{2\pi c}{\omega}$ from 200 to 1100 nm. The result is shown in Fig. 4.7. In the red-detuned region (700-1100 nm) the

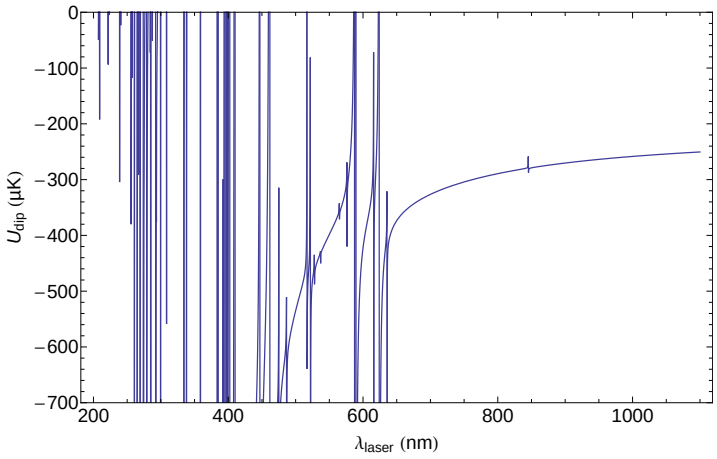

Figure 4.7: Dependence of the total trapdepth $\hat{U}_{dip}$ on the used laser frequency λ_{laser} ranging from 200 to 1100 nm. For this calculation the model of a single beam ODT with 30 μm waist and 10 W is used. This example gives an estimate about the created trap depth in μK. The vertical lines show the asymptotic behavior of $\hat{U}_{dip}$ when the wavelength is resonant to an atomic transition.

total trap depth increases for smaller detunings as expected from Eq. (3.18). Every time the wavelength coincides with one of the levels in erbium the contribution of this level to the total trap depth approaches infinity. This leads to an asymptotic behavior when the energy of the laser is close to an excited state. For wavelengths between 200-700 nm the behavior of the total trap depth gets more complicated. In this region the laser is to some lines red-detuned and to the other lines blue-detuned, leading to a deepening or steepening of the trapping potential. Below the strong 401-nm line the trap depth is positive, leading to the repulsive trapping behavior, as discussed in Sec. 3.1.

Furthermore, we simulate the dependence of the scattering rate Γ_{sc} on the laser wavelength using Eq. (3.14). Figure 4.8 shows the strong $1/\Delta^2$ correlation of the scattering rate on the detuning. In the region close to the 401-nm line the scattering rate gets extremely large, making it impossible to trap atoms by means of optical dipole traps.

For experimental reasons the heating rate of the laser, which stems from the scattering of photons generating the dipole trap, is from interest. In the far-detuned case this scattering is an elastic process. Therefore, the energy transfer is determined only by the energy $\hbar k_{laser}$ of the scattered photon, which is related to the wavelength of the laser. The overall heating increases the total thermal energy by $2E_{rec}$ per scattering event, where $E_{rec} = (\hbar k_{laser})^2/2m$ is the

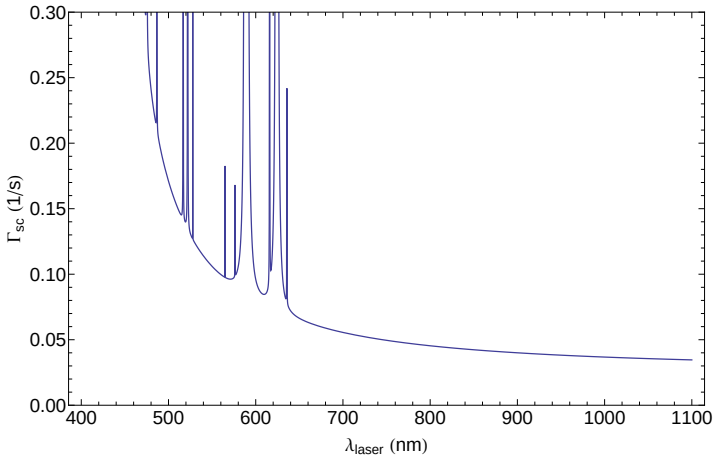

Figure 4.8: Dependence of the scattering rate Γ_{sc} on the used laser wavelength λ_{laser} ranging from 400 to 1100 nm. For this calculation the model of a single beam ODT with 30 μm waist and 10 W is used. The smaller the detuning to the main transition (401-nm line) is, the larger becomes the scattering rate. For wavelengths below this line (blue detuning) the scattering rate is not relevant. In this blue-detuned case atoms are pushed out of the laser beam, as discussed in Sec. 3.1. Therefore, scattering processes hardly occur.

recoil energy and is related to the recoil temperature by $T_{rec} = 2E_{rec}/k_B$. For a red-detuned 3D harmonic trap the heating rate can be expressed as [Gri00]:

$$\dot{T}_{red} = \frac{1}{3} T_{rec} \Gamma_{sc}. \tag{4.1}$$

In the blue-detuned case atoms are located in the intensity minimum and the potential depth is determined by the height of the surrounding walls. Such a confinement can be created for example by a blue-detuned optical lattice. The heating rate $\dot{T}_{blue}$ is given by [Gri00]

$$\dot{T}_{blue} = \frac{3}{2} \frac{k_B T}{\hat{U}} \dot{T}_{red}, \tag{4.2}$$

where $\hat{U}$ is the total trap depth and T is the temperature of the trapped atomic sample. In Tab. 4.1 we simulate different dipole trap parameters for a single spherical beam with 30 μm waist, 10 W power, and an atom cloud temperature of 1 μK for different laser wavelengths. The considered wavelengths are not resonant with one of the excited states in erbium and are technically feasible. For each laser wavelength we calculate the recoil temperature, the dynamic polarizability, the effective potential depth, the scattering rate and the heating rate for the red- and the blue-detuned case.

Table 4.1: Calculation of dipole trap parameters for a selection of technically relevant laser wavelengths. The values are derived for a single beam with 30 μm waist, 10 W power, and an atom cloud temperature of 1 μK.

laser wavelength λ_{laser} (nm)	recoil temperature T_{rec} (K)	dynamic polarizability Re(α) (a.u.)	potential depth U_{dip} (μK)	scattering rate Γ_{sc} (1/s)	heating rate red detuned $\dot{T}_{red}$ (nK/s)	heating rate blue detuned $\dot{T}_{blue}$ (nK/s)
1064	101.9	159.01	-253.01	0.04	1.20	
532	407.6	281.12	-447.32	0.12	16.55	
355	915.4	-529.28	842.18	0.87	265.31	0.47
300	1281.8	-23.55	37.47	0.12	50.34	2.02
266	1630.4	-158.99	252.97	0.12	64.74	0.38

Chapter 5

Setup of a flexible optical dipole trap for erbium

In the previous chapters we reported on the polarizability of erbium atoms. From this knowledge we can estimate the trap depth and trap frequencies for various geometries of a dipole trap. Based on this knowledge, we are now able to design an optimal dipole trap for erbium.

The main challenge is to find a configuration able to assure both, an optimal loading of atoms from the MOT to the dipole trap and a high efficiency during the evaporative cooling. To match these requirements, we have chosen to build an optical dipole trap based on a time averaged potential. With this technique we can dynamically change the effective beam waist of the trapping beam and thus realize a tunable and flexible confinement. In addition, a number of interesting effects in the quantum regime are expected to strongly depend on the trap geometry and on the trap aspect ratio AR. These effects include, for instance, the roton instability [San03, Bla12] and the quantum-fluctuation-driven expansion [Lim11]. With our tunable dipole trap, we can have access to these interesting phenomena.

The total number of atoms, which can be loaded from the magneto-optical-trap (MOT) to the dipole trap, is significantly determined by the spatial overlap of these two traps. Based on mode-matching arguments, the larger the overlap is, the more atoms will be loaded to the dipole trap. For this process a large beam size of the trapping laser beam is needed.

After atoms are loaded to the dipole trap, forced evaporation begins. The trap depth is lowered by decreasing the intensity of the dipole trap beam. Thus, the hottest atoms are lost out of the trap and the remaining atoms thermalize to a lower final temperature via elastic collisions. For this process the collisional rate between atoms is crucial. This rate is in principal determined by three

parameters. One parameter is the scattering length a, which is an intrinsic property of an atomic isotope. Further, the mean relative velocity of the atoms changes the collisional rate. Finally, the density determines how often atoms collide per time. The density can be tuned by changing the geometry of the trap. This gives a versatile tool to adjust the collisional rate, thus leading to efficient evaporative cooling. By changing the shape of the trapping potential we can address both conditions, a large overlap of the MOT and the dipole trap and a tunable density. This leads to an increased controllability of the atoms.

To realize this tunable dipole trap we build a scanning system, which allows to change the waist of one dipole trap beam in one axis. The idea of this scanning system was already realized in different teams of our group [Sch07, Koh07].

5.1 Scanning system

For the scanning system we use an acousto-optic-modulator (AOM)[1]. The AOM consists of a crystal and diffracts a laser beam using sound waves. The frequency of the sound waves f_{AOM} defines the angle of deflection. When a lens is positioned after the AOM in the distance of the focal length, the diffraction is translated to a parallel displacement of the beam. This is only true when the beam is passing the AOM collimated. f_{AOM} can be varied within the bandwidth BW_{AOM} of the AOM, leading to a different displacement of the beam. When f_{AOM} is tuned fast enough, compared to the trap frequencies, the scan of the beam leads to a time-averaged potential for the atoms. Figure 5.1 shows the schematic of the scanning system.

5.1.1 Requirements on the scanning system

From previous measurements at our experiment we know that a beam waist of about 30 μm leads to efficient evaporative cooling of the ^{168}Er isotope [Aik12]. The loading efficiency at this beam waist from the MOT to the dipole trap is about 2 %.

With the new dipole trap we aim to increase the loading efficiency. Here we consider a single beam configuration for the dipole trap. We use an elliptic beam with waist in horizontal direction x of around 25 μm and waist in vertical

[1] We use the model 3110-197 from Crystal Technology, Inc, which has a center frequency f_{center} of 110 MHz and a bandwidth BW_{AOM} of $\pm$15 MHz. The numerical aperture of this model is 3 mm.

direction y of around 15 μm. The waist in horizontal direction can be increased by the scanning system. The ellipticity of the beam is defined as aspect ratio

$$AR = \frac{w_x}{w_y} = \frac{\omega_y}{\omega_x}, \tag{5.1}$$

where w_x and w_y are the horizontal and vertical beam waists[2], respectively. The quantities ω_x and ω_y are the corresponding trap frequencies along the horizontal and vertical direction, as defined by Eq. (3.26).

The AR will then be changed by our scanning system. The maximal possible AR is limited by the resolution $R = \frac{D}{w_a}$ of the AOM. D is the distance by which the center of the beam can be deflected within the bandwidth of the AOM and w_a is defined as the beam waist after the lense; see Fig. 5.1. The resolution only depends on the initial waist w_i of the beam in the AOM and on intrinsic properties of the AOM [Koh07]:

$$R = \frac{2\pi}{4c_s} w_i BW_{AOM}. \tag{5.2}$$

For our AOM the speed of sound c_s is 4200 m/s and BW_{AOM} is 30 MHz. The resolution does not depend on the focal length of the used lens and cannot be changed by implementing a telescope after the AOM. The largest beam waist w_i, which can pass through the AOM is limited by the numerical aperture of the AOM and is about 700 μm. This configuration would give a resolution R of about 8. With this resolution the horizontal waist w_x at the chamber could be tuned from 25[3] to 200 μm, leading to aspect ratios in the range of 1.5 to 13.

An important requirement on the scanning system is the modulation frequency ω_{mod}. This frequency defines how fast the frequency of the AOM f_{AOM} is tuned. Only if the modulation is fast enough, atoms will not follow the change of the potential. This so called time-averaged potential is typically created for modulation frequencies ω_{mod} 100 times larger than the trap frequency ω_x. In this case no heating of the atomic cloud is expected.

5.1.2 Technical realization

To realize the required scanning system the driver of the AOM is adapted. The scheme of the electronic setup is shown in Fig. 5.2. For the creation of an elliptic Gaussian beam we control the frequency of the AOM as follows:

[2]In the following discussion w_x (w_y) is always used for the horizontal (vertical) beam waist at the focal point in the chamber, at the position where atoms are trapped.

[3]The lenses used to achieve this beam waist are shown in Fig. 5.3.

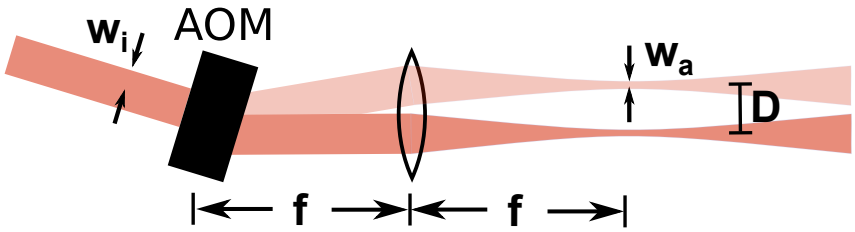

Figure 5.1: Shown is the basic principle of the scanning system. An AOM diffracts a collimated beam depending on the frequency of sound waves f_{AOM} in the AOM. f_{AOM} can be tuned around the center frequency f_{center} and within the bandwidth BW_{AOM} of the AOM. A lense having a distance of its focal length f to the AOM translates the deflection to a parallel displacement of the beam. The bright and the flat beams show exemplary the diffraction for different frequencies of the sound waves. A fast sweep over different frequencies leads to an elliptic beam. The ellipticity depends on the range of the sweep.

- The angle of deflection is determined by the frequency of sound waves f_{AOM} in the AOM. This frequency is given by a voltage controlled oscillator (VCO). Depending on the input voltage of the VCO the output frequency can be changed.
- The voltage U_{mod}, which controls the VCO, is created by a mixer[4]. U_{mod} is determined by three different parameters:

$$U_{mod} = U_{offset} + \frac{U_{signal}\, U_{gain}}{10\,\mathrm{V}}. \tag{5.3}$$

- U_{offset} is used to adjust the central working frequency of the VCO to the center frequency $f_{center} = 110\,\mathrm{MHz}$ of the AOM. The used VCO has a working range of 75-150 MHz. 110 MHz correspond to an input voltage of 7.6 V. With this voltage one can also displace the atom cloud dynamically for, e.g., trap frequency measurements.
- U_{signal} is created by an external frequency generator. This signal defines the shape of the modulation signal U_{mod} and, therefore, determines the shape of the scanned beam. In previous experiments an arcus-cosine-function[5] has proved to be suited for the creation of a Gaussian shape

[4] We used the model AD 734 from Analog Devices; see Appendix A.

[5] As frequency generator we use the model Agilent 33522A. We create the desired function with MATHEMATICA, scale it to a 16 bit amplitude resolution and write the values in a text file. This file is loaded to the Agilent via a USB-stick. The Agilent 33522A has a maximum sampling rate of 250 MSa/s. The number of samples written to the text file determines the maximum frequency. In our case we choose 252 samples and obtain a maximum frequency of $\omega_{mod}^{max} = 2\pi \cdot 0.992\,\mathrm{MHz}$.

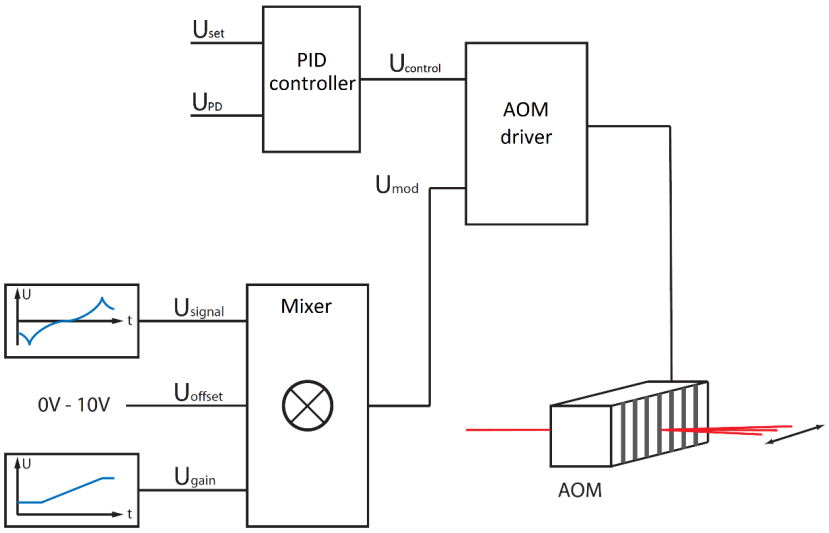

Figure 5.2: Scheme of the electronic setup of the scanning system. To control the deflection and the power of the dipole trap beam, we use the AOM-driver. The signal U_{mod}, which determines the potential form of the dipole trap is created by a mixer. This signal is sent to the frequency input of the AOM-driver and controls the radio frequency f_{AOM} created by a voltage controlled oscillator. The deflection of the beam depends on this radio frequency. The power of the beam is controlled by a PID controller, which compares the set voltage U_{set} with the actual voltage U_{PD} monitored with a photo diode. $U_{control}$ regulates the power of the AOM.

[Koh07]. The voltage of this signal is set to $10\,V_{pp}$. By using a different function one can create an arbitrary trapping geometry, e.g. a box-potential or a double-well-potential.

- U_{gain} defines the amplitude of U_{mod}. This parameter gives the knob to tune the AR of the trap during the experimental cycle online. A voltage of 1 V corresponds to a sweep of 6 MHz.

The power of the dipole trap beam is monitored by a photodiode and compared to the set value U_{set} by a PID-controller. The set value is given via the experiment control system. The PID-controller regulates the power of the signal, which is sent to the AOM. Less power corresponds to a less efficient diffraction, thus more power is lost to the 0^{th} order of the AOM. The power of the 1^{th} order is adjusted until it reaches the set value. The photo diode only monitors the fraction of the power of the beam, which is lost through a mirror.

The voltage of the photo diode U_{PD} has to be calibrated to the actual power of the beam in the experimental chamber.

5.1.3 Implementation in the experiment

To find the optimal configuration of lenses and beam waists to create the required dipole trap beam we built up a test setup. A copy of the optimized setup was then built at the experiment table.

We use a 1064-nm light with a power of 42 W, generated from a single frequency diode-pumped solid-state laser[6]. Figure 5.3 shows the final setup for the horizontal dipole trap beam. We put the laser system directly on the experiment table. The advantage is that we can avoid the use of optical fibers, which limit the final power, while the disadvantage is that the spatial mode of the laser light is not "cleaned" by a fiber.

To avoid back reflection into the laser from optical elements, we place a Faraday-isolator right after the laser. The transmission was optimized to 90.2 %, which is equal to 38 W. The beam is diverging after the laser and can be collimated by inserting a lens[7] with a focal length of 1000 mm at around 109 cm after the output of the laser.

For the designing of the setup after the AOM, we have to consider the following technical facts:

- Due to the vacuum chamber the focal length of the last lens cannot be smaller than $f = 150\,\text{mm}$.
- The beam at the AOM has to be collimated and as large as possible to achieve a large aspect ratio.
- Each distance between the lenses after the AOM has to be the sum of their own focal lengths to maintain the parallel displacement of the beam.

This leads to the setup shown in Fig. 5.3. The lenses f_2 and f_3 are used as a telescope to adjust the beam size. The cylindrical lenses $f_{cyl,1}$ and $f_{cyl,2}$ only change the beam size of the vertical beam axis and do not affect the waist of the scanned axis. Since we produce an elliptic beam, the focal points of the x- and y-axis after the last lens do not coincide. This can be adjusted by changing the distance between the two cylindric lenses.

[6] This laser is a Mephisto MOPA from InnoLight. The spatial mode of the laser light strongly depends on the injection current of the laser amplifier. Therefore, the calibration of the beam and its beam waist should only be done, when the laser is working on maximum power.

[7] Due to the high power we use Fused Silica lenses with a coating for 1064-nm light. The lenses are from LENS-Optics, GmbH and LASER COMPONENTS, GmbH.

The optimized overall optimized efficiency through the AOM is 75 %. This relative small percentage is related to the beam size, which is too large for the numerical aperture of the AOM[8]. The diffraction efficiency between the 0^{th} and the 1^{th} order is 90 %. Because the space after the last lense is limited, we place a flip-mirror after the cylindrical lenses and copy the setup to measure the beam size and the power "in the chamber". At the window of the vacuum chamber 13 % of the power is lost due to reflections. The maximum power at the chamber is 18 W. For the beam waists at the chamber we obtain $w_x = 24\,\mu$m and $w_y = 17\,\mu$m, respectively.

The technical limitations of our scanning system will be discussed in the following Section. To obtain the desired performance some of the electronic parts had to be exchanged.

5.1.4 Technical limitations

The performance of the scanning system is determined by the following parameters:

Scanning range: The range of the scanning system sets the maximum achievable aspect ratio of the scanned beam, as already discussed in Sec. 5.1.2. The range is technically limited by BW_{AOM} and depends thus on the AOM performance as specified by the manufacturer.

Modulation frequency: A modulation frequency ω_{mod} of about 100 times ω_x is needed to create a time-averaged-potential. The modulation frequency is limited by the speed of the VCO that creates the radiofrequency signal. The used AOM-driver is designed for a usage of the POS 150 from Mini-Circuits; see Appendix A. For a scanning range of 30 MHz the 3dB-modulation bandwidth was measured to be roughly $2\pi\cdot100$ kHz. For higher modulation frequencies the range of the scanned frequency f_{AOM} decreases. From the calculations discussed in Sec. 3.3 we expect trap frequencies ω_x of up to $2\pi\cdot2$ kHz, for the used laser beam; see Sec. 5.2. Therefore, we exchange the POS 150 by the model VCO190-112T from Varil. With this model we can achieve a modulation bandwidth of up to 1 MHz. In Sec. 5.2 the performance of the new VCO will be discussed.

Shape of scanned radio frequency signal: By testing the finished electronic box we discovered, that the power shape, monitored by a spectrum analyzer, strongly depends on $U_{control}$. This voltage controls the power of

[8]In a further optimization step we implement a 2:1 telescope before the AOM. With the new, smaller beam waist w_i the efficiency through the AOM increases to 90 %, leading to a higher laser power at the chamber. The quantity for beam waists and power discussed in this Chapter refer to the first setup.

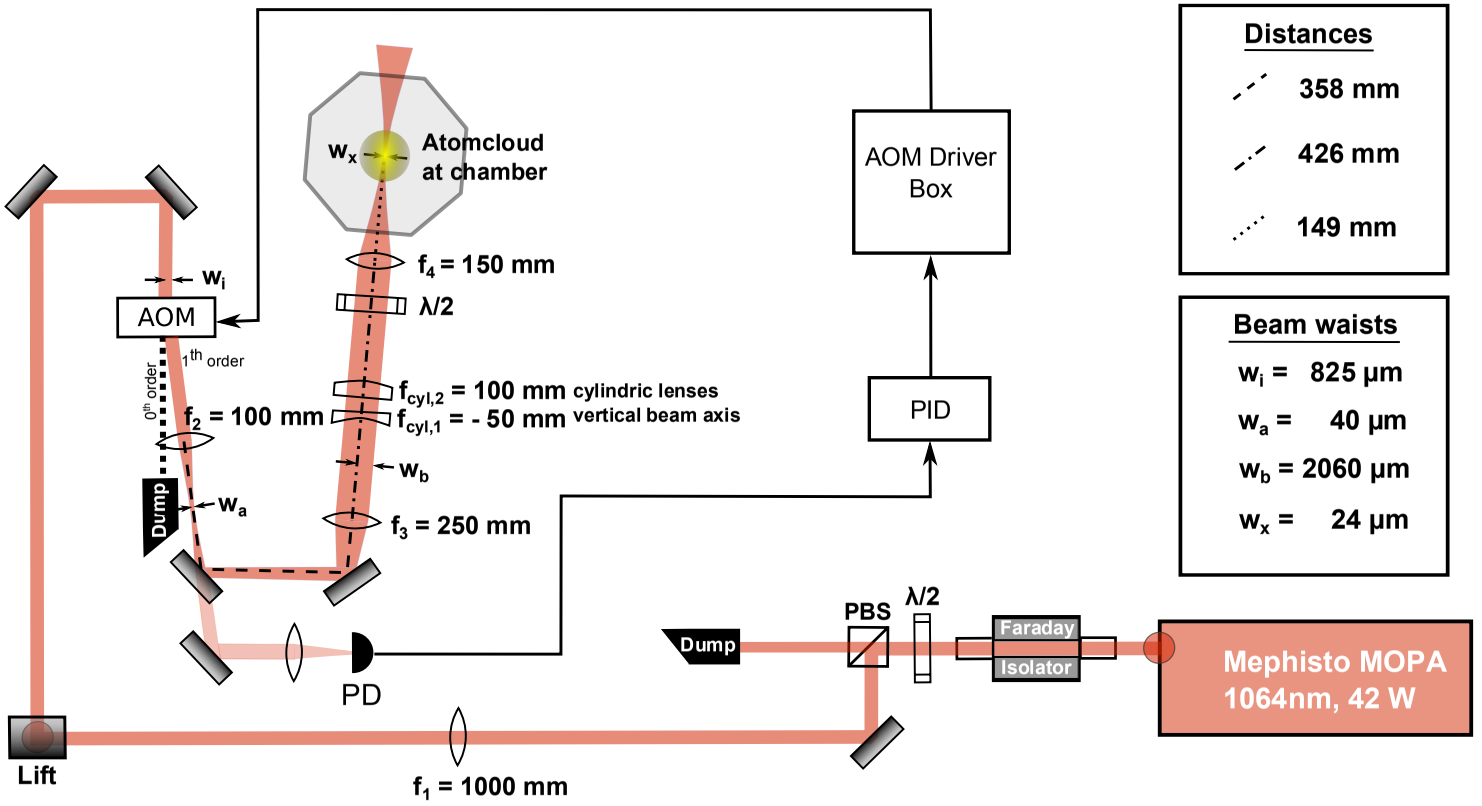

Figure 5.3: Optical setup for the dipole trap scanning system. The setup of the lenses is designed to fulfill our requirements on the scanning system. The distances between the crucial lenses are depicted by the dashed, dashed-dotted, and dotted line. The initial beam waist at the AOM is 825 μm along both, x- and y-direction. The final beam waists at the chamber are $w_x = 24\,\mu$m and $w_y = 17\,\mu$m, respectively.

the radio frequency signal. For the maximum power of 2 W, which corresponds to 33 dBm, the scanned signal had roughly the same power at each frequency. However, for a lower $U_{control}$ the power distribution over the scanned frequency range showed a strange shape. Some frequencies maintained the set value of the power, where other frequencies had by far a lower power. The problem could be traced to components of the AOM-driver. To fix this problem we bridged the TTL-switch OPA693, the preamplifier ERA4-SM and the amplifier MHW9267. This components were replaced externally (outside the box) by coaxial components from Mini-Circuits. As TTL-switch the model ZASWA-2-50DR is used. For the preamplifier we use the model ZFL-500LN+ and for the amplifier the model ZHL-1-2W is implemented. The overall gain is 34 dBm. With the new components a sufficient shape of the power to frequency profile in scanning mode for different $U_{control}$ and U_{gain} could be achieved. In Fig. 5.4(a) the shape of the scanned frequency monitored by a spectrum analyzer is shown for a selection of U_{gain}. This Figure also shows the translation of the scanning range on the actual beam size; see Fig. 5.4(b) and (c). Deeper investigation on the overall performance of the scanning system follow in Sec. 5.2.

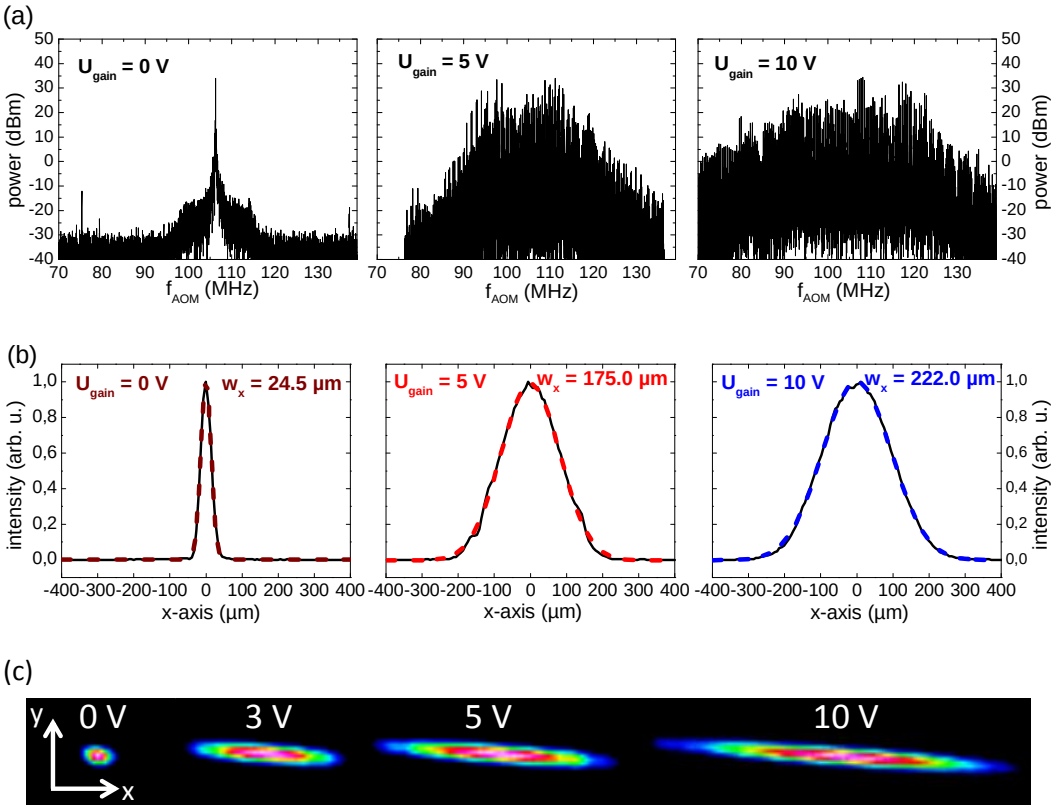

Figure 5.4: Scanned radio signal that is sent to the AOM monitored by a spectrum analyzer (a) and overall performance of the scanning system (b) and (c) for a selection of scanning gains U_{gain}. For this measurement the modulation frequency ω_{mod} was fixed to $2\pi \cdot 200\,\mathrm{kHz}$. In (a) one can see the shape of the scanned radio frequency in terms of power (dBm) for $U_{gain} = 0\,\mathrm{V}$, $5\,\mathrm{V}$, and $10\,\mathrm{V}$. Due to the arcus-cosine-scanning-function the scanned range does not have sharp edges. The scanned radio signal is translated by the AOM to the beam size; see Figures (b) and (c). The profiles of the scanned beam fit nicely to a Gaussian beam function. At the edges of the bandwidth BW_{AOM} of the AOM the diffraction efficiency decreases, what finally limits the maximum beam size. The angle between the scanning axis and the x-axis is due to a slight tilt of the AOM.

5.2 Offline characterization

Beam profile measurements

For the characterization of the laser beam one of the most crucial points is the measurement of the beam profile. This can be particularly demanding for the small beam waists we are using for our dipole trap. We compare three different technical applications to measure the waist of a focused beam. For all methods the beam profile at various points along the propagation direction is determined. From a fit with a Gaussian beam function the waist at the focal point can be extracted:

CCD-camera[9]**:** The total beam profile can be monitored with the provided software. A Gaussian beam function is fitted online to the beam in x- and y-direction and the two times $1/e^2$-radius can be directly read by the user. A disadvantage is, that the camera cannot be used at high power. This can be circumvented by deflecting the high power beam with a mirror and measuring the beam profile of the transmitted part.

Waist meter[10]**:** This model uses a scanning knife-edge technique. The beam waist size $1/e^2$ is calculated by measuring the rise-time of the integrated waveform as the knife-edge passes through the input beam. The power is monitored by a photodetector. The minimal beam waist that can be measured is provided to be $10\,\mu$m, with a resolution of $2\,\mu$m.

Knife edge: For this method one uses a calibrated micrometer-stage, where a razor blade is mounted to cut the beam. The power of the beam is monitored by a power meter. The total power of a beam can be calculated by integrating the intensity of the beam over the whole area. By cutting the beam, part of this area is blocked, leading to a lower value at the power meter. From calculations using the Error-function it can be derived, that the distance from the point where 86 % of the total power passes the knife edge to the point giving 14 % of the total power corresponds to the $1/e^2$ beam waist. This method can also be used at high power.

To determine the most reliable method, we use a test setup to measure a beam profile with the different applications. In Fig. 5.5 our results are summarized. The fitted waists for the CCD-camera and the knife edge method give similar results, while the waist meter measurement results in a smaller waist. Around the focal point the waist meter and the knife edge method give larger numbers by a factor of two in comparison to the fitted quantity. This indicates that

[9]Model BC106-VIS-CCD Camera Beam Profiler from Thorlabs. The pixel size of this camera is $6.45\,\mu$m, which allows waist measurements down to $30\,\mu$m.

[10]Model WM100 Omega Meter from Thorlabs.

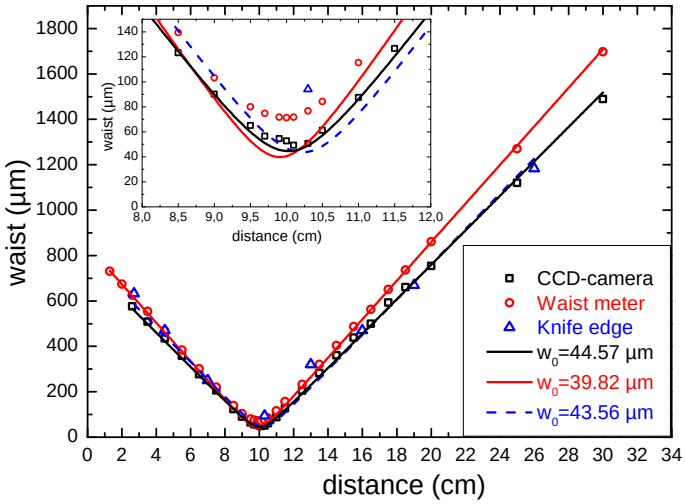

Figure 5.5: Comparison between different methods for measurements of the beam waist in a test setup. The beam profile is measured along its propagation direction and fitted by a Gaussian beam function. The inset shows a zoom of the measurement around the focal point.

these methods cannot give reliable results for small beam waists. The obtained quantities with the CCD-camera, however, match nicely to the fitted curve.

Horizontal dipole trap

To investigate the dependence of the beam waist w_x on the scanning voltage U_{gain} we use the CCD-camera method. In Fig. 5.6 the measurements of the horizontal and vertical waists are shown. The scanning voltage is varied from 1 to 5 V. One can clearly see the large effect on the beam waist. The waists for the scanned beam are fitted by a Gaussian function and not by the formula for a Gaussian beam, due to the fact that the scanning system does not actually enlarge the beam waist, but just shifts the beam very fast. The slope of the scanned beam waist in axial direction is, therefore, much to steep to be fitted with the theory of a Gaussian beam. It seems that the scanning has also an influence on the vertical beam axis. The slight enlargement of w_y is just a relict coming from the fact that the scanning axis has a slight angle to the x-axis; see Fig. 5.4(c). The small shift of the focal position of about 300 μm can also be related to this fact.

During the experimental cycle, U_{gain} is tuned to adjust the aspect ratio of the beam, to obtain the highest phase-space density of the atomic sample. Therefore, it is crucial to explore the performance of the scanning system. For

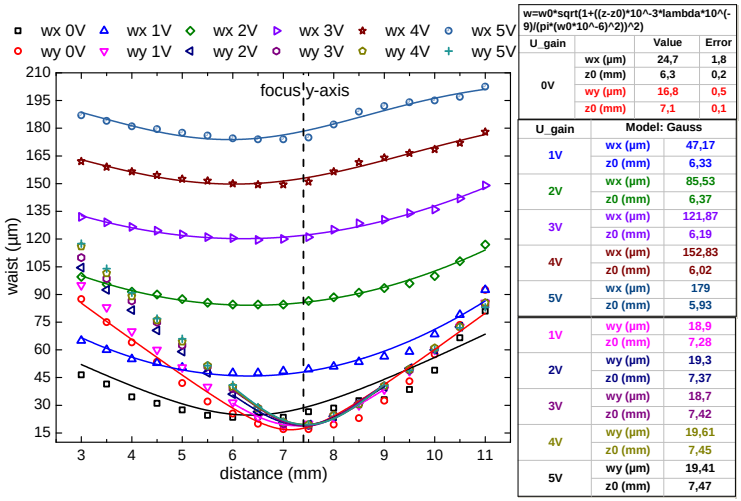

Figure 5.6: Measured beam size of the horizontal dipole trap beam in horizontal and vertical direction without and with scanning the beam. The scanning voltage U_{gain} is tuned from 0 to 5 V with a step size of 1 V. In axial direction the scanned beam does not show a Gaussian behavior anymore. The dashed line shows the position of the focal point of the vertical beam axis. Atoms are sitting most likely at this position. For this set of measurements the modulation frequency was fixed to $f_{mod} = 200\,\mathrm{kHz}$.

this set of measurements we monitor the waists at the focal point of the y-direction. Figure 5.7(a) shows the dependence of the waist in x- and y-direction on the voltage U_{gain}. Again the strong increase of w_x can be seen. At around 5 V the curve levels out. This is due to the lower diffraction efficiency of the AOM at the edge of its bandwidth, as discussed at Fig. 5.4.

In Fig. 5.7(b), the dependence of the scanned beam waist on the modulation frequency $f_{mod} = \omega_{mod}/2\pi$ is shown. The maximum modulation frequency strongly depends on the scanning voltage U_{gain}. The more the beam is scanned the earlier the beam size breaks down for higher modulation frequencies. For a scanning voltage of up to 2 V the maximum modulation frequency $\omega_{mod}^{max} \approx 2\pi \cdot 1\,\mathrm{MHz}$ can be used. In our experiment we choose the modulation frequency $\omega_{mod} = 2\pi \cdot 200\,\mathrm{kHz}$ as working point. At this frequency the beam shape at high scanning voltages is still Gaussian and the horizontal waist can be tuned up to 222 μm. This corresponds to an aspect ratio of 13 and matches the expectation of Sec. 5.1.1. The chosen frequency further fulfills the requirement $\omega_{mod} \gg \omega_x$ since we do not expect larger frequencies than $\omega_x = 2\pi \cdot 2$ kHz at our experimental cycle; see Sec. 6.1.

Summarizing, we find as minimal beam waists $w_x = 24\,\mu\mathrm{m}$ and $w_y = 17\,\mu\mathrm{m}$.

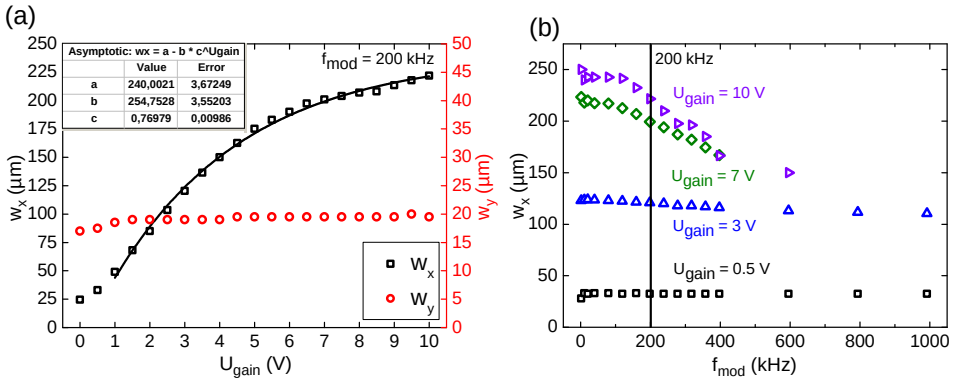

Figure 5.7: Dependence of the scanned beam waist on the voltage U_{gain} (a) and on the modulation frequency (b). The enlargement of w_y in (a) is only due to the slight angle of the scanning axis to the x-axis. In (b) the dependence on f_{mod} was measured for different aspect ratios. Higher scanning gains lead to a lower maximum modulation frequency. For this measurements the new voltage controlled oscillator VCO190-112T is used. In our experiment the modulation frequency $f_{mod} = 200\,\text{kHz}$ is chosen as working point.

By scanning the horizontal direction, w_x can be enlarged up to 222 μm, leading to an AR of 13. The maximum power at the chamber is 18 W. At the loading phase a large beam area and a high power are crucial to increase the loading efficiency. For the maximum scanning and the highest power we expect the following trap frequencies according to Eqs. (3.26) and (3.31):

$$\omega_x = 2\pi \cdot 106\,\text{Hz}, \quad \omega_{y_{gravity}} = 2\pi \cdot 1.34\,\text{kHz}, \quad \omega_z = 2\pi \cdot 14\,\text{Hz}.$$

In this configuration we want to load atoms from the MOT to the dipole trap.

Vertical dipole trap

The vertical dipole trap beam is produced by a 10 W broadband Yb fiber laser source at 1064 nm and has an initial power of about 8 W in the chamber. The beam profile is elliptic with waists $w_{2z} = 55\,\mu$m and $w_{2x} = 110\,\mu$m. Due to the limited access to the view ports of the chamber the vertical beam has an angle α of 15° to the y-axis. The angle to the propagation direction z of the horizontal beam amounts to $\alpha = 14°$. The definitions of these angles are shown in Fig. 3.3. The vertical trapping beam is crucial in the later phase of the evaporation process, to "close the door" such that atoms cannot escape along the propagation axis of the horizontal beam. The evaporation process will be discussed in detail in the next Chapter.

Chapter 6

Measurements with atoms

In the previous Chapter we described our novel dipole trap setup based on the scanning system. With this improvement we are now able to produce BECs with larger atom numbers, as compared to our previous setup [Aik12]. The parameters, which are crucial to reach this goal, are the spatial overlap of MOT and dipole trap as well as the evaporation efficiency. The optimal evaporation ramp for a high evaporation efficiency is part of the discussion in Sec. 6.2. Before we start our search on the best evaporation ramp, it is necessary to understand the geometry of the dipole trap. For this purpose we measure temperature and trap frequencies in a single beam configuration for various scanning voltages. Section 6.1 is dedicated to the investigation of the trapping geometry. From these measurements we also can extract the experimental value for the dynamic polarizability of erbium. We find $\mathrm{Re}(\alpha) = (84 \pm 2 \pm 18)$ a.u. for a dipole trap laser light operating at 1064 nm.

For a loading time of 5 s we prepare typically $2 \cdot 10^7$ atoms in the MOT at a temperature of about 10 μK. Thanks to the scanning system we can load up to $6 \cdot 10^6$ atoms to the optical dipole trap at about 20 μK for a loading time of 500 ms. This corresponds to a loading efficiency of 30 %, which is exceptionally high. For a 10 s loading time we gain $3.5 \cdot 10^7$ atoms in the MOT and can load up to $1.2 \cdot 10^7$ atoms to the dipole trap, corresponding to 34 %. The huge numbers in the dipole trap are a great improvement compared to the values obtained in our earlier experiments [Aik12], where the maximum number was limited to $3 \cdot 10^6$ atoms even for large numbers in the MOT. The results presented in this chapter are for a loading time of 10 s of the MOT. These are the starting conditions for the evaporative cooling process.

If not labeled differently the results shown in this Chapter have been measured with the further improved dipole trap setup; see Sec. 5.1.3. The values for the beam waist and the power for this setup are:

- The vertical beam waist w_y at the focal point is 16.1 μm.
- The horizontal beam waist w_x at the focal point can be tuned from 26.9 μm to 190 μm. This corresponds to a maximal possible AR of about 12.
- The maximum power at the chamber of the beam depends on the scanning voltage. Without scanning a power of 27 W can be reached. For a scanning voltage U_{gain} of 10 V we measure a maximum power of 17 W. This is due to the lower diffraction efficiency of the AOM at the edge of its bandwidth.

6.1 Characterization of trap geometries

A precise knowledge of the trap frequencies is crucial to determine the properties of the trapped sample, e.g. phase-space density and peak number density. The trap frequencies are related to the depth and dimension (beam width) of the trap, as indicated by Eq. (3.26). Different methods can be used to measure the trap frequencies. From comparison between the trap frequency, the dipole beam profile, and the laser intensity one can extract the dynamic polarizability of the trapped sample. The determination of this quantity is from particular importance for theorists, since it gives them the possibility to test their models for various parameters for the particular species. Before our studies, experimental data on the dynamic polarizability of erbium was not available. Additionally, we find a huge dependence of the lifetime of the atoms in the dipole trap depending on the laser polarization.

6.1.1 Trap frequency measurements

The measurements of the trap frequencies give insight into the confinement of the dipole trap laser beam. The basic principle of trap frequency measurements is as follows. A thermalized sample is prepared in a specific trap. The cloud is then excited by compressing, decompressing, or shifting the sample for a short period of time. When the cloud is released to the original trap it starts to oscillate. The trap is switched off after a variable holding time t_e and an absorption image is taken. Additional free expansion, which is named time-of-flight (TOF), increases the signal-to-noise ratio. Different methods are probed to obtain reliable trap frequency measurements:

Power modulation: The strength of the trapping potential is changed by either increasing the intensity or switching off the trap for a short period of time. Therefore, the atomic cloud is compressed or released and

switching on the original trap leads to excitations of the breathing mode. The typical modulation time for the switching-off method is one fourth of the trap frequency. The breathing mode is observed by monitoring the width of the atomic cloud for various holding times t_e in the final trap after modulation. For an ideal thermal gas the breathing mode is equal to twice of the trap frequency. In principle, with this method the frequencies of all axes could be observed. However, the oscillation on the strongest confining axis is the most dominant one. Therefore, the oscillations on the weaker confining axes are hardly visible. An example measurement for this method is shown in Fig. 6.1(b).

Magnetic gradient field: The gradient field can be used to tilt the dipole trap along the vertical y-axis. Additionally the gradient field has also an influence on the horizontal x- and z-axis[1]. This leads to a coupling of the individual oscillations, thus making the distinction between the individual trap frequencies less reliable.

Individual modulation of each axis: Most precise measurements can be done when the sample is only modulated along the monitored trap axis. In our case the strongest confining axis is the y-axis (axis of gravity). Therefore, the corresponding trap frequency can be obtained by switching off and on again the horizontal dipole trap beam, as discussed above. For the measurement of ν_x we use the scanning system itself. By slowly changing the voltage U_{offset} the atomic sample is shifted adiabatically along the x-axis and starts oscillating, when it is released to its original position. The center-of-mass motion around the equilibrium position is observed to extract the trap frequency. This measurement can be done even during w_x is enlarged by the scanning system. An example of this measurement is shown in Fig. 6.1(a). For the z-axis we can use the vertical beam, which provides a strong confinement in the axial axis of the horizontal beam to excite oscillations. The vertical beam is typically switched on for a few milliseconds.

In conclusion, best results are obtained by modulating each axis individually. An additional reason for this is that the axis of our imaging system has an angle of 28° to the z-axis in the x-z-plane; see Fig. 3.5. As a consequence, simultaneous oscillation along the x- and the z-axis cannot be distinguished if they have similar frequencies. Too strong excitations of the trapped cloud can lead to large atom loss and heating. An adequate modulation manifests itself in many observable oscillations of the trapped atomic cloud. A damping of these

[1]The vertical gradient is produced by two coils in Anti-Helmholtz configuration. Due to $\mathrm{div}\vec{B} = 0$ the creation of a vertical gradient also leads to horizontal gradients.

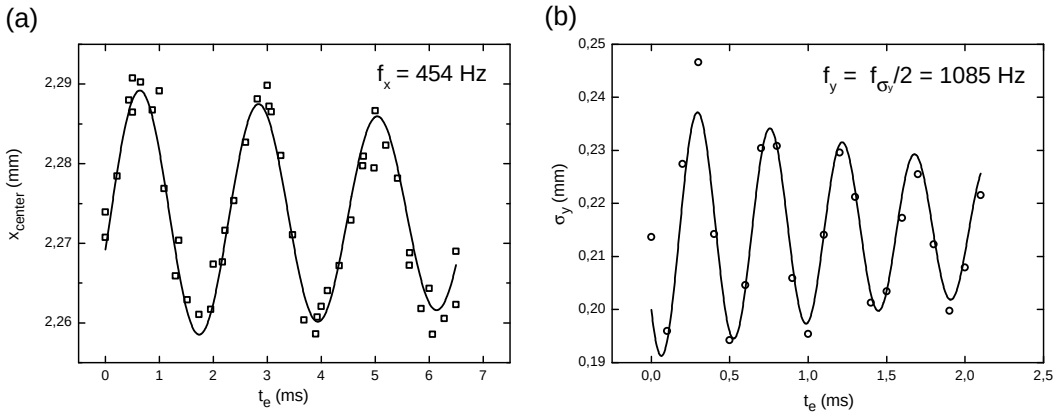

Figure 6.1: Typical trap frequency measurements in a single beam dipole trap configuration. In Figure (a) the sample was prepared at a laser power of 2 W, and an AR of 2. To excite the center-of-mass oscillation along the x-axis the trapped cloud was shifted by changing the value of U_{offset} for 60 μs. In Figure (b) a breathing mode oscillation is shown. Switching off the beam for 50 μs leads to an excitation of this mode, especially along the strong confining y-axis. For this measurement the sample was prepared at 2 W with the scanning system being off. We obtain trap frequencies $\omega_x = 2\pi \cdot 454$ Hz and $\omega_y = 2\pi \cdot 1085$ Hz, respectively.

oscillations indicates that the trapping potential is not perfectly harmonic.

6.1.2 Atomic polarizability

The knowledge of the atomic polarizability of erbium is of great importance for experiments and theories. For instance, theorists are able to extract the C_6 and ΔC_6 values of this element if a precise knowledge of the polarizability is available; see Sec. 2.3. The atomic polarizability $\mathrm{Re}(\alpha)$ can be obtained from trap frequency measurements. Here a single beam dipole trap is used. As discussed in Chap. 3, there is a very convenient relation between $\mathrm{Re}(\alpha)$ and the optical dipole trap frequencies ν:

$$\begin{aligned} \nu_x &= \frac{1}{2\pi}\sqrt{P \cdot \frac{8A \cdot \mathrm{Re}(\alpha)}{w_x^3 w_y m\pi}}, \\ \nu_y &= \frac{1}{2\pi}\sqrt{P \cdot \frac{8A \cdot \mathrm{Re}(\alpha)}{w_y^3 w_x m\pi}}, \end{aligned} \tag{6.1}$$

where P is the power of the dipole trap beam, w_x and w_y are the beam waists in the horizontal and the vertical axis, respectively, and $A = 1.65 \cdot 10^{-41}/(2\epsilon_0 c)$ is the conversion factor to extract the polarizability in atomic units. These formula can be derived from Eqs. (3.2), (3.18), and (3.26), where

$$\nu_x \equiv \frac{1}{2\pi}\sqrt{\frac{4\hat{U}}{mw_x^2}}, \quad \nu_y \equiv \frac{1}{2\pi}\sqrt{\frac{4\hat{U}}{mw_y^2}},$$

are the trap frequencies obtained from the harmonic approximation of the dipole trap potential and

$$\hat{U} = \tilde{U} I_0 = -\frac{1}{2\epsilon_0 c}\mathrm{Re}(\alpha)\frac{2P}{\pi w_x w_y},$$

is the total trap depth. In the experiment we measure independently the trap frequencies as well as the beam waists w_x and w_y. The latter are obtained by beam profile measurements with a CCD-camera, see Sec. 5.2, and have in general the highest uncertainty. For the measurements of the trap frequencies we use the methods discussed above.

In a single beam configuration the trap frequencies are measured at different dipole trap conditions. To change the trapping potential we either vary the trapping power or change the trap aspect ratio with the scanning system.

Power variation: For this measurement we prepare a cold and thermalized atomic sample. Therefore, the laser power is first decreased to 0.7 W, leading to temperatures of about 2 μK. Then the power is increased to the desired value, thus recompressing the sample. After one second of thermalization the atomic cloud is modulated for a few micro seconds to excite oscillations and to extract the trap frequencies ν_x and ν_y. The TOF time is typically 10 ms. Here the scanning voltage was fixed to 0 V. This measurement was done with our first dipole trap setup, discussed in Sec. 5.1.3, with beam waists $w_x = (24.0 \pm 1.8)\,\mu$m and $w_x = (17.0 \pm 0.5)\,\mu$m. Equation (6.1) is used as fit model to extract the atomic polarizabilities. In Fig. 6.2 we summarize our measurements of the trap frequencies as a function of the laser power. The solid lines are the fits to the set of data.

Aspect ratio variation: Similar to the above discussed procedure a cold and thermalized atomic sample is prepared by evaporating down to about 2 μK and recompressing the sample with a power of 2 W. During the recompression the trap aspect ratio is adjusted by changing U_{gain} to the desired value. We measure trap frequencies ν_x and ν_y for various scanning voltages U_{gain} of up to 3.5 V. Our current dipole trap setup was used to

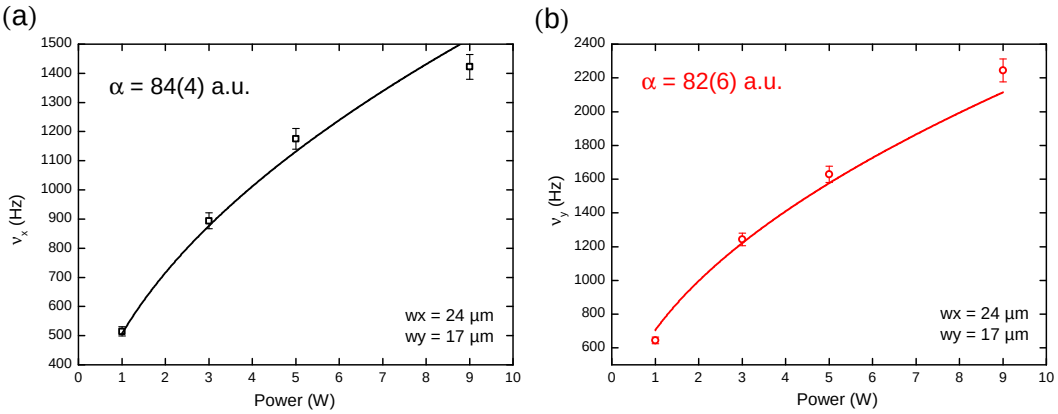

Figure 6.2: In a single beam configuration we have measured trap frequencies for different powers of the horizontal dipole trap beam in x- (a) and y-direction (b). The solid line is a fit to the data according to Eq. (6.1). The fit yields for the atomic polarizabilities $\mathrm{Re}(\alpha) = (84 \pm 4)$ a.u and $\mathrm{Re}(\alpha) = (82 \pm 6)$ a.u for the data of Fig. (a) and Fig. (b), respectively. The obtained errors are statistical only.

perform this set of measurements. The beam waists without scanning are found to be $w_x = (27.0 \pm 2.0)\,\mu$m and $w_y = (16.1 \pm 0.5)\,\mu$m. The dependence of the horizontal waist on U_{gain} in the region up to 3.5 V is found from offline measurements similar to Fig. 5.7:

$$w_x = [-345.8 + 372.7 \cdot \exp(0.078 \cdot U_{gain})]\,\mu\mathrm{m}. \tag{6.2}$$

This dependence is used to refine the fit model of Eq. (6.1). Figure 6.3 shows the fit to the measured trap frequencies as a function of U_{gain}.

In Fig. 6.4 we summarize the extracted atomic polarizabilities of each set of measurements. The data points are fitted with a constant to find the best value of $\mathrm{Re}(\alpha)$:

$$\mathrm{Re}(\alpha) = (84 \pm 2)\,\mathrm{a.u.} \tag{6.3}$$

As discussed above the error of this value is statistical only. In the fits the uncertainties of the trap frequencies and the powers are included[2]. Up to now the uncertainties of the beam waists have not been considered. In the following discussion we want to give an upper and a lower bound of the uncertainty of the measured atomic polarizabilities.

[2]In our experiment the trap frequency measurements typically have an uncertainty of 3 %. The uncertainty of the power is about 1 % and is related to the used photo-diode and to the whole control circuit.

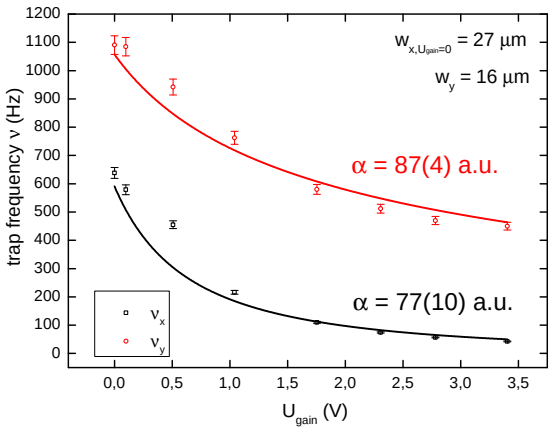

Figure 6.3: The trap frequencies were measured for different scanning voltages of the horizontal dipole trap beam in y- and x-direction. The power of the beam was set to 2 W. In the fitting function the dependence of the waist w_x on the voltage U_{gain} is included; see Eqs. (6.1) and (6.2). From the fit we can extract the atomic polarizabilities $\mathrm{Re}(\alpha) = (87 \pm 4)$ a.u and $\mathrm{Re}(\alpha) = (77 \pm 10)$ a.u for the set of measurements in the y- and x-direction, respectively.

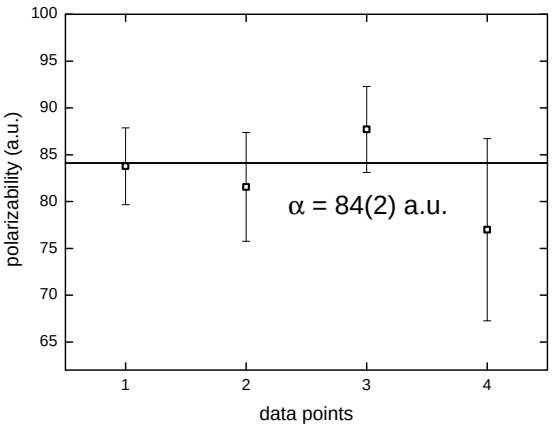

Figure 6.4: All obtained values are plotted in one graph to extract the best value and the statistical error of the polarizability. The solid line is a constant fit to the data that gives $\mathrm{Re}(\alpha) = (84 \pm 2)$ a.u.

Lower bound: To determine the lower bound value we use the theory of error propagation. Equation (6.1) is solved to $\mathrm{Re}(\alpha)$ and for each data point we calculate the corresponding error of the polarizability according to the above discussed uncertainties of ν, P, w_x and w_y. We then use all the errors to calculate the total error and find ± 3 a.u.

Upper bound: Trap frequencies and beam powers can be measured with a high precision, where for the beam waist measurements systematic errors hardly can be avoided. For the offline beam characterization the last part of the dipole trap setup is copied since it is not possible to measure the beam profile *in* the vacuum chamber; see Sec. 5.1.3. Imperfect alignment of the optical elements in the copied path can lead to a deviation between the measured and the actual beam waists. To obtain the beam waists we take multiple data points along the propagation direction of the laser beam and fit the set of data with the theory of a Gaussian beam. Since the beam profile of the used laser is not perfectly Gaussian, additional deviations are expected. To take the systematical error into account we assume the beam waists to be wrong by $\pm 2\,\mu$m. This assumption is used to calculate the polarizability again by varying the beam waists in the fit functions of Figs. 6.2 and 6.3. The observed differences to each above discussed polarizability are then used to determine the overall systematic error. The error propagation yields ± 18 a.u.

In conclusion we find for the dynamic polarizability of erbium at 1064-nm:

$$\mathrm{Re}(\alpha) = (84^{\pm 18}_{\pm 3} \pm 2)\,\text{a.u.} \tag{6.4}$$

including lower and upper bound of the systematical errors as well as the statistical error.

This quantity is in striking contrast to the theoretical predicted polarizability of 159 a.u. ; see Sec. 4.1. This seems to be typically for lanthanides, since the dynamic polarizability of dysprosium has also been overestimated in comparison to the measured quantity [Dzu11, Lu11].

To cross-check the obtained quantity for the dynamic polarizability we use the mathematical model to calculate the expected trap depth; see Appendix B. The depth is compared to the corresponding, measured temperature of the atomic sample. We find well agreement to the typical correlation $k_B T \approx 1/10 \cdot U_{dip}$.

In future we plan to add lithium to our experiment. For this element the dynamic polarizabilities are known [Tan10]. This knowledge can be used to extract the polarizability of erbium. A proposal by Cronin et al. [Cro09] shows that the ratios of polarizabilities of different species can be determined accurately.

6.1.3 Comparison to offline characterization

From the results shown in Fig. 6.3 we can also extract the trap aspect ratio AR of the scanned beam for different scanning voltages U_{gain}. In Fig. 6.5 we plot the

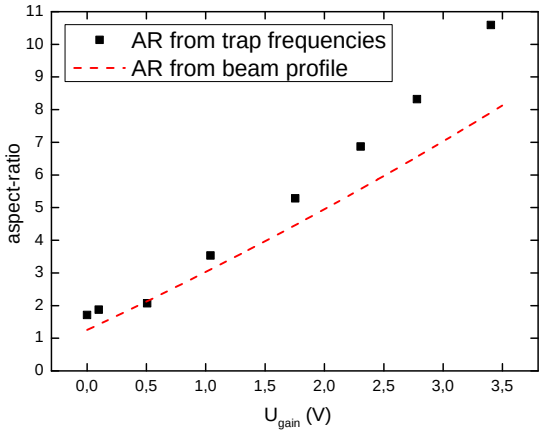

Figure 6.5: Comparison between the aspect ratio of the horizontal dipole trap obtained from trap frequency measurements to the expected AR from the offline beam characterization.

measured AR and the AR expected from our offline characterization. For small values of U_{gain} the measured and the expected AR nicely agree. At a higher scanning voltage the two values disagree by up to 30 %. An explanation for this can be an introduced anharmonicity in the x-axis lowering the trap frequencies ν_x, thus increasing the AR. Suspects are the slight angle of the scanning axis to the x-axis, and a non perfectly Gaussian shape of the time-averaged beam. Systematic errors in the measurement of the beam profile could also contribute to the observed differences. One problem is, that the measurement of the beam profile can only be done at a "copied chamber", and thus could differ from the actual profile. However, for the experimental process we are only interested in the actual trap geometry, determined by trap frequency measurements. From the trap frequency measurements we find a maximal possible AR of 15, which gives us a huge flexibility for the modification of the trapping potential.

6.1.4 Polarization dependence of the trapping geometry

In a recent paper on the polarizability of polar molecules, it was shown that the polarizability strongly depends on the angle of the linear polarization of the dipole trap laser beam [Ney12]. Tuning the polarization thus changes the trap geometry. This is related to the tensorial part, which accounts for the dependence of the polarizability on the angle between the electric field and the quantization axis. The observation also could be valid for dipolar non-S state atoms, such as erbium. As a preliminary investigation we measured

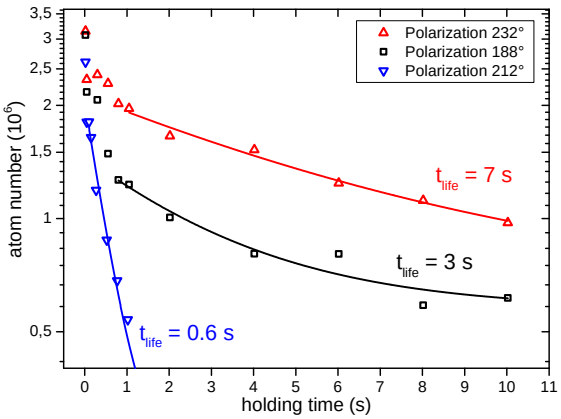

Figure 6.6: We load atoms to the dipole trap and simply let them evolve in the same trap. Thereby we monitor the atom number right at the end of the holding time. The linear polarization of the trapping laser light is adjusted manually, rotating a λ-half wave-plate, where 232° and 188° correspond to p- and s-polarization, respectively. For s-polarization the field of the laser light is aligned along the quantization axis of the atoms. We find a strong dependence of the lifetime on the laser polarization, indicating loss processes for a specific polarization angle. The lifetimes are extracted by fitting the data with an exponential decay function.

the trap geometries for different angles of laser polarization, but could not observe a measurable difference in trap frequencies and temperature. This matches our theoretical calculations, where we found that the tensorial part of the polarizability for the ground state of erbium does not play a significant role; see Sec. 4.1. However, we found a dramatic change in the stability of the trapped atoms. For this measurement we prepare $3.5 \cdot 10^6$ atoms in a single beam configuration with a power of 18 W and an AR of 10 after a loading time of 5 s of the MOT. For a specific angle of the laser polarization we observe huge and very fast losses of atoms. In Fig. 6.6 we report the number of atoms for a variable holding time directly after loading to the optical dipole trap. The log-lin scale reveals the non-exponential behavior of the loss dynamics. At shorter holding time we generally see faster losses compared to the one observed at longer time. This losses can be related to plain evaporation. For longer holding times a change of 20° in the angle of the linear polarization gives a change of one order of magnitude in t_{life}. The investigation of the reason for these losses will be part of future experiments.

6.2 A new Bose-Einstein condensate

In our recent papers, see Ref. [Fri12] and Appendix C, we demonstrated a simple and efficient approach to trap erbium atoms and cool them to quantum degeneracy. During this thesis, we could further improve our system and reach even higher atom numbers in the Bose-Einstein condensate. In this Section, we will discuss the optimized evaporation process used with the new trap. For a high evaporation efficiency the ratio between elastic and inelastic collisions in the trap is crucial. This ratio is determined by the density, which can be changed by modifying the trap geometry. In our previous setup simply the power of the horizontal and vertical dipole trap were changed to reach a good evaporation efficiency. The scanning system gives us an additional, optional "knob" to optimize the collisional rate. Especially at the end of the evaporation process high densities can lead to large three-body losses. With the scanning system we have a versatile tool to reduce the losses. To control the scanning system U_{gain} is calibrated to the trap AR. Therefore, we fit the data of Fig. 6.5 and implement the obtained function in the experiment control system. The AR can then be controlled for every evaporation step via this system.

The evaporation efficiency is determined by the ratio of the change in phase-space-density (D) to the change in atom number in a double-logarithmic scale:

$$\epsilon = -\frac{\frac{dD}{D}}{\frac{dN}{N}}, \tag{6.5}$$

where the phase-space-density D is defined as

$$D = \left(\frac{\hbar}{k_B}\right)^3 \omega_x \omega_y \omega_z \frac{N}{T^3}. \tag{6.6}$$

This equation outlines that high atom numbers and low temperatures are crucial for a high phase-space-density. When the phase-space-density is equal to about 1.2 quantum degeneracy is reached. An additional parameter to describe the atomic sample is the peak-number density. It gives the maximum number of particles per area and can be derived from the density distribution in a harmonic trap:

$$n_0 = N \left(\frac{m}{2\pi k_B T}\right)^{\frac{3}{2}} \omega_x \omega_y \omega_z. \tag{6.7}$$

The new BEC

We load $1.2 \cdot 10^7$ atoms to the optical dipole trap with a power of 20 W and a scanning AR of 10. The thermalized temperature of the atoms directly after

loading is about 20 μK. These are the starting conditions for the evaporation process. Figure 6.8 shows the whole evaporation ramp for the creation of the new BEC. At every evaporation step we adjust the power of the horizontal and the vertical dipole trap beam, as well as the AR. We monitor the atom numbers, the temperatures, and the trap geometries by frequency measurements for a selection of evaporation steps. These data are fed to our mathematical model to determine the trap depths, the phase-space-densities and the peak-number densities. For these calculations we use the measured atomic polarizability of erbium. The calculation of the trap depths already includes the contribution of both the horizontal and the vertical dipole trap beam. For the beam waists of the horizontal beam we use $w_y = 16.1\,\mu$m and $w_x = (AR \cdot w_y)\,\mu$m where for the vertical beam $w_x = 112\,\mu$m and $w_z = 70\,\mu$m are the expected beam waists[3]. The dashed lines in Fig. 6.8 show the expected trap frequencies for each power and AR of the crossed dipole trap according to our mathematical model, discussed in Sec. 3.3. In most cases we find well agreement with the actual measured trap frequencies. The maximal discrepancy between the measured and the calculated trap frequencies is about 20 %. One explanation for this is the difficulty to measure the beam waists precisely, as well as the systematic errors discussed in Sec. 6.1.2. Another effect that could justify this discrepancy is the movement of the atomic sample when the vertical dipole trap beam is switched on. We see a shift of about 200 μm of the center of the cloud in the axial direction of the horizontal dipole trap beam. This is related to the non perfect crossing of the beams. The atoms are shifted out of the focal point of the horizontal beam, which results in a change of the confinement. Thus, different trap frequencies than expected can occur.

After about 5 s of evaporation an onset of a BEC is achieved, which corresponds to a phase-space-density of 1.2. A very interesting feature of the applied evaporation process can be seen in the plot of the peak-number density. When the vertical trapping beam is turned on a huge increase of n_0 is observed, where it is then slowly decreased to reach a high evaporation efficiency. Just at the very last evaporation step we gain a pure BEC.

The whole evaporation process takes 6.9 s and leads to a final number in the pure BEC of up to $2 \cdot 10^5$ atoms. In comparison to our previous setup this number is larger by a *factor of 3*; see Appendix C. At the end of the evaporation process the increase of the AR by the scanning system is ideal to decrease the density, and thus three-body losses. Best performance is found for

[3]The used beam waists of the vertical dipole trap beam differ from the measured waists in the focal point. For the alignment of the crossing of the two dipole trap beams only the atom number in the crossed region is monitored. Therefore, it is very likely, that the focal points of the beams are not perfectly overlapped.

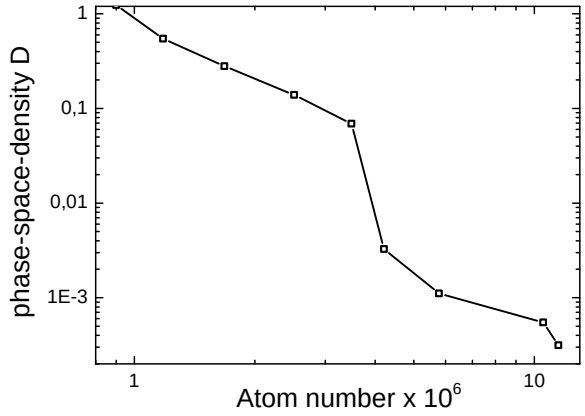

Figure 6.7: Double-logarithmic plot of the phase-space-density during the evaporation ramp as a function of the atom number. The overall evaporation efficiency ϵ until quantum degeneracy is reached is 3.4. When the vertical beam is switched on a huge evaporation efficiency is observed.

an AR of 7 at the end of the evaporation process. Due to the large AR at the loading phase we start with low trap frequencies, then compress the sample and finally evaporate it down. In the pure BEC we find peak-number densities of up to $8 \cdot 10^{13}\,\mathrm{cm}^{-3}$.

Figure 6.7 shows the phase-space-density as a function of the atom number during the evaporation process. The overall evaporation efficiency until $D = 1.2$ is reached is $\epsilon = 3.4$, which is very high. When the vertical dipole trap beam is switched on we find an evaporation efficiency of 16. In the latter phase of the evaporation process the efficiency decreases to $\epsilon = 2$.

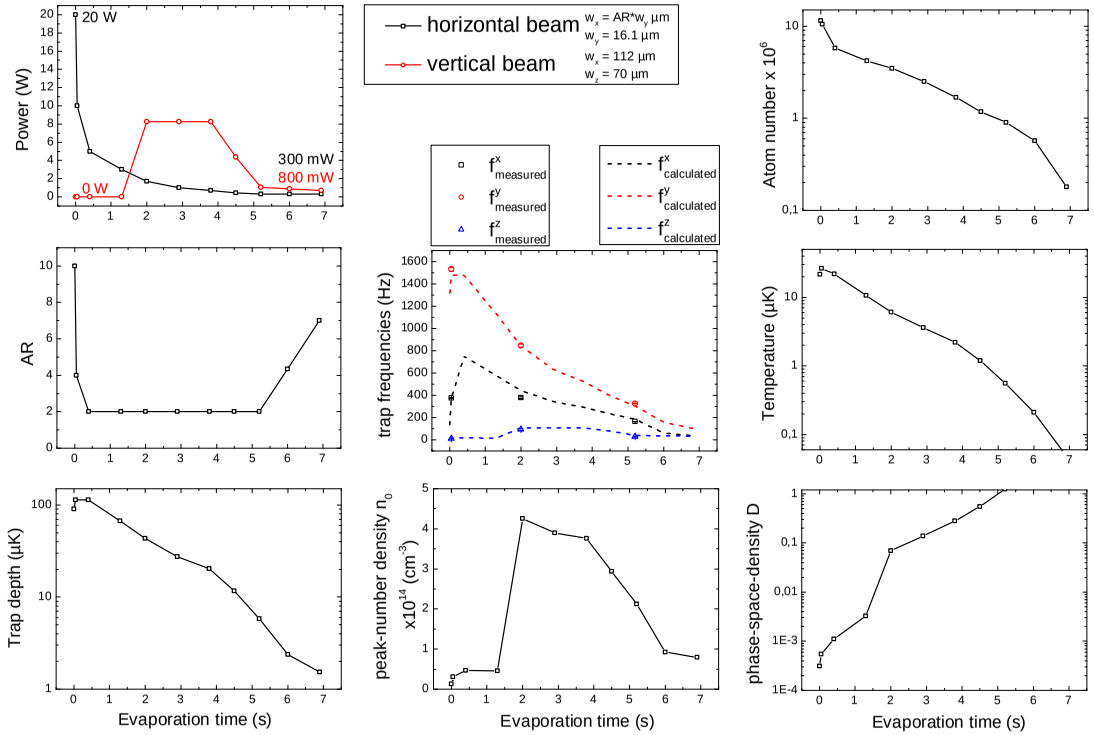

Figure 6.8: This figure shows the evolution of different parameters during the forced evaporation. The whole evaporation process takes about 7 seconds. For each evaporation step we measure the atom number, the temperature, as well as selected trap frequencies. From these quantities we can calculate the phase space density and the peak number density at each step. Our theoretical model is used to calculate the potential depths of the crossed dipole trap and the expected trap frequencies. The latter are indicated by the dashed lines. We find well agreement with the measured data with a maximum deviation of 20 %. We obtain up to $2 \cdot 10^5$ atoms in the pure BEC which is an improve in number of a factor of 3 compared to our previous dipole trap setup.

Chapter 7

Conclusion and Outlook

The goal of my master thesis was to implement an optical dipole trap with tunable geometry to our erbium experiment. Optical dipole traps are used to load atoms from the MOT and evaporatively cool them down to quantum degeneracy. A flexible geometry can help to optimize the loading of the optical dipole trap and the evaporative cooling efficiencies. This improvement can be used to reach large atom numbers in the trap.

The potential created by a laser beam depends on the intensity and profile of the laser. The depth of the created dipole trap is related to the atomic polarizability of the trapped atomic species. The polarizability depends on the atomic spectrum of the particular species, as well as on the wavelength of the laser beam. Erbium is a multi-valence electron system and shows thus a complex and rather unknown energy spectrum. Theoretical and experimental efforts are taken to further improve the knowledge of the energy level structure. During my thesis work I developed a mathematical model to calculate the atomic polarizability of erbium. For the calculation every known dipole allowed transition is taken into account according to its line strength factor. For the ground state of erbium atoms we find a dynamic polarizability of 159 a.u. for a dipole trap operated at 1064-nm. This value accounts for both the scalar and the tensorial part of the atomic polarizability. Furthermore, the mathematical model allows to fully simulate the trapping geometry of the crossed dipole trap used in our experiment.

In a first crossed dipole trap setup we managed to evaporatively cool down erbium atoms to quantum degeneracy – *for the first time*. The corresponding publication is given in Appendix C. This knowledge was used to design the optical setup for the horizontal dipole trap laser beam with tunable ellipticity. To dynamically tune the trapping geometry we use a scanning system consisting of an AOM. An AOM deflects a laser beam depending on the frequency of

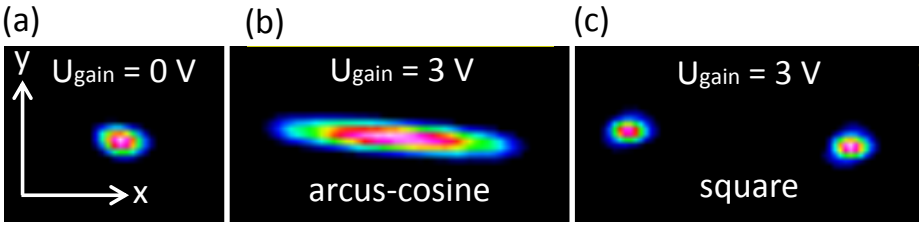

Figure 7.1: Scanning system gallery for a scanning voltage of 0 V (a) and 3 V; (b) and (c). The shape of the beam depends on the function used to scan the beam. Here we show two examples. An arcus-cosine function leads to an elliptic Gaussian beam shape (b), whereas a square function creates two beams (c). The pictures were taken with the CCD-camera beam profiler.

sound waves in the crystal. A change of this frequency thus changes the angle of deflection and a scan over a range of frequencies leads to a time-averaged beam profile. A lens positioned one focal length after the AOM translates the deflection into a horizontal displacement of the beam. If the frequency of the AOM is scanned fast enough compared to the trap frequency of the dipole trap a time-averaged potential is created. The ellipticity of this time-averaged potential can be tuned by the scanning system. The optical setup of the horizontal beam was optimized several times and we finally find ideal working conditions with beam waists at the position of the atoms of $w_x = 27\,\mu$m and $w_y = 16\,\mu$m along the horizontal and vertical axis, respectively. The horizontal waist can be tuned up to $190\,\mu$m, leading to a theoretical maximal possible aspect ratio of 12. The vertical dipole trap beam has a waist of $55\,\mu$m along the axial direction of the horizontal beam and a waist of $110\,\mu$m perpendicular to this direction in the horizontal plane. In Fig. 7.1 the profile of the horizontal dipole trap beam for a selection of scanning functions is shown.

With the new flexible dipole trap we can load up to 35 % of the atoms from the MOT to the optical dipole trap at a temperature of about $20\,\mu$K. For a loading time of 10 s of the MOT this number typically corresponds to $1.2 \cdot 10^7$ atoms. For the optimized evaporation process we reach up to $2 \cdot 10^5$ atoms in the pure BEC. The evaporation efficiency of this process is 3.5, which is very high. In comparison to our first setup we could *triple* the atom number in the BEC. Especially at the end of the evaporation process the scanning system is used to weaken the confinement in the trap thus suppressing three-body losses. In Fig. 7.2 a 3D density profiles of absorption images for different evaporation steps are shown. For lower, and lower temperatures the matter waves of the atoms start to overlap finally forming a Bose-Einstein condensate, a macroscopic occupation of the lowest quantum state.

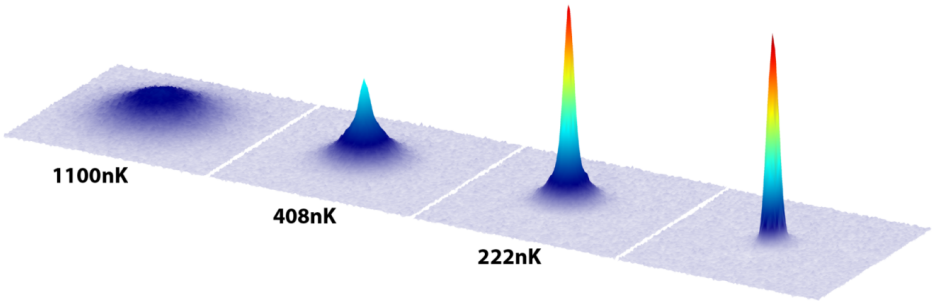

Figure 7.2: 3D density profile showing the phase-transition of the erbium atomic cloud to a Bose-Einstein condensate.

Additionally the scanning system can be used for trap frequency measurements. Here the atomic sample is first adiabatically shifted in x-direction. Then a sudden switch back to the original trap leads to center-of-mass oscillations. From trap frequency measurements we find that we can reach *even higher aspect-ratios* than expected from the offline beam configuration. This behavior could be due to anisotropical effects, and further increases the tunability of the dipole trap. The maximal possible aspect-ratio is measured to be 15.

First results based on my work are measurements of the atomic polarizability of erbium. Here we compare trap frequency measurements with our mathematical model to extract the dynamic polarizability. In atomic units we find a value of $\mathrm{Re}(\alpha) = (84^{\pm 18}_{\pm 3} \pm 2)$ a.u. where ± 3 and ± 18 indicate the lower and the upper bound of the systematical error of the measured polarizability and ± 2 is the statistical error. This value is smaller by 47 % compared to the one calculated by our mathematical model. A similar discrepancy also has been observed for dysprosium [Lu11], which is part of the lanthanide series as well. The obtained value will help to theorists to further improve their theoretical models for erbium, including investigations of the isotropic and anisotropic part of the van der Waals interaction as well as theoretical researches on Feshbach resonances.

In future experiments we plan to use the scanning system to investigate the geometry dependence of anisotropic quantum effects in dipolar gases. The influence of the geometry on the behavior of a dipolar gas was already demonstrated by the group of T. Pfau [Koc08]. We are confident that with our tunable dipole trap we can precisely map the behavior of the system when the geometry is changed in a continuous way. Due to the high magnetism of erbium quantum fluctuation are expected to be sizable and to manifest themselves in the TOF dynamics of a Bose gas as well as in the collective modes [Lim11]. Since

quantum fluctuations are expected to depend on the aspect-ratio of the trap, our new flexible dipole trap setup will be an ideal environment for this investigation. Other proposals show that in a dipolar BEC confined in a quasi-2D trap a rotonlike spectrum can emerge [San03, Bla12]. This fascinating phenomena is unique to dipolar BECs and may also can be accessed by means of the scanning system.

Appendix A

Electronics

Figure A.1 shows the electronic circuit for the creation of the frequency signal, which is sent to the AOM-driver. The modulation signal U_{mod} consists of the three signals U_{offset}, U_{gain} and U_{signal} and is generated by a mixer:

$$U_{mod} = U_{offset} + \frac{U_{signal}\, U_{gain}}{10\,\mathrm{V}} \tag{A.1}$$

The supply voltage is $\pm 18\,\mathrm{V}$. The maximum values for U_{offset} and U_{gain} are $+10\,\mathrm{V}$, and for U_{signal} the voltage should not exceed $\pm 10\,\mathrm{V}$. The full control on the signal U_{mod} is then used to change the radio-frequency signal created by a VCO in the AOM-driver. The signal is then amplified and sent to an AOM.

In Fig. A.2 the electronic circuit of the used AOM-driver is shown. As discussed in Sec. 5.1.4 some electronic parts had to be exchanged to achieve an utilizable radio frequency signal.

In Fig. A.3 the box of the AOM-driver is shown. The electronic circuit to produce U_{mod} is implemented in this box on the left hand side. The right hand side was changed, as discussed at Fig. A.2.

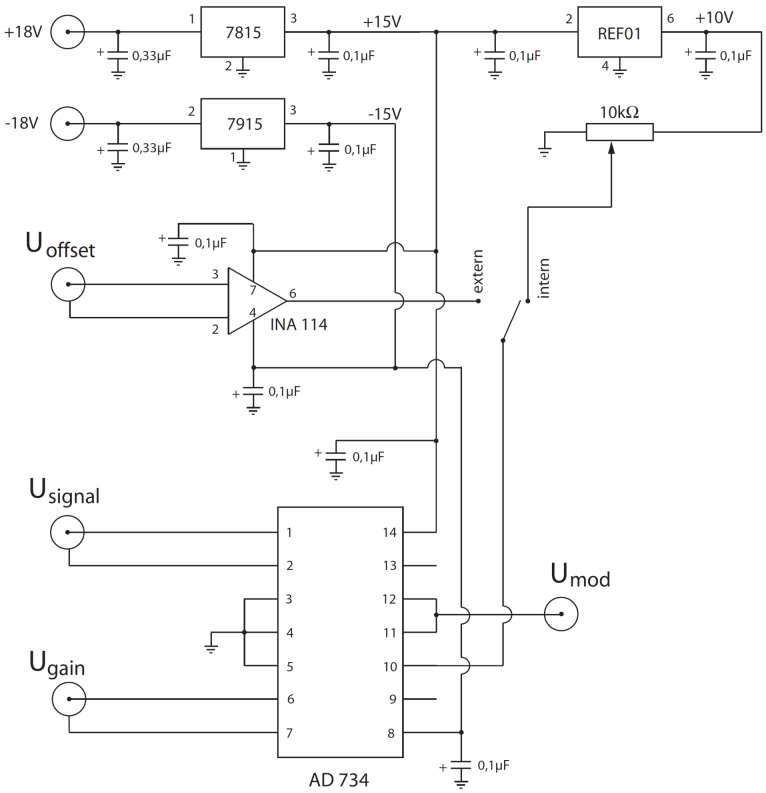

Figure A.1: Electronic circuit used to generate the signal to scan the frequency of the AOM; see Sec. 5.1. The mixer AD 734 from Analog Devices creates the output signal U_{mod} from the input signals U_{offset}, U_{signal} and U_{gain}.

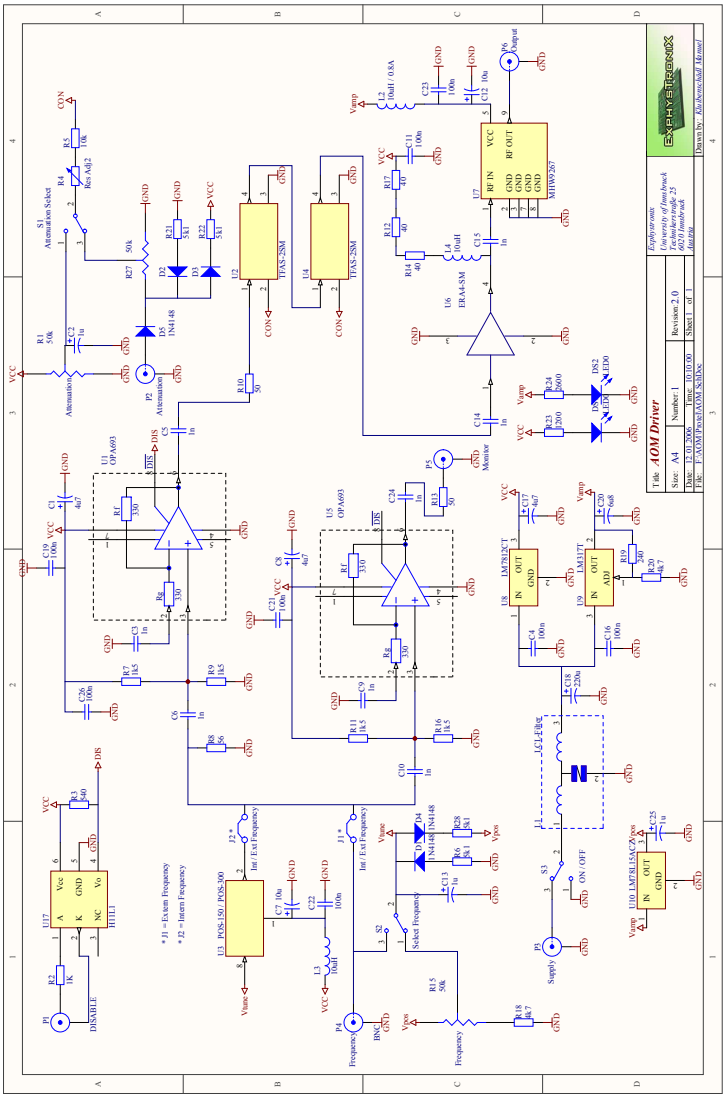

Figure A.2: Electronic circuit of the analog AOM-driver. U_{mod} is sent to input P4 and controls V_{tune}. Instead of the model POS-150 we use the model VCO190-112T from Varil. The TTL-switch OPA693, the preamplifier ERA4-SM and the amplifier MHW9267 are bridged and replaced coaxially by components from Mini-Circuits (ZASWA-2-50DR, 1 ZFL-500LN+, ZHL-1-2W). C13 had to be removed, because of influences on the signal at high frequencies.

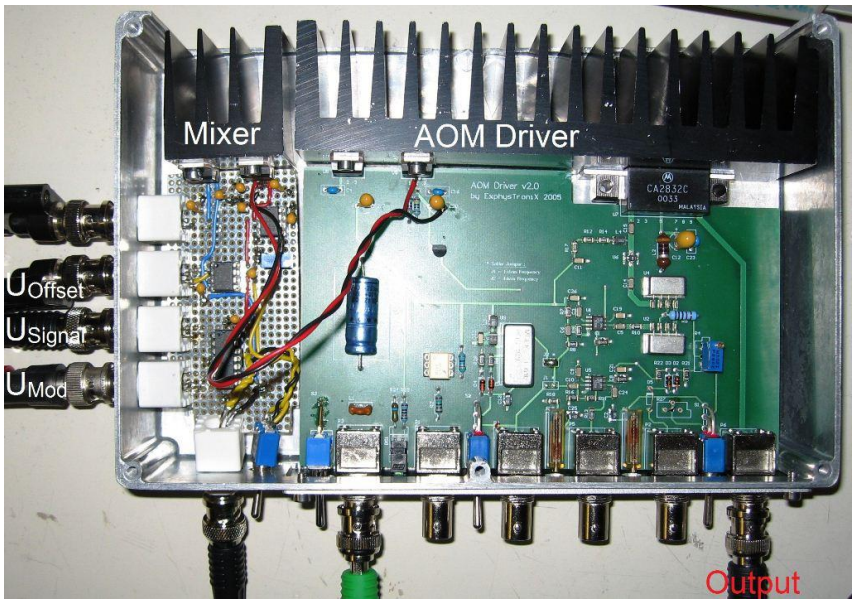

Figure A.3: Realized electronic box for the control of the AOM.

Appendix B

Dipole trap model

On the following pages the source code of the MATHEMATICA file to model the trapping potential of our dipole trap for the ground state of bosonic erbium atoms is shown. The definitions of the various formulas can be found in Cha. 3.3.

The file is subdivided into five main parts:

Constants and data import: In this part the constants used in the file are defined. Also the data of all dipole allowed transitions contributing to the dipole trap are imported, hence the wavenumber of the allowed transitions from the ground to the excited states, as well as the total angular momentum quantum number J and the linewidth of the excited states [Wya12]. Furthermore, each linewidth is adapted according to the line strength factors related to the $3J$-symbol. The total dipole potential and the scattering rate are calculated from Eq. (3.13) and Eq. (3.14) (Here the intensity $I(\vec{r})$ is set to 1).

Dipoletrap formula: In this section the functions to calculate the total intensity profile for crossed elliptic beams under an angle are defined. With this intensity the real total dipole potential and the scattering rate – for each beam – can be calculated.

Parameter: In this part all known parameters as beam waists, powers, atom number and temperature are added.

Output: Before the trapping parameters are calculated, the trapping geometry has to be recalculated each time the input parameter are changed. Therefore we calculate the trap depth of the horizontal and the vertical dipole trap, the effective beam waists and Rayleigh ranges due to the angles α and β between the beams, the trap frequencies, the scattering and heating rates, the phase space density and the peak number density, the influence of the gravity on the vertical confinement as well as the

magnetic field gradient to levitate the trap against gravity.

Figures: The calculated data are used to plot the change of the dipole trap potential because of the gravity, as well as the 3D trapping profile along each axis.

This model also can be used in any other ultracold experiment. Here is a list of the values, which have to be changed to adapt this model to any other element and trapping geometry:

- the wavelength λ of the used dipole trap laser – here given as $\lambda 1064$.
- the trapping potential U_{dip} for an intensity I of one – here given as $U1064$.
- the scattering rate Γ_{sc} for an intensity I of one – here given as $\Gamma 1064$.
- In this file the two values $U1064$ and $\Gamma 1064$ are calculated from implemented data, which includes the contribution of all the dipole allowed transitions from the ground to the excited states for bosonic erbium atoms according to their line strength factors [Wya12]. $U1064$ is nothing else than the atomic polarizability and already includes the scalar and the tensorial part.
- the horizontal and the vertical waist of each laser beam – here given as $waist1y$, $waist1x$ for the horizontal beam and $waist2z$, $waist2x$ for the vertical beam.
- the power of each laser beam – here given as $power1$ and $power2$.
- the angles between the two laser beams α and β; the definition of these values can be found in Cha. 3.3.
- As an additional feature the model also calculates the phase-space-density (psd) and the peak number density ($npeak$). To get the right results, one also needs to change the values for the atom number ($Natom$) and the temperature ($Tatom$) in the trap.

```
Clear["Global`*"]
c = 299 792 458 (*m/s*);                    g = 9.804864698 (*m/s^2*);
hbar = 1.054571726*10^-34 (*Js*);           h = hbar*(2 Pi) (*Js*);
kB = 1.3806488*10^-23 (*J/K*);              μB = 9.27400968*10^-24 (*J/T*);
ermass = 166*1.660538921*10^-27 (*kg*);     ϵ0 = 8.854187817*10^-12 (*As/Vm*);
λ1064 = 1064*10^-9 (*m*);                   ω1064 = 2 Pi*c/λ1064 (*s^-1*);
```

Import data

```
(*Import data from .dat file,
including all allowed transitions from the ground to excited states*)
(*wzgr imports all the wavenumbers from the transition of the ground to the excited states*)
(*Jex imports all the total angular momentum quantum numbers of the excited states*)
(*ggr1 imports all the linewidths of the excited states times the statistical weight
 of these levels (15)*)
    AppendTo[$Path, NotebookDirectory[]];
    file = Import["Er_groundtransition.dat", "Table"];
    ground = file[[19 ;; 1194]];
    wzgr = ground[[All, 7]];
    Jex = Round[ground[[All, 3]]];
    ggr1 = ground[[All, 10]];
(*Calculate linewidth Γ and substitute by known measured Γ values for the 401 nm and 583 nm line;
The multiplication with the WignerJ accounts for the line strength factor of each transition*)
(*Calculate the optical transition frequencies*)
    ggr = ggr1/15;
    WignerJ = Table[(2 J + 1)*ThreeJSymbol[{6, -6}, {1, 0}, {J, 6}]^2, {J, Jex}];
    Γgr = ReplacePart[ggr, {{36} → 1.8686*10^8, {8} → 1.17*10^6}]*WignerJ;
    ωgr = 2*Pi*c/(10^-2/(wzgr*10^3)) (*s^-1*);
(*Dipoletrap formula*)
(*Calculates the potential depth of a dipole trap depending on the transitionfrequency
 ωa and the linewidth Gamma Of the excited state (with incoming light λ=1064nm)*)
    U[Gamma_, ωa_] := -3*Pi*c^2*Gamma/(2*ωa^3)*(1/(ωa - ω1064) + 1/(ωa + ω1064))
    Gammascat[Gamma_, ωa_] := 3*Pi*c^2*1/(2*hbar*ωa^3)*(ω1064/ωa)^3*(Gamma/(ωa - ω1064) + Gamma/(ωa + ω1064))^2
(*Potentialdepth (atomic polarizability) and scattering rate of the dipole trap;
just intensity has to be added*)
(*Consider all known transitions from groundstate to other states*)
    U1064  = Sum[U[Γgr, ωgr][[i]], {i, Length[ωgr]}] (*J m^2/W*)
    Reα = -U1064*2*ϵ0*c/(0.16487776*10^-40) a.u
    Γsc1064 = Sum[(Gammascat[Γgr, ωgr])[[i]], {i, Length[ωgr]}] (*s^-1 m^2/W*)
```

-4.93837×10^{-37}

159.009 a.u

4.98914×10^{-12}

Dipole trap formula

```
(*Gaussian beam waist*)
w[w0_, z_] := w0 Sqrt[1 + (z / zR[w0])^2]
(*Rayleigh length*)
zR[w0_] = Pi * w0^2 / λ1064;
(*Rayleigh length elliptic beam*)
zRell[wx_, wy_] = (zR[wx] zR[wy]) / (Sqrt[(1/2) * (zR[wx]^2 + zR[wy]^2)]);
(*Calculates waist and Railey length of an elliptic beam having an angle alpha to
     the coordinate system in the y-z plane
      η parameter used for =1: determining only the new beamwaist; =
 2: for including into trap frequency
   (contribution of axial confinment is half of radial confinement)*)
wα_angle[wz_, wx_, α_, η_] := (Cos[α * Pi / 180]^2 / w[wz, 0]^2 + Sin[α * Pi / 180]^2 / (η * zRell[wz, wx]^2))^(-1/2);
zRell_angle[wz_, wx_, α_, η_] := (Sin[α * Pi / 180]^2 / w[wz, 0]^2 + Cos[α * Pi / 180]^2 / (η * zRell[wz, wx]^2))^(-1/2);
(*calculates waist change of an elliptic beam having an angle beta to the coordinate
  system in the x-z plane*)
w2zβ_angle[wz_, wx_, β_, α_, η_] := (Cos[β * Pi / 180]^2 / wα_angle[wz, wx, α, η]^2 + Sin[β * Pi / 180]^2 / w[wx, 0]^2)^(-1/2)
w2xβ_angle[wz_, wx_, β_, α_, η_] := (Sin[β * Pi / 180]^2 / wα_angle[wz, wx, α, η]^2 + Cos[β * Pi / 180]^2 / w[wx, 0]^2)^(-1/2)
(*Intensity of the light beam depending on waists w0x and w0y,Power P,
radial compontents x(horizontal) and y(vertical) and axial distance z*)
intensity[P_, w0x_, w0y_, x_, y_, z_] :=
 (2 * P) / (Pi * w[w0x, z] * w[w0y, z]) * Exp[-2 * (x^2 / w[w0x, z]^2 + y^2 / w[w0y, z]^2)]
(*Horizontal beam: Potential depth in J and μK
                   Scattering rate*)
Upotgr1[x_, y_, z_] := U1064 * intensity[power1, waist1x, waist1y, x, y, z];
Tpotgr1[x_, y_, z_] := Upotgr1[x, y, z] 1/kB 10^6
rscat1[x_, y_, z_] := rsc1064 * intensity[power1, waist1x, waist1y, x, y, z];
(*Vertical beam: Potential depth in J and μK
                  Scattering rate*)
Upotgr2[x_, y_, z_] := U1064 * intensity[power2, waist2x, waist2z, x, z, y];
Tpotgr2[x_, y_, z_] := Upotgr2[x, y, z] 1/kB 10^6
rscat2[x_, y_, z_] := rsc1064 * intensity[power2, waist2x, waist2z, x, y, z];
(*Euler rotation on the x and z angle*)
xangle[x_, z_] := x * Cos[beta * Pi / 180] + z * Sin[beta * Pi / 180];

yangle[x_, y_, z_] := x * Sin[alpha * Pi / 180] Sin[beta * Pi / 180] + y * Cos[alpha * Pi / 180] -
```

```
    z * Sin[alpha * Pi / 180] Cos[beta * Pi / 180];

zangle[x_, y_, z_] := -x * Cos[alpha * Pi / 180] Sin[beta * Pi / 180] + y * Sin[alpha * Pi / 180] +
    z * Cos[alpha * Pi / 180] Cos[beta * Pi / 180];
(*Spatial potential of vertical beam due to angles α and β*)

Upotgr2angle[x_, y_, z_] :=
  U1064 * intensity[power2, waist2x, waist2z, xangle[x, z], zangle[x, y, z], yangle[x, y, z]];

    Tpotgr2angle[x_, y_, z_] := Upotgr2angle[x, y, z] 1/kB 10^6;
```

Parameter

y .. direction of gravity (axial direction of vertical beam)
x .. horizontal, perpendicular to horizontal beam
z .. axial direction of horizontal beam

```
(*Horizontal beam*)
    waist1y = 16.1 * 10^-6;        waist1x = 27 * 10^-6;        power1 = 1;
(*Vertical beam*)
    waist2z = 55 * 10^-6;        waist2x = 110 * 10^-6;        power2 = 10;
(*Angles between vertical and horizontal beam; α..rotation in y-z-plane;
β..rotation in x-z-plane;
Corresponds in our experiment to the angle of the vertical beam to the axis
 of gravity*)
    alpha = 15(*°*);
(*Corresponds in our experiment to the angle of the horizontal beam in the
 horizontal plane(half angle between viewports = 14°)*)
    beta = 14(*°*);
(*Measured data*)
    Natom = 2.5 * 10^6;
    Tatom = 3.6 * 10^-6;
```

OUTPUT

```
(*Effective potential depth of the dipole trap in μK depending on the radial and
 axial parameters of the horizontal beam*)
    U1gr = -Upotgr1[0, 0, 0];
    T1gr = -Tpotgr1[0, 0, 0];
(*Effective potential depth of the dipole trap in μK depending on the radial and
 axial parameters of the vertical beam*)
    U2gr = -Upotgr2[0, 0, 0];
    T2gr = -Tpotgr2[0, 0, 0];
(*Waist/Rayleigh length change of vertical beam due to angle between beams*)
    w2znew = N[w2zβangle[waist2z, waist2x, beta, alpha, 2]];
    w2xnew = N[w2xβangle[waist2z, waist2x, beta, alpha, 2]];
    zRell2new = N[zRellangle[waist2z, waist2x, alpha, 2]];
(*Gravity deforms potential in vertical direction;
horizontal and vertical beam calculated independently
 (z-y-: particles with higher "altitude" have higher potential energy and could
```

```
(*therefore escape from the DT; with a magnetic field gradient B_lev this can be compensated*)
U_grav[y_] = ermass * g * y;
B_lev = U_grav[1] / (7 * μB) * 10^2 (* G/cm *);

T1_gravity[y_] = (U_grav[y * 10^-6] + Upotgr1[0, y * 10^-6, 0]) 10^6 / kB (*μK*);

Min1 = FindMinimum[{T1_gravity[y], -waist1y * 10^6 ≤ y ≤ waist1y * 10^6}, {y, 0}] (*μK*);
Max1 = FindMaximum[{T1_gravity[y], -10 * waist1y * 10^6 ≤ y ≤ (y /. Last[Min1])}, {y, 0}] (*μK*);
T1_real = -(First[Min1] - First[Max1]) (*μK*);
T1_real,y = If[power1 <= 0, 0, If[T1_real < 0, 0, T1_real]] (*μK*);
U1_real,y = T1_real,y * kB / 10^6 (*J*);

T2_gravity[y_] = (U_grav[y * 10^-6] + Upotgr2angle[0, y * 10^-6, 0]) 10^6 / kB (*μK*);

Min2 = FindMinimum[{T2_gravity[y], -zRell2_new * 10^6 ≤ y ≤ zRell2_new * 10^6}, {y, 0}] (*μK*);
Max2 = FindMaximum[{T2_gravity[y], -10 * zRell2_new * 10^6 ≤ y ≤ (y /. Last[Min2])}, {y, 0}] (*μK*);
T2_real = -(First[Min2] - First[Max2]) (*μK*);
T2_real,y = If[power2 <= 0, 0, If[T2_real < 0, 0, T2_real]] (*μK*);
U2_real,y = T2_real,y * kB / 10^6 (*J*);
(*Trapfrequencies due to angle α and β between the horizontal and the vertical beam;
same coefficient for z_R and waist contribution because η parameter(see above) takes
 care of this*)
ωx = √(4/ermass (U1gr/waist1x^2 + U2gr/w2x_new^2)); νx = ωx/(2*Pi);
ωy = √(4/ermass (U1gr/waist1y^2 + U2gr/zRell2_new^2)); νy = ωy/(2*Pi);
ωz = √(1/ermass ((2 U1gr)/zRell[waist1x, waist1y]^2 + 4*U2gr/w2z_new^2)); νz = ωz/(2*Pi);
(*Trapfrequencies due to angle α and β between the horizontal and the vertical beam
 including also gravity in y direction(lowering of potential depth)*)
ωy_gravity = √(4/ermass (U1real,y/waist1y^2 + U2real,y/zRell2_new^2)); νy_gravity = ωy_gravity/(2*Pi);
(*Heating rate in three dimension T_heat=1/3*T_rec*Γsc_mean; T_rec=2*E_rec/kB=101nK;
E_rec=(hbar*k_laser)^2/2m*)
(*Phase-space-density and peak number density according to temperature,
atomnumber and trap frequencies*)
Theat = 1/3 * (h/λ1064)^2 * 1/(ermass * kB) * (Γscat1[0, 0, 0] + Γscat2[0, 0, 0]);

psd = (hbar/(kB * Tatom))^3 * Natom * ωx * ωy * ωz;

npeak = Natom * (ermass/(2 * Pi * kB * Tatom))^(3/2) * ωx * ωy * ωz (*m^-3*);
```

```
StyleForm[
 NumberForm[
  TableForm[
   {{"Er DT Groundstate", "beams@angle", unit, "with gravity"}, {},
    {"U0,beam horizontal", T1gr, μK, T1real,y}, {"U0,beam vertical", T2gr, μK, T2real,y},
    {"νx,axis horizontal ", νx, s^-1}, {"νy,axis vertical ", νy, s^-1, νygravity},
    {"νz,axis axial", νz, s^-1}, {phspden, psd, 1}, {n0, npeak*10^-6, cm^-3},
    {"Total scattering rate", Γscat1[0, 0, 0] + Γscat2[0, 0, 0], 1/s},
    {Heating rate, Theat*10^9, nK/s}, {zRhorizontal, N[zRell[waist1x, waist1y]]*1000, mm},
    {zRvertical, N[zRell[waist2x, waist2z]]*1000, mm},
    {"mag. field gradient to levitate", Blev, G/cm}},
   TableSpacing→{1, 1}],
  5],
 Background→LightBlue, FontFamily→"Times", FontWeight→"Bold", FontSize→16]
```

Er DT Groundstate	beams@angle	unit	with gravity
$U_{0,\text{beam horizontal}}$	52.383	μK	47.101
$U_{0,\text{beam vertical}}$	37.638	μK	0.81345
$\nu_{x,\text{axis horizontal}}$	618.85	$\frac{1}{s}$	
$\nu_{y,\text{axis vertical}}$	1014.8	$\frac{1}{s}$	960.33
$\nu_{z,\text{axis axial}}$	237.73	$\frac{1}{s}$	
phspden	0.8843	1	
n0	2.4278×10^{15}	$\frac{1}{cm^3}$	
Total scattering rate	0.012556	$\frac{1}{s}$	
Heating rate	0.42652	$\frac{nK}{s}$	
$zR_{\text{horizontal}}$	1.0198	mm	
zR_{vertical}	12.254	mm	
mag. field gradient to levitate	4.1633	$\frac{G}{cm}$	

Figures

```
(*Deformation of the horizontal beam potential (y-direction) due to gravity*)
"Gravity on horizontal beam \     Gravity on vertical beam"
GraphicsRow[{
  Plot[T1gravity[y], {y, -2*waist1y*10^6, 2*waist1y*10^6}, PlotRange → Full,
   AxesLabel → {"vertical position y[μm]", "total potential[μK]"}],
  (*Deformation of the vertical beam potential (y-direction) due to
   gravity: angles α and β are included*)
  Plot[T2gravity[y], {y, -2*zRell2new*10^6, 2*zRell2new*10^6}, PlotRange → Full,
   AxesLabel → {"vertical position y[μm]", "total potential[μK]"}]
 }]
"Vertical(y) potential / Horizontal(x) Potential / Axial(z) Potential "
GraphicsRow[{
Plot3D[Tpotgr1[x*10^-6, 0, z*10^-6] + Tpotgr2angle[x*10^-6, 0, z*10^-6], {z, -100, 100},
   {x, -100, 100}, PlotRange → Full, AxesLabel → {"z (μm)", "x (μm)", "Udip (μK)"},
   Mesh → None, MaxRecursion → 0, PlotPoints → {15, 15}],
  Plot3D[Tpotgr1[0, y*10^-6, z*10^-6] + Tpotgr2angle[0, y*10^-6, z*10^-6], {z, -100, 100},
   {y, -100, 100}, PlotRange → Full, AxesLabel → {"z (μm)", "y (μm)", "Udip (μK)"},
   Mesh → None, MaxRecursion → 0, PlotPoints → {15, 15}],
  Plot3D[Tpotgr1[x*10^-6, y*10^-6, 0] + Tpotgr2angle[x*10^-6, y*10^-6, 0], {x, -100, 100},
   {y, -100, 100}, PlotRange → Full, AxesLabel → {"x (μm)", "y (μm)", "Udip (μK)"},
   Mesh → None, MaxRecursion → 0, PlotPoints → {15, 15}]
 }]
```

Gravity on horizontal beam

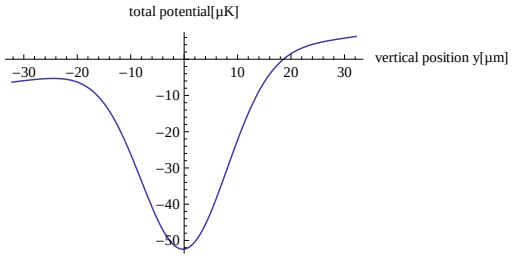

Gravity on vertical beam

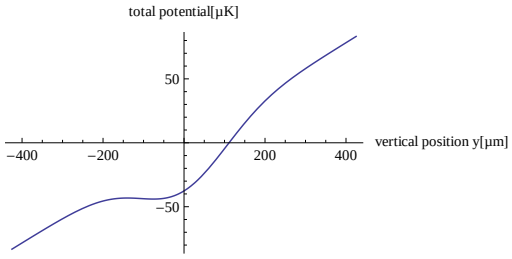

Vertical(y) potential / Horizontal(x) Potential / Axial(z) Potential

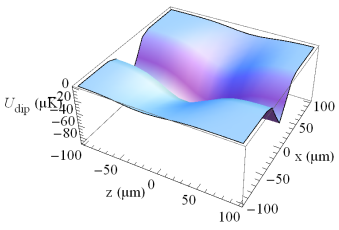

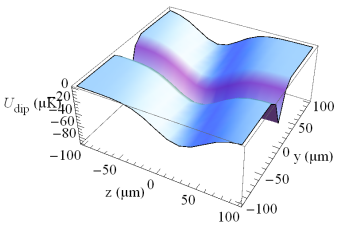

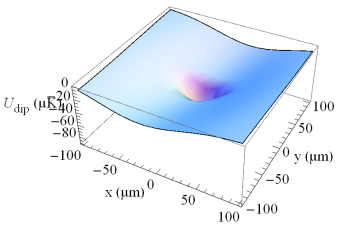

Appendix C

PRL: Bose-Einstein Condensation of Erbium

Bose-Einstein Condensation of Erbium

K. Aikawa,[1] A. Frisch,[1] M. Mark,[1] S. Baier,[1] A. Rietzler,[1] R. Grimm,[1,2] and F. Ferlaino[1]

[1]*Institut für Experimentalphysik and Zentrum für Quantenphysik, Universität Innsbruck, Technikerstraße 25, 6020 Innsbruck, Austria*
[2]*Institut für Quantenoptik und Quanteninformation, Österreichische Akademie der Wissenschaften, 6020 Innsbruck, Austria*

(Received 6 April 2012; published 21 May 2012)

We report on the achievement of Bose-Einstein condensation of erbium atoms and on the observation of magnetic Feshbach resonances at low magnetic fields. By means of evaporative cooling in an optical dipole trap, we produce pure condensates of ^{168}Er, containing up to 7×10^4 atoms. Feshbach spectroscopy reveals an extraordinary rich loss spectrum with six loss resonances already in a narrow magnetic-field range up to 3 G. Finally, we demonstrate the application of a low-field Feshbach resonance to produce a tunable dipolar Bose-Einstein condensate and we observe its characteristic *d*-wave collapse.

DOI: 10.1103/PhysRevLett.108.210401 PACS numbers: 03.75.Nt, 37.10.De, 51.60.+a, 67.85.Hj

Ultracold quantum gases have proven to be ideal systems for observing spectacular many- and few-body quantum effects. The large majority of these phenomena rely on the high degree of control over the interparticle interaction achieved with ultracold atoms. In the widely used alkalis, ultracold atoms interact isotropically via a short-range contact potential. A novel exciting frontier in quantum gas experiments is to access unexplored physical scenarios based on the anisotropic and long-range dipole-dipole interaction (DDI) [1,2]. A dipolar quantum gas is expected to exhibit fascinating phenomena, including novel many-body quantum phases [3–6]. The DDI acts in systems having sizable electric or magnetic dipole moments [1].

In the context of ultracold atomic quantum gases, pioneering experimental work on strong DDI has been carried out with chromium atoms [7–9]. Magnetic lanthanides offer new possibilities for dipolar physics. In such systems, the combination of a large magnetic moment and a large atomic mass leads to a particularly strong dipolar character. The demonstration of the first magneto-optical trap of erbium atoms [10] stimulated growing interest in such species for quantum gas experiments. Very recently, a Bose-Einstein condensate (BEC) and a degenerate Fermi gas of dysprosium have been produced [11,12]. We choose erbium as a promising candidate for experiments on dipolar quantum gases. This species has a number of very appealing features, including a large magnetic moment μ of 7 times the Bohr magneton, several stable isotopes, a rich energy level scheme [13] with a non-*S* electronic ground state [14], and interesting cold collisional phenomena [15,16].

In strongly magnetic atoms, the competition between the DDI and the contact interaction is very important and gives rise to many intriguing phenomena. The contact interaction is determined by the *s*-wave scattering length a and can be often tuned with external magnetic fields via Feshbach resonances [17]. Tuning of a also controls the balance of these two interactions. In the case of a novel species in quantum gas experiments, Feshbach resonances and scattering lengths are *a priori* unknown. Magnetic lanthanides such as erbium with their large magnetic moments and their non-*S* electronic ground states present a completely unexplored terrain in ultracold scattering physics. Here the anisotropic interaction is expected to give rise to novel scattering scenarios, which are not accessible with alkali atoms [18,19].

In this Letter, we report on the attainment of Bose-Einstein condensation of erbium atoms and on the observation of Feshbach resonances in the region of low magnetic fields. We obtain pure optically trapped BECs of ^{168}Er containing 7×10^4 atoms. The remarkably high efficiency of evaporative cooling in a standard optical dipole trap indicates favorable scattering properties of the ^{168}Er isotope. In addition, the magnetic Feshbach spectroscopy provides first valuable information on the scattering behavior of submerged-shell atoms at ultralow temperatures. Moreover, we demonstrate low-field Feshbach tuning of the contact interaction in our strongly dipolar BEC.

Our experimental procedure to create a BEC of Er follows a simple and straightforward scheme, inspired by work on Yb atoms [20,21]. Our starting point is the narrow-line *yellow* magneto-optical trap (MOT) described in our very recent work [22]; it operates on the 583 nm line (natural linewidth 190 kHz). We choose this approach because narrow-line MOTs permit us to obtain samples with a large number of atoms at temperatures in the lower microkelvin region. This allows a direct and efficient transfer of atoms into optical dipole traps without the need for additional cooling stages [20,21]. Our MOT gives about 10^8 atoms at a temperature of 15 μK [23].

An additional very advantageous feature of our approach is that the MOT light automatically pumps the atoms into the lowest Zeeman sublevel $m_J = -6$, where m_J is the projection quantum number of the total electronic angular momentum $J = 6$. This effect results from the interplay between gravity and weak radiation pressure, which leads to a spatial down shift with respect to the zero of the

magnetic quadrupole field [24] and thus to a preferential absorption of the vertical MOT beam with σ^- polarization [22]. The polarization of the sample is confirmed by Stern-Gerlach-type measurements.

Our optical dipole trap geometry follows the concepts originally applied in experiments with Yb BEC [20]. The trap is created by crossing a tightly confining horizontal beam (y axis) and a less focused vertical beam (z axis). The basic idea is that initially the atoms are predominantly trapped by the horizontal beam, whereas the vertical beam provides confinement relevant in the final stage of evaporation. The horizontal beam is derived from a 100 W broadband Yb fiber laser operating at 1075 nm and has an initial power of 10 W. The beam has an elliptic cross section with a waist of 30(40) μm along the vertical (horizontal) direction. The vertical beam is produced by a 10 W Yb fiber laser source at 1064 nm and has an initial power of 8 W. The beam profile is elliptic with a waist of 55(110) μm along (perpendicular to) the axis of the horizontal beam.

We load the dipole trap during the MOT compression phase. We observe that the time period in which the compressed MOT and dipole trap coexist is crucial for efficient loading. The number of atoms in the optical dipole trap exponentially approaches its maximum value with a time constant of about 150 ms. After 600 ms of loading, we turn off the MOT beams and the quadrupole magnetic field, and we switch on a weak homogeneous magnetic field of about 300 mG along the vertical direction to preserve the spin polarization of the sample. We obtain 2.6×10^6 atoms at a temperature of 42 μK in the optical dipole trap. At this point, the atoms are mainly trapped by the horizontal beam. We measure oscillation frequencies $(\nu_x, \nu_y, \nu_z) = (1.3, 0.016, 1.95)$ kHz; the potential depth is estimated to be 560 μK. The peak density and the peak phase-space density are 1.7×10^{13} cm^{-3} and 1.6×10^{-4}, respectively. These are our starting conditions for the evaporative cooling process.

Forced evaporative cooling is performed by reducing the power of the trapping beams in a nearly exponential ramp. The overall evaporation sequence has a duration of 5.5 s [25]. We then turn off the trapping beams and let the atomic cloud expand before applying standard absorption imaging. For imaging, we illuminate the atomic cloud with a 50-μs probe beam pulse [26]. The probe beam propagates horizontally at an angle of 14° with respect to the propagation axis (y axis) of the horizontal trapping beam.

The phase transition from a thermal cloud to BEC manifests itself in a textbooklike bimodal distribution in the time-of-flight absorption images. Figure 1 shows the absorption images and the corresponding linear density profiles for different final temperatures, i.e., for different stages of the evaporation. At higher temperatures the atomic distribution is thermal with the expected Gaussian profile resulting from the Maxwell-Boltzmann distribution; see Fig. 1(a).

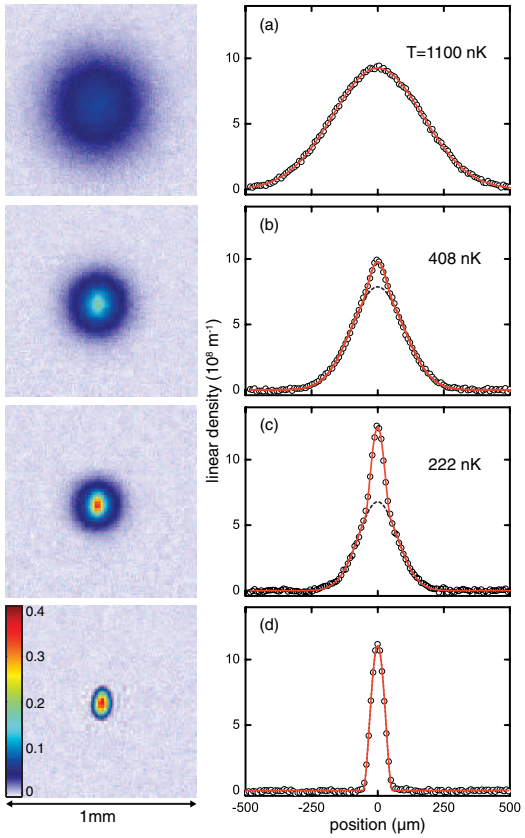

FIG. 1 (color online). Absorption images and integrated density profiles showing the BEC phase transition for different evaporation times. The absorption images are an average of four images taken after 24 ms of expansion. The color bar shows the optical density. The solid lines are fits to the data using Gaussian (a), bimodal (b) and (c), and Thomas-Fermi (d) distribution. The dotted lines represent the Gaussian part of the bimodal fit, describing the thermal atoms. From the fit we extract: $N = 3.9 \times 10^5$, $T = 1100$ nK (a), $N = 2.1 \times 10^5$, $T = 408$ nK (b), $N = 1.6 \times 10^5$, $T = 222$ nK (c), $N = 6.8 \times 10^4$ (d), where N is the total atom number. For (b) and (c), we extract a condensate fraction of 5% and 20%, respectively.

By cooling the atomic sample below the critical temperature, we clearly observe that the atomic density distribution has a bimodal profile with a narrower and denser peak at the center, which represents the BEC (b). By further evaporating the sample, the BEC fraction continuously increases (c) until the thermal component is not anymore discernible and an essentially pure BEC is formed with 7×10^4 atoms (d).

To analyze our data, we fit a bimodal distribution to the integrated time-of-flight absorption images. This distribution consists of a Gaussian function, which accounts for the thermal atoms, and an inverted integrated parabolic function for the BEC component in the Thomas-Fermi limit.

Just after the onset of quantum degeneracy (BEC fraction ~5%), we measure trap frequencies of $(\nu_x, \nu_y, \nu_z) = (208, 70, 299)$ Hz, atom number of $N = 2.1 \times 10^5$, and a temperature of $T = 408$ nK. The critical temperature of 417 nK as calculated from standard BEC theory (without interaction shift) is consistent with this observation.

The evaporation efficiency is found to be remarkably high as 3.5 orders of magnitude in phase-space density are gained by losing a factor of 10 in atom number. This observation already points to favorable scattering parameters of the ^{168}Er isotope. First evaporative cooling experiments on the most abundant ^{168}Er isotope reveal a lower efficiency in the final stage of evaporation, suggesting that a different strategy might be needed to reach BEC.

To gain insight into the ultracold collisional properties of erbium we perform Feshbach spectroscopy [17] at low magnetic fields. This measurement is done in a way that allows us to identify both the poles and zero crossings of Feshbach resonances [27,28]. The basic idea here is to prepare the system at a variable target value of the magnetic field and then to rapidly (50 ms) decrease the depth of the optical dipole trap by almost a factor of 2. The sample stays near thermal equilibrium with an effective temperature of 2.2 μK but features a truncated energy distribution. We then let the system evolve at a constant trap depth for 250 ms, during which plain evaporative cooling and inelastic losses can occur depending on the scattering length. We finally switch off the trap and take time-of-flight images to determine the temperature and number of the atoms. The measurement is then repeated for variable magnetic-field values. Such a Feshbach scan shows resonance poles as loss features and zero crossings as temperature maxima.

Figure 2 shows the loss spectrum and the corresponding temperatures in the low magnetic-field range up to 3.2 G [29]. Already in this narrow magnetic-field range, the loss spectrum is very rich. We identify six pronounced resonant minima in the atom number that we interpret as being caused by Feshbach resonances. For convenience, we determine the resonance positions with Gaussian fits, yielding 0.72, 0.91, 1.51, 2.16, 2.48, and 2.85 G. The loss features show different strengths and widths. For the three broader resonances at 0.91, 2.16, and 2.48 G, we also observe the appearance of temperature maxima to the right of the loss minima (arrows in Fig. 2). These temperature maxima mark the zero crossings of the scattering length. The other loss features are too narrow to provide clear signatures of the zero crossing. From the difference in positions between the minima in the atom number and the maxima in temperature we estimate the widths Δ of the resonances. We find $\Delta = 65$, 60, and 180 mG for the resonances at 0.91, 2.16, and 2.48 G, respectively.

In a strongly dipolar atomic gas, universal dipolar scattering is present [30–32], so that the total cross section for elastic scattering does not vanish at the zero crossings of the scattering length. For Er, a minimum cross section $\sigma_{\mathrm{dip}} = 8\pi(30a_0)^2$ results from universal dipolar scattering, where a_0 is the Bohr radius. The fact that we observe temperature maxima near the zero crossings suggests a dominant role of s-wave scattering and not of dipolar scattering. Preliminary cross-dimensional thermalization measurements indeed point to a scattering length between 150 and $200a_0$.

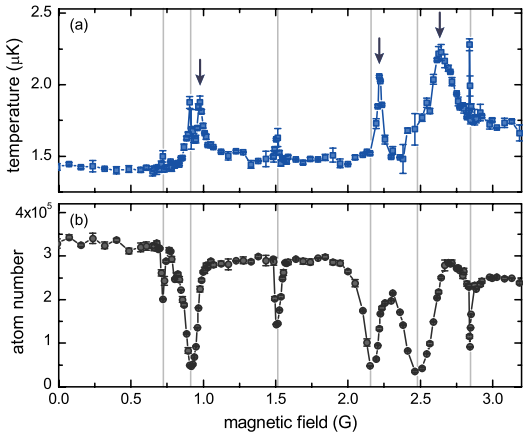

FIG. 2 (color online). Observation of Feshbach resonances in Er-Er collisions. The measured temperature (a) and atom number (b) are plotted as a function of the magnetic field. The minima in the atom number indicate the Feshbach resonance poles, marked by the thin vertical lines. The maxima in the temperatures to the right of the three stronger loss features (arrows) are attributed to the respective zero crossings of the scattering length. The varying background in the atom number is presumably due to ramping effects caused by the sweep of the magnetic field across the resonances.

The existence of Feshbach resonances at low magnetic fields makes the manipulation of the contact interaction in the Er BEC very convenient and straightforward. As a proof-of-principle experiment, we explore the controlled d-wave collapse of the BEC, following the procedure successfully applied by the Stuttgart group [7]. We first produce a pure BEC by evaporative cooling at 1.2 G, which is above the position of the first broad Feshbach resonance (0.91 G). Here we obtain 3×10^4 atoms in the BEC, indicating that forced evaporation at this magnetic field is slightly less efficient. We then ramp down the magnetic field within 2 ms to a variable target value and let the sample evolve for 2 ms before switching off the trap. The magnetic field is kept constant at its target value during the first stage of the expansion (15 ms), where the main dynamics happens. We then set the magnetic field along the y axis and we image the atomic cloud after an additional 11 ms of expansion. Our results are summarized in Fig. 3, where we show time-of-flight absorption images for different values of the target magnetic field. We observe a dramatic change in the shape of the condensate when the

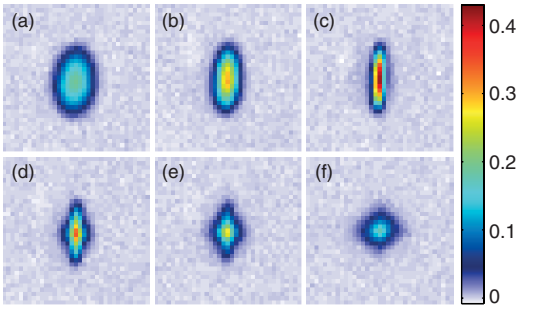

FIG. 3 (color online). Absorption images showing the d-wave collapse of the BEC. The field of view is 290 μm $\times$ 290 μm. The images are an average of eight pictures. The color bar shows the optical density. The images are taken for different target values of the magnetic field: 1.208 G (a), 0.963 G (b), 0.947 (c), 0.942 G (d), 0.939 G (e), and 0.934 (f). We note that the actual magnetic-field value might be slightly higher (10 mG) because of ramping issues and eddy currents [7].

magnetic field is reduced towards the zero crossing of the scattering length. At the magnetic field of evaporation, the aspect-ratio of the cloud is close to the one observed at zero magnetic field; see Fig. 3(a). By changing the magnetic field to lower target values, the BEC shows a more and more anisotropic shape (b) and (c). Below a critical magnetic-field value, the BEC develops a complicated *cloverleaf* pattern (d)–(f) which is the striking signature of the d-wave collapse in a dipolar BEC [7].

In conclusion, we have demonstrated the first BEC of Er atoms and the tunability of its interparticle interaction via Feshbach resonances. Our scattering data provide first sensitive input to understand the complex collisional behavior of submerged-shell atoms. The observation of the d-wave collapse is very encouraging in view of future experiments dedicated to the rich phenomena expected in strongly dipolar quantum gases.

We are grateful to F. Schreck, S. Stellmer, and B. Pasquiu (Innsbruck Sr team) for their continuous support. We thank the Yb teams in Kyoto and Tokyo for their advice, M. Springer for technical support, and E. Zupanič for contributions in an earlier stage of the experiments. This work is supported by the Austrian Ministry of Science and Research (BMWF) and the Austrian Science Fund (FWF) through a START grant under Project No. Y479-N20 and by the European Research Council under Project No. 259435.

[1] T. Lahaye, C. Menotti, L. Santos, M. Lewenstein, and T. Pfau, Rep. Prog. Phys. **72**, 126401 (2009).
[2] M. A. Baranov, Phys. Rep. **464**, 71 (2008).
[3] K. Goral, K. Rzazewski, and T. Pfau, Phys. Rev. A **61**, 051601 (2000).
[4] B. Damski, L. Santos, E. Tiemann, M. Lewenstein, S. Kotochigova, P. Julienne, and P. Zoller, Phys. Rev. Lett. **90**, 110401 (2003).
[5] G. Pupillo, A. Micheli, H. P. Büchler, and P. Zoller, in *Cold Molecules: Theory, Experiment, Applications*, edited by R. V. Krems, W. C. Stwalley, and B. Friedrich (CRC Press, Boca Raton, 2009), Chap. 12.
[6] D. S. Jin and J. Ye, Phys. Today **64**, 27 (2011).
[7] T. Lahaye, J. Metz, B. Fröhlich, T. Koch, M. Meister, A. Griesmaier, T. Pfau, H. Saito, Y. Kawaguchi, and M. Ueda, Phys. Rev. Lett. **101**, 080401 (2008).
[8] T. Lahaye, T. Koch, B. Fröhlich, M. Fattori, J. Metz, A. Griesmaier, S. Giovanazzi, and T. Pfau, Nature (London) **448**, 672 (2007).
[9] B. Pasquiou, G. Bismut, E. Maréchal, P. Pedri, L. Vernac, O. Gorceix, and B. Laburthe-Tolra, Phys. Rev. Lett. **106**, 015301 (2011).
[10] J. J. McClelland and J. L. Hanssen, Phys. Rev. Lett. **96**, 143005 (2006).
[11] M. Lu, N. Q. Burdick, S. H. Youn, and B. L. Lev, Phys. Rev. Lett. **107**, 190401 (2011).
[12] M. Lu, N. Q. Burdick, and B. L. Lev, arXiv:1202.4444 [Phys. Rev. Lett. (to be published)].
[13] H. Y. Ban, M. Jacka, J. L. Hanssen, J. Readerand, and J. J. McClelland, Opt. Express **13**, 3185 (2005).
[14] The Er electronic configuration is [Xe] $4f^{12}6s^2$. The electronic ground state is a $^3H_6$ state, meaning $L = 5$ (H state), $S = 1$, and $J = 6$. L, S, J denote the quantum numbers for the orbital angular momentum, for the spin, and for the total electronic angular momentum, respectively. ^{168}Er has zero nuclear spin ($I = 0$) and consequently does not exhibit a hyperfine structure.
[15] R. V. Krems, G. C. Groenenboom, and A. Dalgarno, J. Phys. Chem. A **108**, 8941 (2004).
[16] C. B. Connolly, Y. S. Au, S. C. Doret, W. Ketterle, and J. M. Doyle, Phys. Rev. A **81**, 010702 (2010).
[17] C. Chin, R. Grimm, P S. Julienne, and E. Tiesinga, Rev. Mod. Phys. **82**, 1225 (2010).
[18] S. Kotochigova and A. Petrov, Phys. Chem. Chem. Phys. **13**, 19165 (2011).
[19] A. Petrov, E. Tiesinga, and S. Kotochigova, arXiv:1203.4172.
[20] Y. Takasu, K. Maki, K. Komori, T. Takano, K. Honda, M. Kumakura, T. Yabuzaki, and Y. Takahashi, Phys. Rev. Lett. **91**, 040404 (2003).
[21] T. Fukuhara, S. Sugawa, and Y. Takahashi, Phys. Rev. A **76**, 051604(R) (2007).
[22] A. Frisch, K. Aikawa, M. Mark, A. Rietzler, J. Schindler, E. Zupanic, R. Grimm, and F. Ferlaino, arXiv:1203.1460 [Phys. Rev. A (to be published)].
[23] The MOT stage includes a 15 s loading phase, in which the light is red detuned by -9.5 MHz, and a compression phase, in which we reduce the detuning to -0.8 MHz and the MOT beam intensity by about a factor of 400. The compression phase is used to obtain colder and denser samples and it is optimized for loading efficiency into the dipole trap.
[24] H. Katori, T. Ido, Y. Isoya, and M. Kuwata-Gonokami, Phys. Rev. Lett. **82**, 1116 (1999).
[25] Initially only the power of the horizontal beam is reduced to its final value of 230 mW, while the vertical beam power is reduced during the last 600 ms of evaporation to its final

value of 1.5 W.
[26] We use the strong blue transition at 401 nm for imaging.
[27] S. Jochim, M. Bartenstein, G. Hendl, J. H. Denschlag, R. Grimm, A. Mosk, and W. Weidemüller, Phys. Rev. Lett. **89**, 273202 (2002).
[28] M. Zaccanti, C. D'Errico, F. Ferlaino, G. Roati, M. Inguscio, and G. Modugno, Phys. Rev. A **74**, 041605 (2006).
[29] The magnetic field is calibrated via rf-spectroscopy between Zeeman sublevels. From the calibration we estimate a short-term stability of 1 mG and a long-term stability of about 10 mG.
[30] V. Roudnev and M. Cavagnero, Phys. Rev. A **79**, 014701 (2009).
[31] J. L. Bohn, M. Cavagnero, and C. Ticknor, New J. Phys. **11**, 055039 (2009).
[32] K. K. Ni, S. Ospelkaus, D. Wang, G. Quemener, B. Neyenhuis, M. H. G. de Miranda, J. L. Bohn, J. Ye, and D. S. Jin, Nature (London) **464**, 1324 (2010).

Bibliography

[Aik12] K. Aikawa, A. Frisch, M. Mark, S. Baier, A. Rietzler, R. Grimm, and F. Ferlaino, *Bose-Einstein Condensation of Erbium*, Phys. Rev. Lett. **108**, 210401 (2012).

[And95] M. H. Anderson, J. R. Ensher, M. R. Matthews, C. E. Wieman, and E. A. Cornell, *Observation of Bose-Einstein condensation in dilute atomic vapor*, Science **269**, 198 (1995).

[Ang68] J. R. P. Angel and P. G. H. Sandars, *The Hyperfine Structure Stark Effect. I. Theory*, Proc. R. Soc. Lond. A **305**, 125 (1968).

[Ban05] H. Ban, M. Jacka, J. Hanssen, J. Reader, and J. McClelland, *Laser cooling transitions in atomic erbium*, Opt. Express **13**, 3185 (2005).

[Bar08] M. A. Baranov, *Theoretical progress in many-body physics with ultracold dipolar gases*, Physics Reports **464**, 71 (2008).

[Bea08] Q. Beaufils, R. Chicireanu, T. Zanon, B. Laburthe-Tolra, E. Maréchal, L. Vernac, J.-C. Keller, and O. Gorceix, *All-optical production of chromium Bose-Einstein condensates*, Phys. Rev. A **77**, 061601 (2008).

[Bla12] P. B. Blakie, D. Baillie, and R. N. Bisset, *Roton spectroscopy in a harmonically trapped dipolar Bose-Einstein condensate*, Phys. Rev. A **86**, 021604 (2012).

[Bra95] C. C. Bradley, C. A. Sackett, J. J. Tollett, and R. G. Hulet, *Evidence of Bose-Einstein condensation in an atomic gas with attractive interactions*, Phys. Rev. Lett. **75**, 1687 (1995).

[Chi06] J. K. Chin, D. E. Miller, Y. Liu, C. Stan, W. Setiawan, C. Sanner, K. Xu, and W. Ketterle, *Evidence for superfluidity of ultracold fermions in an optical lattice*, Nature **443**, 961 (2006).

[Chi10] C. Chin, R. Grimm, P. S. Julienne, and E. Tiesinga, *Feshbach resonances in ultracold gases*, Rev. Mod. Phys. **82**, 1225 (2010).

[Con10] C. B. Connolly, Y. S. Au, S. C. Doret, W. Ketterle, and J. M. Doyle, *Large spin relaxation rates in trapped submerged-shell atoms*, Phys. Rev. A **81**, 010702 (2010).

[Cow81] R. D. Cowan, *The Theory of Atomic Structure and Spectra*, Berkeley, CA: University of California Press (1981).

[Cro09] A. D. Cronin, J. Schmiedmayer, and D. E. Pritchard, *Optics and interferometry with atoms and molecules*, Rev. Mod. Phys. **81**, 1051 (2009).

[Dav95] K. B. Davis, M. O. Mewes, M. R. Andrews, N. J. van Druten, D. S. Durfee, D. M. Kurn, and W. Ketterle, *Bose-Einstein condensation in a gas of sodium atoms*, Phys. Rev. Lett. **75**, 3969 (1995).

[DeM99] B. DeMarco and D. S. Jin, *Onset of Fermi Degeneracy in a Trapped Atomic Gas*, Science **285**, 1703 (1999).

[Dem05] W. Demtröder, *Experimentalphysik 3, Atome, Moleküle und Festkörper*, Springer Verlag (2005).

[Dra96] G. Drake, *Atomic, Molecular and Optical Physics Handbook*, American Institute of Physics (1996).

[Dzu11] V. A. Dzuba, V. V. Flambaum, and B. L. Lev, *Dynamic polarizabilities and magic wavelengths for dysprosium*, Phys. Rev. A **83**, 032502 (2011).

[Fer09] F. Ferlaino, S. Knoop, and R. Grimm, *Cold Molecules: Theory, Experiment, Applications*, chapter Ultracold Feshbach molecules, Taylor & Francis (2009).

[Fer10] F. Ferlaino and R. Grimm, *Forty years of Efimov physics: How a bizarre prediction turned into a hot topic*, Physics **3**, 9 (2010).

[Fey82] R. P. Feynman, *Simulating Physics with Computers*, Int. J. Th. Phys. **21**, 467 (1982).

[Fri12] A. Frisch, K. Aikawa, M. Mark, A. Rietzler, J. Schindler, E. Zupanič, R. Grimm, and F. Ferlaino, *Narrow-line magneto-optical trap for erbium*, Phys. Rev. A **85**, 051401 (2012).

[Gor00] K. Goral, K. Rzazewski, and T. Pfau, *Bose-Einstein condensation with magnetic dipole-dipole forces*, Phys. Rev. A **61**, 051601 (2000).

[Gra07] C. Grain, T. Nazarova, C. Degenhardt, F. Vogt, C. Lisdat, E. Tiemann, U. Sterr, and F. Riehle, *Feasibility of narrow-line cooling in optical dipole traps*, Eur. Phys. J. D **42**, 317 (2007).

[Gre02] M. Greiner, O. Mandel, T. Esslinger, T. W. Hänsch, and I. Bloch, *Quantum phase transition from a superfluid to a Mott insulator in a gas of ultracold atoms*, Nature **415**, 39 (2002).

[Gre08] M. Greiner and S. Föllig, *Condensed-matter physics: Optical lattices*, Nature **453**, 736 (2008).

[Gri00] R. Grimm, M. Weidemüller, and Y. B. Ovchinnikov, *Optical dipole traps for neutral atoms*, Adv. At. Mol. Opt. Phys. **42**, 95 (2000).

[Gri05] A. Griesmaier, J. Werner, S. Hensler, J. Stuhler, and T. Pfau, *Bose-Einstein condensation of chromium*, Phys. Rev. Lett. **94**, 160401 (2005).

[Han04] C. I. Hancox, S. C. Doret, M. T. Hummon, L. Luo, and J. M. Doyle, *Magnetic trapping of rare-earth atoms at millikelvin temperatures*, Nature **431**, 281 (2004).

[Jam92] A. M. James and M. P. Lord, *Macmillan's chemical and physical data*, Macmillan (1992).

[Joc03] S. Jochim, M. Bartenstein, A. Altmeyer, G. Hendl, S. Riedl, C. Chin, J. Hecker Denschlag, and R. Grimm, *Bose-Einstein Condensation of Molecules*, Science **302**, 2101 (2003).

[Koc08] T. Koch, T. Lahaye, J. Metz, B. Fröhlich, A. Griesmaier, and T. Pfau, *Stabilization of a purely dipolar quantum gas against collapse*, Nature Phys. **4**, 218 (2008).

[Koh07] C. Kohstall, *A New Toolbox for Experiments with Ultracold ^6Li*, Diploma thesis, Universität Innsbruck (2007).

[Kot11] S. Kotochigova and A. Petrov, *Anisotropy in the interaction of ultracold dysprosium*, Phys. Chem. Chem. Phys. **13**, 19165 (2011).

[Kre04] R. V. Krems, G. C. Groenenboom, and A. Dalgarno, *Electronic Interaction Anisotropy between Atoms in Arbitrary Angular Momentum States*, J. Phys. Chem. A **108**, 8941 (2004).

[Lah08] T. Lahaye, J. Metz, B. Fröhlich, T. Koch, M. Meister, A. Griesmaier, T. Pfau, H. Saito, Y. Kawaguchi, and M. Ueda, *d-wave collapse and explosion of a dipolar Bose-Einstein condensate*, Phys. Rev. Lett. **101**, 080401 (2008).

[Lah09] T. Lahaye, C. Menotti, L. Santos, M. Lewenstein, and T. Pfau, *The physics of dipolar bosonic quantum gases*, Rep. Prog. Phys. **72**, 126401 (2009).

[Law10] J. E. Lawler, J.-F. Wyart, and E. A. D. Hartog, *Atomic transition probabilities of Er I*, J. Phys. B: At. Mol. Opt. Phys. **43**, 235001 (2010).

[Lim11] A. R. P. Lima and A. Pelster, *Quantum fluctuations in dipolar Bose gases*, Phys. Rev. A **84**, 041604 (2011).

[Lu11] M. Lu, N. Q. Burdick, S. H. Youn, and B. L. Lev, *Strongly Dipolar Bose-Einstein Condensate of Dysprosium*, Phys. Rev. Lett. **107**, 190401 (2011).

[Lu12] M. Lu, N. Q. Burdick, and B. L. Lev, *Quantum Degenerate Dipolar Fermi Gas*, Phys. Rev. Lett. **108**, 215301 (2012).

[McC06a] J. J. McClelland, *Natural linewidth of the 401-nm laser-cooling transition in Er I*, Phys. Rev. A **73**, 064502 (2006).

[McC06b] J. J. McClelland and J. L. Hanssen, *Laser cooling without repumping: A magneto-optical trap for erbium atoms*, Phys. Rev. Lett. **96**, 143005 (2006).

[Ney12] B. Neyenhuis, B. Yan, S. A. Moses, J. P. Covey, A. Chotia, A. Petrov, S. Kotochigova, J. Ye, and D. S. Jin, *Anisotropic Polarizability of Ultracold Polar $^{40}K^{87}Rb$ Molecules*, arXiv:1209.2226 (2012).

[Osp10] S. Ospelkaus, K.-K. Ni, D. Wang, M. H. G. de Miranda, B. Neyenhuis, G. Quéméner, P. S. Julienne, J. L. Bohn, D. S. Jin, and J. Ye, *Quantum-State Controlled Chemical Reactions of Ultracold Potassium-Rubidium Molecules*, Science **327**, no. 5967, 853 (2010).

[Pet12] A. Petrov, E. Tiesinga, and S. Kotochigova, *Anisotropy-Induced Feshbach Resonances in a Quantum Dipolar Gas of Highly Magnetic Atoms*, Phys. Rev. Lett. **109**, 103002 (2012).

[Phi92] W. Phillips, *Laser cooling and trapping of neutral atoms*, International School of Physics "Enrico Fermi" (1992).

[Ral11] Y. Ralchenko, A. Kramida, J. Reader, and N. A. Team, *NIST Atomic Spectra Database (ver. 4.1.0)* (2011).

[Sal91] B. E. A. Saleh and M. C. Teich, *Fundamentals of photonics*, John Wiley & Sons, Inc. (1991).

[San03] L. Santos, G. V. Shlyapnikov, and M. Lewenstein, *Roton-Maxon Spectrum and Stability of Trapped Dipolar Bose-Einstein Condensates*, Phys. Rev. Lett. **90**, 250403 (2003).

[Sch01a] F. Schreck, G. Ferrari, K. L. Corwin, J. Cubizolles, L. Khaykovich, M.-O. Mewes, and C. Salomon, *Sympathetic cooling of bosonic and fermionic lithium gases towards quantum degeneracy*, Phys. Rev. A **64**, 011402 (2001).

[Sch01b] F. Schreck, L. Khaykovich, K. L. Corwin, G. Ferrari, T. Bourdel, J. Cubizolles, and C. Salomon, *Quasipure Bose-Einstein Condensate Immersed in a Fermi Sea*, Phys. Rev. Lett. **87**, 080403 (2001).

[Sch06] P. Schwerdtfeger, *Atomic Static Dipole Polarizabilities*, ed. G. Maroulis, IOS Press, Amsterdam (2006).

[Sch07] H. Schöbel, *Ultrakalte Cs_2-Moleküle in einer optischen Dipolfalle mit kontrollierbarer Elliptizität*, Diploma thesis, Universität Innsbruck (2007).

[Sch11] J. Schindler, *Characterization of an Erbium Atomic Beam*, Master's thesis, Universität Innsbruck (2011).

[Söd98] J. Söding, D. Guéry-Odelin, P. Desbiolles, G. Ferrari, and J. Dalibard, *Giant spin relaxation of an ultracold cesium gas*, Phys. Rev. Lett. **80**, 1869 (1998).

[Tan10] L.-Y. Tang, Z.-C. Yan, T.-Y. Shi, and J. Mitroy, *Dynamic dipole polarizabilities of the Li atom and the Be^+ ion*, Phys. Rev. A **81**, 042521 (2010).

[Tru01] A. G. Truscott, K. E. Strecker, W. I. McAlexander, G. B. Partridge, and R. G. Hulet, *Observation of Fermi Pressure in a Gas of Trapped Atoms*, Science **291**, 2570 (2001).

[Win06] K. Winkler, G. Thalhammer, F. Lang, R. Grimm, J. Hecker Denschlag, A. J. Daley, A. Kantian, H. P. Büchler, and P. Zoller, *Repulsively bound atom pairs in an optical lattice*, Nature **441**, 853 (2006).

[Wya12] J.-F. Wyart, M. Lepers, and O. Dulieu, Private communication (2012).

Danksagung

First of all I want to thank Francesca for letting me be part of the erbium team. She supported me in every possible way – in preparing my talks, in the decision concerning my scientific future and finally in the writing phase of my thesis. I want to thank her for giving me the possibility to work independently on such a crucial part of our experiment. I had the luck to join the erbium team in a very exciting phase and really look forward to my time as a Ph.D student.

Des Weiteren möchte ich mich bei Rudi Grimm bedanken – für die Aufnahme in eine so professionell arbeitende wissenschaftliche Gruppe mit einem äußerst angenehmen Arbeitsklima. Besonders viel Freude hat mir die Abstimmung unserer Vorträge auf der YAO Konferenz gemacht, die es mir ermöglichte unsere sensationellen experimentellen Ergebnisse als Erster präsentieren zu dürfen – *"The correct answer is ... 13"*.

Vielen herzlichen Dank allen Gruppenmitgliedern, die mich schnell als einen der Ihren aufgenommen haben. Christoph für seine nützlichen Tipps zum Scanning System, Simon für sein Know-how im Bereich von High-Power Linsen und all jenen die mich bereitwillig in ihren Utensilien stöbern haben lassen.

Mein besonderer Dank gilt dem Erbium Team, für die unglaublich angenehme Atmosphäre auch bei Problemen im Labor, sowie bei unseren "Breakfast & Besprechung" Meetings, die gerne auch mal über Mittags hinaus gedauert haben. Von Alberts technischen Wissen, seiner Fähigkeit sich von Problemen nicht aus der Bahn werfen zu lassen und seiner Liebe für Details konnte ich mir hoffentlich vieles abschauen. I enjoyed the talks with Kiyotaka concerning science, attitude and lifestyle and want to thank him for always encouraging me to push the limits. Ein großer Anteil dieser Masterarbeit ist Michael zu verdanken. Er hat alle wichtigen Entscheidungen bezüglich dieser Arbeit mit mir gemeinsam getroffen und mich in meinem Kampf mit Elektronik, Laserprofilen und *MATHEMATICA*-Code stets unterstützt. Besonders hervorzuheben ist die intensive Zeit die wir zur Fertigstellung des Laseraufbaus gemeinsam investiert haben – Vielen Dank! Michael S. und Ben danke ich für die Diskussionen auf Augenhöhe im Labor.

Alle Institutsmitarbeiter waren nie um eine Hilfe verlegen. Im organisatorischen Bereich haben sich vor allem Christine und Nicole um alle meine Anfragen und Rechungen gekümmert. Michael und Wolfgang waren stets die richtigen Ansprechpersonen für Fragen rund um IT und nicht zu funktionierend scheinende Elektronik. Helmut hat mit seinem unverwechselbaren Stil meine anfänglich noch bescheidenen Kenntnisse im Bohren, Fräsen und Drehen maßgeblich verbessert. Armin und Toni möchte ich für die Fertigung der maßgeschneiderten Breadboards danken.

Furthermore I want to thank Maxcence Lepers from the Université of Lille and Jean-François from the Laboratoire Aimé Cotton in Orsay for providing me always with the newest set of data for my calculations.

Meine Studienkollegen Florian, Christian und Michael haben viel ihrerseits beigetragen, sodass mein Physikstudium vieles, aber sicher nicht langweilig war. Legendäre Physikerfeste, intensive Lerneinheiten im 8. Stock und aufgelockerte Vorlesungen und Proseminare sind nur einige Anekdoten aus dieser Zeit. Besonders Michael danke ich für die langjährige Zusammenarbeit und die zahlreichen Diskussionen.

Der wahrscheinlich größte Dank gilt meinen Eltern, die mir durch ihre Unterstützung in allen Lebenslagen eine vollkommen freie Entscheidung bezüglich meines Werdeganges ermöglichen. Meiner Mutter danke ich für all die Diskussionen über Gott und die Welt, meinem Vater für all die horizonterweiternden Touren in den Bergen dieser Welt und meinem Bruder Stefan danke ich für das so angenehme Zusammenleben. Bei meinen Großeltern möchte ich mich für ihr immerwährendes Interesse bedanken und für die traditionellen wöchentlichen Telefonate. Mein Onkel Gottfried hat schon früh den Wissenschaftler in mir erkannt und fördert mich auch weiter auf diesem Weg. Meine Freundin Katrin ist immer für mich da und gibt mir stets Kraft, sodass ich daran glaube alles schaffen zu können – dafür schätze ich sie besonders. Vielen Dank euch allen, dass ihr mich immer an die wirklich wichtigen Dinge im Leben erinnert.